PERSPECTIVES ON DEGRADATION IN SOLID OXIDE FUEL CELLS USING X-RAY SPECTROSCOPIES AND SCATTERING

A Thesis
Presented to
The Academic Faculty

by

Samson Yuxiu Lai

In Partial Fulfillment
of the Requirements for the Degree
Doctor of Philosophy in the
School of Materials Science and Engineering

Georgia Institute of Technology
December 2015

PERSPECTIVES ON DEGRADATION IN SOLID OXIDE FUEL CELLS USING X-RAY SPECTROSCOPIES AND SCATTERING

Approved by:

Professor Meilin Liu,
Committee Chair
School of Materials Science and Engineering
Georgia Institute of Technology

Professor Gleb Yushin
School of Materials Science and Engineering
Georgia Institute of Technology

Professor Faisal M. Alamgir, Advisor
School of Materials Science and Engineering
Georgia Institute of Technology

Professor Thomas M. Orlando
School of Chemistry and Biochemistry
Georgia Institute of Technology

Professor Preet Singh
School of Materials Science and Engineering
Georgia Institute of Technology

Date Approved: 30 October 2015

To my mother, my father,

and my brother.

ACKNOWLEDGEMENTS

First and foremost, I would like to thank my parents for all of their support. While my father knows what it is like to obtain a Ph.D., I am cognizant of the special kind of courage required particularly of parents to invest their time, emotion, and money into a field of engineering they do not fully understand but nevertheless trust that their child, whom they raised to the best of their ability, has the qualities to succeed. Heartfelt gratitude is owed to my brother, Yuxi, for always being there to talk to, supporting me through graduate school, and the best, if not always cooperative, Player 2 in any video game.

I probably cannot give enough thanks to my advisors, Drs. Faisal Alamgir and Meilin Liu. Their guidance, resilience, and patience have all been integral to my completion of the Ph.D. program. I will not be able to fathom the level of trust and faith required of them unless I one day become an Ph.D. advisor myself, but, failing that, I will acknowledge and appreciate what their efforts have meant for my success.

No one gets through graduate school alone. Thanks goes to Dr. Robert Rettew, Dr. Cole Petersburg, Dr. Erin Redmond, (future Dr.) Alex Bryant, and (future Dr.) Adam Vitale, mentors, colleagues, and friends of the Alamgir group, for their mentorship and companionship during sleepless nights at the synchrotron. From the Liu group, Drs. Mingfei Liu, Dong Ding, Wentao Qin, Mingyang Gong, and Tao Wei all provided significant technical assistance with fuel cell sample preparation and intellectual discourse on international politics, particularly of Sino-American relations. Of course, the camaraderie of Drs. Xiaxi Li, Kevin Blinn, Matt Lynch, Min-Kyu Song, and Lei Yang (in memoriam) will never be forgotten; I am eager to join your ranks as the next-generation of Ph.D.s. Likewise, (future Drs.) Ben Rainwater, Gordon

Waller, Brian Doyle, Dongchang Chen, Lei Zhang, Ryan Murphy, and Jun Hyuk Kim along with Sophia Feng and Cynthia Cromer are all deserving of thanks, among many others who joined the Liu group from abroad too innumerable to list, for making the Liu group truly a pleasure to work in and for making the graduate school experience socially worthwhile. I look forward to seeing and hearing about all of your successes to come.

Special thanks goes to the many friends of Saturday Cooking Night over the years: my partner-in-crime, the king-of-bad-ideas, and troublemaking tippler (Dr.) Adrian Lam; fellow enthusiast of Japanese culture, (Dr.) Ken Pradel; (Dr.) Jeff Wong, Wesley Wang, (Dr.) Elaine Tang, (Dr.) Ken Chiu, (Dr.) Samantha Lo, (Dr.) Brian Gestner, Linda Hui, Wenny Liu, (future Dr.) Yizheng Chen, Grace Lee, and (real Dr.) Irene Lai. Over time, the friends come and go and the food always changes, but there is always a seat for you at my dinner table. See you on Saturday night.

Use of the National Synchrotron Light Source (NSLS), Brookhaven National Laboratory, was supported by the U.S. Department of Energy (DOE), Contract No. DE-AC02-98CH10-886. I must acknowledge the technical expertise and aid provided by the many beamline scientists and postdoctoral scholars at the NSLS, in no particular order, Bruce Ravel, Cherno Jaye, Conan Weiland, Barry Karlin, Joe Woicik, Kumi Pandya, Nebosja Marinkovic, Peter Albrecht, Syed Khalid, Dan Fischer, Adele Wang, Sanjaya Senanayake, and Wenqian Xu. The contributions were both large and small, but all were essential to my work at the synchrotron.

Technical research work was supported by the HeteroFoaM Center, a U.S. DOE Energy Frontier Research Center, Award Number DE-SC0001061.

For my Student-Teacher Enhancement Partnership (STEP) fellowship, I must thank Drs. Donna C. Llewellyn and Marion C. Usselman for nurturing Ph.D. students into pedagogical changemakers and inspiring the noble act of teaching. The STEP

Fellowship was supported by the National Science Foundation under Grant No. DGE-0338261.

Fellowship support was also provided by the National Science Foundations Integrative Graduate Education Research and Traineeship (IGERT): Nanostructured Materials for Energy Conversion and Storage (NESAC) at Georgia Tech under Award Number 1069318. Sincere thanks goes to Dr. Elsa Reichmanis and the NESAC IGERT executive committee for selecting me and providing me the opportunity to expand my perspectives of science into the world of policy and the intertwined relationship between them. Acknowledgements also are given to (future Drs.) Jonah Bea-Taylor, Nabil Kleinhenz, Rebecca Hill, and Alexander Smith for being faithful and steadfast companions in the journey of being NESAC IGERT fellows.

I must also thank the Materials Research Society, The Electrochemical Society, the Student Chapter of the Electrochemical Society at Georgia Tech, the Local Chapter of The Electrochemical Society in Atlanta, GA, the Georgia Tech Institute of Materials, and the HeteroFoaM Center for prize support of poster competitions and for fostering communities of like-minded researchers that remind us of the context of our work, inspire us with new ideas, and help us find common ground amongst uncommon individuals.

There are countless other individuals who have contributed to the person I have become over my years in graduate school. Writing of this dissertation was aided by those who followed my #dissertuesday posts and voiced their support. I would be remiss to neglect a few more important individuals, without particular categorization: (future real Dr.) Joyce Loh, for friendship; (Dr.) Keenan Zhuo, for curious conversation; and lastly, but the opposite of least, (future Dr.) Chia-Chi Kathy Tuan, for her kindness. Thank you, all; thank you so much.

TABLE OF CONTENTS

LIST OF TABLES

LIST OF FIGURES

SUMMARY

Solid oxide fuel cells (SOFCs) represent a major piece of a next-generation, renewable, clean energy economy and contribute to combating anthropogenic climate change by efficiently converting chemical energy into electrical energy through electrochemical reactions. However, despite adding significant chemical, mechanical, and microstructural complexity to push SOFC performance ever higher, cost and durability remain significant barriers to SOFC commercialization. Two of these issues are cathode stability in atmospheres containing carbon dioxide and water vapor and anode stability in fuel containing hydrogen sulfide. With regards to those aspects, state-of-the-art SOFC cathodes like $La_{1-x}Sr_xMnO_{3-\delta}$ (LSM) and $La_{1-x}Sr_xCo_{1-y}Fe_yO_{3-\delta}$ (LSCF) and anodes (NiO and $BaZr_{0.1}Ce_{0.7}Y_{0.1}Yb_{0.1}O_{3-\delta}$ (BZCYYb)) are studied to understand the interactions between contaminants and electrodes.

In this work, powerful *in situ* and *operando* x-ray spectroscopy and scattering experiments provide deep insight into the physiochemical phenomena that define the behavior of SOFC electrode materials. For example, *in situ* x-ray absorption spectroscopy (XAS) has been successfully used to tracked the charge-compensation behavior (or change in oxidation states) of both Mn and Co metal cations in a state-of-the-art LSM-infiltrated LSCF composite cathode as oxygen vacancies were introduced or removed by controlling the chemical environment. Thermal annealing in oxidizing or reducing atmospheres, however, caused more Mn cations to adopt a more ordered local structure and higher crystal field splitting energies, resulting in a more stable, low spin electron configuration of the *d*-band orbitals. In contrast, Co cations show a fully reversible change in oxidation state before and after thermal annealing, thus implying that the LSM infiltration provides LSCF cathode performance enhancement

through structural and chemical stability of the Mn in the surface LSM coating.

To gain insight into the degradation mechanism of SOFC electrodes, *operando* x-ray absorption spectroscopy is used to probe the evolution in surface chemistry and structure of an LSCF thin film cathode exposed to contaminants commonly encountered under practical fuel cell operating conditions. Backed by the robustness of simultaneous reference foil measurements, slight oxidation shifts were observed in the Fe and Co cation absorption edges after exposure to CO_2 while H_2O has a neutral or slight reduction effect. Negative electrical polarization resulted in slight reduction shifts. Pump-probe, *in situ* synchrotron x-ray photoelectron spectroscopy (XPS) complementarily showed strong oxidation of Co and migration of it to the surface along with evolving oxygen signals from carbonates and hydroxides for CO_2 and H_2O exposure, respectively. The experiment also demonstrated that electrical polarization in the presence of gas contaminants made oxidation more severe, which was an unexpected interaction that was contrary to what would be predicted by complementary *in situ* experiments that tested only electrical polarization or only gas contaminant at temperature, thereby showcasing the importance of *operando* experiments.

Combining *in situ* x-ray absorption spectroscopy and *in situ* pair distribution function provides evidence that sulfur exchanges with oxygen and bonds to Ni and Yb cations, the latter from which the sulfur-tolerance property may originate. While tracking transient crystalline phases with *in situ* x-ray diffraction (XRD) indicated that nickel oxide experienced reduction, the more complicated case of BZCYYb showed $BaCO_3$ was also present, which then decomposed into BaO at high temperature. The resulting BaO then reacts with the water vapor to temporarily form $Ba(OH)_2 \bullet H_2O$ until exposure to H_2S. Further *in situ* pair distribution function data also suggested the same sulfur-oxygen exchange behavior as was observed in EXAFS.

These studies demonstrate that proper combination of *in situ* and *operando* experiments, due partially to the powerful intensity and capabilities of synchrotron x-rays, can provide unique information that has never before been possible and is critical to gaining new perspectives and to better understand data where a single perspective may only lead to ambiguous conclusions. Such a multi-pronged characterization approach is vital to gaining a better understanding of complex SOFC materials and providing critical insights for rational design of next-generation SOFC electrode materials.

CHAPTER I

INTRODUCTION

1.1 Motivation and Scope

A scientist's obligation is to his or her society. In return for the investment society makes in educating and supporting a scientist, society turns to the scientist to provide answers to unprecedented problems. In the same spirit, this thesis research is motivated by a strong sense of duty to the social debt of honor and by the potential to advance the the well-being of humans across the globe. It is the author's belief that anthropogenic climate change is the most severe threat to this and future generations. As a result, this thesis is aimed at contributing to the body of knowledge and joining the many scientists that aim to study, understand, and ultimately combat climate change.

A discussion of the evidence, trends, and consequences of anthropogenic climate change cannot be afforded by the limited space here, but mountains of relevant information are easily accessible. Simply put, one of the strategies to reducing climate change, particularly without significantly compromising the standard of living, is to develop higher efficiency energy conversion devices. One such type of energy conversion process that holds potential on the scale of affecting climate change is fuel cell technology, which converts chemical energy to electrical energy without the thermal combustion of the fuel. Lastly, of the many types of fuel cells that exist, this thesis is relevant only to solid oxide fuel cells.

1.2 Role of solid oxide fuel cells in a renewable energy economy

The policy stance on the forthcoming renewable energy economy is that it will consist of many renewable energy sources. This should not be surprising, as it is much like the current status quo of fossil fuels being a diverse portfolio of coal, oil, and natural gas to serve a diverse set of energy needs. Currently, the major energy needs include baseload power for constant power production, peak power for dynamic power demand, and fuel for heating and transportation. With solar, wind, geothermal, nuclear, and biofuels still shaping their roles in an infantile and evolving renewable energy economy, where do fuel cells, and in particular, solid oxide fuel cells, fit into the puzzle?

Fuel cells are widely known by two major design types: low temperature proton-based fuel cells and high temperature oxide-based fuel cells. The proton exchange membrane fuel cells (PEMFCs) work by the movement of H^+ protons, hence the name. Solid oxide fuel cells (SOFCs) rely on the transport of oxide ions, which by the nature of their larger size, require much higher operating temperatures to achieve reasonable conductivity. There are, of course, many types of fuel cells which do not operate on the same exact transport principles (indeed, some materials can exhibit significant conductivity of protons and oxide ions simultaneously while others conduct entirely different ions), but PEMFCs and SOFCs dominate the field because they are the most commercially mature technologies.

Delineating fuel cells by these two types serves to reference the dichotomy in their fundamental chemical mechanisms of operation, each with their respective practical applications and challenges thereof. For example, prototype fuel cell vehicles by Toyota, Ford, and General Motors use PEMFCs for their power conversion technology because their mechanical flexibility and low operating temperature afford advantages in durability and fast start up time, respectively. In that field, durability of the

Pt catalyst and humidity management of the electrolyte are some of the main challenges. Conversely, Bloom Energy's Bloom box uses SOFC technology in stationary, on-site power generation situations where the longer start up time is traded for higher efficiency and where commercialization is supported by the premiums on electrical reliability and security. In SOFCs, more cost-effective, non-Pt catalysts can be used (although chemical durability can still be an issue depending on the fuel) and humidity management of the electrolyte is a non-issue, but the high temperature requirements and poorer mechanical properties of ceramic materials are just two of the many challenges. Based on their fundamental mechanisms, each type of fuel cell technology aims to fulfill a different role and faces different challenges in doing so.

In an ideal renewable, carbon-neutral energy economy, how does one imagine fuel cells working with other clean energy technologies? One can start with solar and wind, which are energy conversion technologies whose fuel is practically free of cost and carbon. But these somewhat unpredictably intermittent power sources need to be complemented by some kind of on-demand power generation or large-scale energy storage technology to pick up any slack. Using current technology, a natural gas turbine in a peaker plant, which is designed to come online quickly and to efficiently accommodate dynamic peak loads on the grid, would compensate for cloudy and/or windless periods. It is foreseeable for fuel cells to eventually replace gas-powered peaker plants, leveraging their solid-state design to rapidly meet fluctuating demand. Fuel cells are also advantaged by being able to use both hydrocarbon and cleaner hydrogen fuels, thereby providing a seamless bridge from a carbon-intensive to a carbon-free fuel economy. Furthermore, the high operating temperature of SOFCs mean that the system generates high quality waste heat, which can be used for more electricity generation or combined heat and power, ultimately increasing overall system efficiency.

Fuel cells could also play a role in grid-scale energy storage. A grid-scale battery,

on the order of megawatt-hours (MWh), is one approach to level electrical load on the grid and help intermittent energy sources succeed. The unfortunate fundamental barrier to large, grid-scale batteries is that the power and energy densities of each battery are interdependent because the electrode itself is changing as a function of the amount of energy stored. Thus, a low power but high energy battery may be over-built or underutilized according to the power and energy requirements at the grid level and consequently, cost-inefficient. Since fuel cells are open systems, the energy density and power requirements can be independently designed, respectively, by controlling the volume of the fuel and the area of the electrodes/fuel cell stack. The advantage of a fuel cell over a grid-scale battery would be the cost savings from design flexibility and ease of storing a liquid or gas fuel. It is worth mentioning that redox flow batteries, which are battery systems with some design characteristics common to fuel cells, have potential applications in the large-scale energy storage, since their energy and power densities can also be designed independently of each other [84, 79]. Ideally, fuel cells would be capable of using the excess electricity during periods of excess solar or wind generation to revert the exhaust products back into fuel for later use to close the loop, particularly if a carbon-based fuel is used. There are many nuances in fuel cells and batteries that have been overlooked by this thought experiment, but the primary goal is to understand the role of fuel cells as a combined power-and-fuel generation plant of the future renewable energy economy.

1.3 Challenges of SOFCs

SOFCs still face of a number of interrelated challenges in operating temperature, affordability of materials, and robustness. To function as an effective oxide ion conductor, the electrolyte of a SOFC must be at a significantly high temperature, typically in the range of 600 °C to 1000 °C. At these temperatures, there are not many materials with high stability that can last for the thousands of hours expected of a SOFC.

While lower temperature oxide ion conductors exist, the trade-off is frequently lower performance.

Using exotic materials capable of withstanding high temperatures has consequences in the cost of SOFCs, which already have significant processing costs from the high temperature ($> 1000\,^{\circ}\mathrm{C}$) sintering necessary for engineered materials to have longevity at operating temperatures. Besides the costs for manufacturing parts, there is the SOFC balance of system cost, which involves the heating, insulation, mass flow, and electrical subsystems. Like the photovoltaics industry, these balance of system costs will decrease over time, but will remain a significant cost to the technology as a whole.

One of the main barriers to commercialization is chemical stability and robustness of materials operating at high temperature. Contaminants in the gas phase can cause performance degradation and premature failure. Degradation phenomena can occur at the cathode, such as from water and carbon dioxide from ambient air [2], and the anode, typically from carbon and/or sulfur in the fuel. Additionally, at lower temperatures, Cr-poisoning from using ferritic stainless steel interconnects can be another source of chemical instability [26]. Despite the pre-existing complexity in SOFCs, yet more complex materials and enhancements, such as tuning microstructure or morphology, are needed to develop more robust electrodes.

One of the major touted advantages of SOFCs is fuel flexibility, which speaks to the ability for SOFCs to utilize hydrogen, natural gas, gassified coal, propane, and other fuels. However, an industrial state-of-the-art SOFC system with a nickel oxide anode cannot be directly fueled by any hydrocarbon fuel without steam reforming or a similar internal reforming reaction. With steam reformation, hydrocarbon fuels can be converted to hydrogen, which is oxidized for electricity, and carbon dioxide, which is dispelled as exhaust. Without steam reformation, the nickel oxide anode is almost immediately covered in carbonaceous species, a process referred to as coking,

that starve the anode from fuel and once deposited, the carbon is difficult to remove in a reducing atmosphere.

Even if carbon coking were to be solved through catalytic internal reforming, of which recent research has made much progress, there is still the challenge of hydrogen sulfide in natural gas causing sulfur poisoning of the anode. Concentration levels as low as $10\,\frac{\mu mol}{mol}$ to $100\,\frac{\mu mol}{mol}$ can be devastating to an SOFC anode; even if the fuel stream is cleaned, the recovery time for the performance is significant and the performance loss is not fully reversible. True fuel flexibility and robustness are still major challenges.

Ultimately, SOFCs are a proven concept but whether they can compete on the levels of conventional fossil fuel power generation is yet to be seen. The Solid State Energy Conversion Alliance (SECA) program under the Department of Energy's Office of Fossil Energy has led the research and commercialization effort of SOFCs at the federal level, setting targets of \$175/kW for stacks, \$700/kW for modules, and a degradation rate of less than 0.2 % per 1000 h for 40 000 h [54, 77]. Although SOFCs run at higher efficiency with the same fuels (and can thus easily integrate into existing infrastructure), the high price is the deciding factor for SOFCs to succeed commercially, except in niche applications where special premiums are willing to be paid for benefits that conventional technology cannot provide. Reducing the operating temperature to use more cost-effective materials and increasing robustness are scientific research strategies that will help accelerate SOFCs reach a competitive market.

The main materials science topic of this thesis is the study of SOFC materials' behavior to performance-degrading gas contaminants, primarily through the use of x-ray characterization. X-ray characterization affords a wide range of elemental and spatial specificity while providing a plethora of fundamental chemical, electronic, and structural information, which become particularly insightful when studying materials at or close to fuel cell operating conditions. Through this information, a deeper

understanding of the mechanism of electrode poisoning by gas contaminants can be obtained. Ideally, that will lead to fundamental knowledge that can inform the rational design of novel electrocatalysts that can tolerate contaminants in the gas phase with high performance and at low cost.

Even if so, the other aforementioned challenges in SOFC technology remain and while many other researchers are seeking solutions, those challenges will likely remain for some time, as SOFC technology slowly works its way through social and economic acceptance. There is great risk and difficulty in taking on the challenges facing SOFC technology but there are also potentially great rewards. SOFC technology foreseeably plays a role in distributed electric grids, scalable power generation systems, diverse fuel flexibility, energy security and independence from unstable foreign fossil-fuel exporting regimes, and in creating a cleaner energy economy primed for a transition to a future of hydrogen.

1.4 Chapter organization

Chapter 2 covers the basic fundamental principles for the operation of SOFCs and a review of the state-of-the-art in terms of materials choice and challenges related to SOFCs. Chapter 3 describes the technical approach used to address a few specific challenges and explains the principles behind the x-ray characterization used extensively throughout the research.

Chapter 4 details the experimentation and development of *in situ* transmission x-ray absorption spectroscopy, which serves as a stepping stone to the development of *operando* x-ray absorption spectroscopy experiments. Chapter 5 follows with the results of *operando* x-ray absorption spectroscopy and its augmentation by combining with *in situ* x-ray photoelectron spectroscopy. Both chapters 4 and 5 focus on state-of-the-art SOFC cathode materials.

Chapter 6 applies x-ray absorption spectroscopy experiments to the study of sulfur

poisoning of state-of-the-art SOFC anode materials. Following that discussion, the concept and use of *in situ* x-ray diffraction and pair distribution function measurements are detailed to augment the information from x-ray absorption spectroscopy. Each chapter is followed by a brief conclusion and a description of its significance in the broader context of the whole thesis. Chapter 7 concludes a summary and recommendations for future technical work.

CHAPTER II

BACKGROUND AND LITERATURE REVIEW

The operating principles of a SOFC will be briefly explained here, followed by some generalized statements about the SOFC field, synchrotron x-ray characterization, and references to specific literature.

2.1 Solid oxide fuel cell operation and key principles

At a macroscale systems level, a solid oxide fuel cell converts hydrogen fuel and ambient oxygen to form water electrochemically. The distinguishing aspect of this process occurring electrochemically is that it avoids oxidation of the hydrogen fuel via combustion, which generates significant amounts of heat which is then lost to the surrounding environment. A fuel cell thus achieves much higher efficiency through an electrochemical reaction at both the anode and the cathode. At the anode, molecular hydrogen gas is dissociated by Ni, which serves both as a catalyst and an electron conductor. At the cathode, molecular oxygen gas from the air is dissociated and reduced by a perovskite oxide that operates as both a catalyst and a mixed ion/electron conductor to move the dissociated oxygen anions through the electrolyte to the anode. Each electrochemical half reaction is shown below using Kröger-Vink notation:

$$H_2 \rightleftharpoons 2H^{\bullet} + 2e^{'} \tag{1}$$

$$O_X^O \rightleftharpoons V_O^{\bullet\bullet} + 2e^{'} + \frac{1}{2}O_2 \tag{2}$$

The electrolyte is a solid, oxide-conducting but electrically-insulating material that mechanically connects the anode and the cathode but in a way that prevents electrons from directly shorting the circuit and prevents fuel and air from mixing or reacting with the incompatible electrode. By forcing electrons and oxygen anions to take

separate routes from and to the anode, useful electrical work can be extracted from the fuel cell while the electrochemical reaction is completed, theoretically enabling continuous operation.

The performance of an SOFC depends on the number or size of interfacial junctions known as "triple-phase boundaries" (TPBs), where the electron-conducting phase, the ion-conducting phase, and the fuel or air gas phase are all simultaneously readily available to react. At locations besides the triple phase boundaries, the reaction is severely limited by the transport of one or two of the other reactants since each phase is typically not capable of fast conduction of more than one reactant (e.g., the electron-conducting phase has poor ionic conductivity and slow gas diffusion). As a result, SOFC electrodes are often made as composites of an electronically conductive catalyst and the ionically conductive electrolyte to increase the TPB length. The TPB is the most dynamic and important region for studying the fundamental surface reactions occurring but is also a complex region that is difficult to pinpoint and investigate under *in situ* conditions. Their importance has been studied and is illustrated by studies that show how the bulk regions of an electrode may be covered by contaminants but the SOFC can continue operation so long as the TPB regions remain clear [82, 56, 45, 19]. Some studies have shown or calculated the concentration of activity in the TPB region [56, 43].

2.1.1 Cathode materials and challenges

For optimal performance, solid oxide fuel cell cathodes require a combination of different properties related to temperature, oxidizing environment, conductivity, materials compatibility, and catalysis for the oxygen reduction reaction. For example, besides not decomposing rapidly at the high operating temperatures of SOFCs (as high as 1000 °C), the thermal expansion coefficient of a cathode needs to closely match the thermal expansion coefficient of the electrolyte or the cathode risks delamination with

heating and cooling cycles. Often, cathodes are frequently doped to increase ionic and/or electronic conductivity or catalytic activity but can suffer deficiencies in long term stability. There may also be issues with compatibility with systems materials, such as current collectors or sealants. Thus, development of cathode materials is frequently an exercise in compromise and incremental advancement.

For SOFC cathodes, the main barrier to higher performance is the oxygen reduction reaction, since polarization resistance at the cathode is typically a larger contributor to the overall cell resistance, relative to the electrolyte or anode depending on the full cell architecture. In recent years, significant efforts have been devoted to search for suitable cathode materials that are more active for O_2 reduction [81, 67]. To date, $La_{1-x}Sr_xMnO_{3\pm\delta}$ (LSM) ($> 800\,^{\circ}C$) and $La_{0.6}Sr_{0.4}Co_{0.2}Fe_{0.8}O_{3\pm\delta}$ (LSCF) ($< 750\,^{\circ}C$) based cathodes still remain the most widely used in SOFCs. The LSCF material shows much higher ionic and electronic conductivity, potentially extending the active sites beyond the triple phase boundary (TPB) to the surface of the LSCF far from the electrolyte [52], but it is limited by the long-term stability [70, 31], particularly in atmospheres containing carbon dioxide and water [2], and by slow surface exchange process for oxygen reduction reaction [34, 35, 45]. While LSM shows good stability and compatibility with yttria-stabilized zirconia (YSZ) electrolyte and excellent oxygen adsorption characteristics with rapid surface catalytic kinetics [12], it is limited by its poor ionic conductivity.

To better utilize the best properties of LSCF and LSM, a more efficient electrode architecture using a thin-film LSM coating to modify LSCF surface was proposed [40], and improved performance and stability has been demonstrated in our recent work [45]. Although different approaches, such as electrochemical performance test [45, 1], modeling and simulation [45], and microstructure analysis [45, 11], have been applied to study the degradation mechanism(s) of the LSCF cathode and the

performance enhancements of LSM-coated LSCF cathode (LSM-LSCF), there still remains difficulty in understanding the mechanism of this composite cathode structure. It is still not clear how the LSM coating improves the stability of LSCF cathode nor what local atomistic and electronic structures exist under operating conditions. In some cases, due to the structural similarity of LSCF and LSM, the results from local composition, morphology, and structure analysis are often confounded or ambiguous.

2.1.2 Anode materials and challenges

Other reactions can occur at a TPB that are undesirable for the operation of the SOFC. At the anode, contaminants in the fuel stream may deposit on surface, inhibiting the fuel cell's operation by blocking fuel from reaching the active sites of the anode. The resulting carbon deposition, or "coking", and sulfur poisoning are the primary causes of performance degradation in SOFCs, in particular, those that use hydrocarbon fuels instead of hydrogen. Carbon deposition typically originates from the reduction of carbon monoxide and dioxide and oxidation of a hydrocarbon fuel. Hydrogen sulfide is a naturally-occurring contaminant in "sour gas", a common source of natural gas, and may be oxidized into sulfur or sulfur-containing compounds at the surface of the anode. The effect of these contaminants on fuel cell performance is dramatic; within seconds or minutes, the fuel cell may be completely poisoned and producing fractions of its peak power density.

There has also been a focus of research efforts on developing high performance SOFCs that are highly robust against the poisoning mechanisms from sulfur in hydrogen sulfide [82, 83, 88, 51, 9, 38, 56, 87, 64, 78]. Current commercial state-of-the-art SOFC systems handle sulfur by using purification methods. However, these additional processes add significant costs that prevent SOFCs from achieving significant market presence and SOFCs still remain highly sensitive to even small concentrations of sulfur. The ideal SOFC anode would be a modified version of the well-studied

Ni and be robust enough to directly mediate sulfur poisoning caused by small to significant concentrations of hydrogen sulfide in the fuel stream.

One particular family of anode modifications based on barium cerates, zirconates, and oxides has proliferated advances in sulfur tolerance. For example, BaO nanoparticles have enabled carbon tolerance in Ni anodes [82]. In another case, a novel high temperature proton and oxide ion conductor, $BaZr_{0.1}Ce_{0.7}Y_{0.1}Yb_{0.1}O_{3-\delta}$ (BZCYYb), has demonstrated significant sulfur tolerance [83]. Later work was able to translate the sulfur tolerance to a Ni-YSZ anode through a surface nanoparticle modification [65, 3], analogous to BaO on Ni for coking tolerance [82]. However, little is known about how BZCYYb is able to ward off or catalyze sulfur.

The goal in this project is to gain an understanding of the sulfur tolerance mechanism of BZCYYb and synthesize more efficient catalyst materials that can be directly integrated with Ni-YSZ anodes. The motivation for adhering to the Ni-YSZ material system is that the Ni-YSZ system has been shown to have the best characteristics of chemical compatibility, well matched thermal expansion coefficients, microstructural stability, and economic competitiveness. Thus, the end result would be a BZCYYb-inspired nanoparticle surface modification for sulfur tolerance, without changing the existing Ni-YSZ anode material system. Using a nanoparticle-based surface modification strategy catalyzes the Ni surface without blocking the TPB sites essential to SOFC operation, and furthermore, allows that fundamental discovery to be rapidly implemented over an existing architecture, shortening the time and cost to bring the technology to market. However, the chance of success relies on procuring a deep and fundamental understanding of the sulfur poisoning mechanism in operating conditions.

Recent developments in solution infiltration hold significant promise in being able to deliver drastically enhanced fuel cell performance at low cost. Using simple wet chemistry methods, a variety of surface modifications and catalysts can be applied

to porous electrodes, yielding numerous advantages. First, well-studied and well understood materials, such as LSM and LSCF for cathode or Ni for the anode, can be used as the backbone material, providing a necessary network of mixed or electronic conductivity as well as mechanical strength. Secondly, since the solution infiltration method is adaptable to existing materials and architectures, the capital and research labor investments risks are much lower. For example, by relying on existing state-of-the-art electrodes as the backbone, major research effort does not need to be dedicated to optimizing chemical and thermomechanical compatibility with the electrolyte and the interconnect. Further, backbone/infiltration combinations can be synthesized in high volumes and evaluated rapidly. Thirdly, by only modifying the surface of the electrode or using nanoparticles of a catalyst, the most active portion of a material, the surface, is used efficiently while avoiding significant bulk which is largely a dead weight. Fourthly, catalysts tend to be novel and/or exotic materials, so minimizing their use with solution infiltration is cost efficient. The body of solution infiltration research for solid oxide fuel cells is better detailed in reviews [17, 25].

2.2 Advanced X-ray techniques using synchrotron light

2.2.1 Background on synchrotrons

Lab-scale x-rays are widely used in research laboratories as a versatile and fast characterization tools. However, more powerful and intense x-rays can be used for more insightful and information-rich characterization and in that regard, a type of particle accelerator known as a "synchrotron" light source is an extremely potent facility. To create powerful x-rays, a synchrotron uses electrons traveling at relativistic speeds with a curved trajectory. Electrons are first linearly accelerated into a booster ring, followed by further acceleration into to a larger, storage ring. The storage ring consists of a series of straight and curved segments where electromagnets oscillate and curve the trajectory of the electron beam. Due to the change in acceleration and the

conservation of energy, a wide spectrum of x-rays are emitted and focused through ports, slits, and mirrors into a beamline, which can service one or more experimental endstations. A radio frequency cavity is used to restore some of the energy lost by the electron beam, but periodically, the electron beam must be restored by a new injection from the linear accelerator and booster ring, since some electrons are eventually lost due to collisions with either gas particles, despite the extremely high vacuum, or the storage ring wall. The "synchronization" aspect of a synchrotron comes from the synchronization of the bunches of electrons that make up the beam as they are injected into the storage ring.

With a broad spectrum white light source, synchrotrons provide significant control over light-matter interactions compared to lab-scale fixed energy x-ray sources. A specific energy of x-ray can be selected from the white light by using a single crystal double monochromator. Additionally, the x-rays are emitted with intensities thousands to tens of thousands greater than what is possible from lab-scale x-ray sources. Based on the energy, sample composition, and detector-analyzer equipment, different advanced x-ray techniques can be used for characterization. Some characterization experiments, such as with x-ray absorption spectroscopy, are only practically possible with a synchrotron light source while others, such as x-ray diffraction or photoelectron spectroscopy, are enhanced by the use of synchrotron light. The theoretical basis, experimental details, and applications of these characterization tools will be further described in the Chapter 3.

2.2.2 Characterization under *in situ* or *operando* conditions

One of the major difficulties in characterizing SOFC materials is the capture of information under operating conditions. The term "*operando*" is used to describe such experiments and the information gained can be used to better understand chemical interactions and mechanisms on the surface, at interfaces, and in the bulk. In the case

of SOFC systems, we consider the term "*operando*" to refer to characterization experiments that include temperature, gas, and electrical current collection. Some prior *operando* experiments have been successful for low temperature polymer electrolyte fuel cells [59, 63, 36].

The high operating temperature of SOFCs presents a challenge in designing safe and effective experiments. Increased complexity also comes along in the form of controlling experimental parameters while simultaneously accommodating the needs of the probing technique. Optical and infrared characterization methods have found success in *operando* experiments [32, 5, 16] but synchrotron x-rays are highly desired for their wealth of element-specific information at different length scales, such as chemical shifts and local atomistic structure information at the surface and in the bulk.

For SOFC materials, while many efforts have been focused on *in situ* x-ray experiments, few studies examine the material state under the combined stimulus of temperature, atmosphere, and electrical polarization. In some *operando* experiments on thin films of lanthanum-based perovskite cathodes, the material's surface response to thermal annealing and electrical bias was examined through x-ray techniques but chemical interactions with contaminants in the gas were not explored [86, 7, 8]. Furthermore, the results of *in situ* experiments cannot necessarily be combined to predict the result of an *operando* experiment, similar to how *ex situ* results may fail to fully capture an *in situ* phenomenon. *Operando* spectroscopy is essential for providing insight into the reaction mechanisms and information for the rational design of novel materials [41].

There are three key challenges in developing *in situ* and *operando* experiments for SOFCs. Any experimental approach aimed at discovering the phenomenological steps in detail must be sufficiently sensitive, have relevant spatial resolution, and be capable to studying materials under true operating conditions. The first challenge of

any characterization technique is whether that method has the sensitivity to observe the chemical reaction of interest as it occurs. In order to understand the fundamental reaction mechanisms, sensitivity has two required aspects. The technique must be able to specifically collect information about a specific element or species, particularly as a function of time to track its transitions from one phase or moiety to another.

The second challenge of the investigation is having sufficient spatial resolution to obtain the most relevant information. In the case of SOFCs, the challenge lies in being able to probe the TPB region and obtaining information relevant to the TPB, even though it is the same composition as the bulk. Since the TPB region is relatively much smaller, an overwhelming portion of the signal comes from the bulk. It is not a trivial task to separate contributions from each and experiments must be designed with maximizing the desired signal in mind. For example, since the beam spot size is generally fixed, samples should prepared with an architecture that is a compromise between maximizing TPBs for the beam spot size and remaining relevant to the architecture of actual operating fuel cells.

The third key challenge is studying the reaction under *in situ* and operating conditions. Since the conditions of operation are so far from the typical conditions for characterization, the information from *ex situ* experiments does not accurately represent the actual material state during operation. Even the preparation of a sample for *ex situ* characterization itself can introduce contamination that confounds the analysis. There are already multiple requirements for SOFC operation, which are temperature, controlled gas atmosphere, and electrical connection. To further complicate the experiment, synchrotron x-ray spectroscopy has its own requirements for effective data collection, which can directly conflict with the optimal arrangement for SOFC operation. Using a spectroscopy that relies on x-ray fluorescence requires an open cell design which maintains the experimental conditions while allowing x-rays

to pass through windows, interact with the sample, and exit through additional windows. A fluorescence detector is most efficiently positioned as close to the sample as possible to capture the largest solid angle of x-ray fluorescence but proximity to the sample at high temperature can damage the detector or prevent it from collecting data efficiently.

These challenges must be addressed for any *in situ* or *operando* experiment to be successful. In the Technical Approach chapter, x-ray core-hole spectroscopies and x-ray scattering techniques aimed at meeting these challenges are discussed in detail. The unique combination of the information generated from these characterization tools provides insightful perspectives on understanding the behaviors of complex SOFC materials.

CHAPTER III

TECHNICAL APPROACH

3.1 Basic electrochemical characterization methods

Electrochemical tests and impedance spectroscopy are common techniques in SOFC research to establish a performance baseline and standard for comparisons. With the in-house equipment and expertise, these tests are the primary tool for identifying the most interesting compositions and phenomena before conducting more resource-intensive investigation through spectroscopy. Electrochemical tests involve determining the peak power output of a full cell, temperature dependence of the peak power output, and the open-circuit voltage behavior as a function of time. Electrochemical impedance spectroscopy can be used via circuit modeling for identifying different components of the overall cell resistance and providing initial clues about the mechanisms of poisoning. Both are tools that can rapidly screen for promising materials as candidates for next-generation anodes, cathodes, electrolytes, and other SOFC components.

The most basic test for an SOFC's viability as a testable sample is measuring the open circuit voltage (OCV) or potential (OCP). The OCV measures the theoretical maximum voltage that a cell can produce when a chemical potential is put across the cell (fuel on the anode side, air on the cathode side) before considering all possible sources of resistance. Generally, it provides a good measure of the health and quality of the cell, particularly of the electrolyte. If there is a pinhole leak in the electrolyte or sealant that reduces the chemical potential, it will be reflected by a lower OCV. Similarly, an electrical short between the anode and the cathode will result in a low OCV. Thus, without applying any potential or current, the OCV is a simple and

rapid electroanalytical method that can determine whether a specific sample cell is viable for testing.

To measure peak power performance, linear sweep voltammetry (LSV) can be employed from the OCV to 0.6 V. The product of the current measured and the voltage is the power output in watts, which is then normalized by the geometric area (not the true surface area) of the cathode. The resulting curve will be a parabola that reaches a peak within the LSV voltage window. The peak power density is frequently reported as a measure of the promise of candidate SOFC materials. Like the OCV test, once the operating/testing conditions have been reached, the test is rapidly conducted and can quickly screen many different materials for promising performance.

Lastly, one major electroanalytical method used for stability is chronoamperometry, which is the measurement of current density over time, typically for at least hundreds of hours. Chronoamperometry is useful for tracking the stability of a SOFC as it performs in true operating conditions, particularly as contaminants are introduced into the gas stream. Other behaviors like activation, where current density increases gradually over time, and degradation, which may be intrinsic to the cell or extrinsically caused by introduced contaminants, can also be readily tracked and studied. Stability measurements require significant time and resources, but provide a clearer picture of the problems, capabilities, and commercial prospects of SOFC design and materials. Phenomena like degradation and activation also serve as focal points which may motivate deeper investigational studies, such as those that utilize spectroscopy.

For the above and most other electroanalytical methods, a potentiostat is used to apply and measure potentials and currents. Electrochemical impedance spectroscopy, on the other hand, also requires a frequency response analyzer to work in conjunction with a potentiostat. This is because it uses an alternating current signal of varying

frequency to probe the electrochemical characteristics of the SOFC. Although the capacity for circuit modeling is very deep when dealing with EIS, it can be difficult to be rigorous and time-consuming to explore. The EIS data can still be, and is frequently, taken at more of its face value for calculating the ohmic and polarization resistance by measuring the displacement and diameter of semicircle arcs. Like chronoamperometry, these values can help track and indicate stability issues that occur over time or from introduced contaminants.

3.2 Basic structural and morphological methods

Scanning electron microscopy (SEM) is a common scientific research tool for studying morphology, roughness, particle size, elemental analysis, and other physical surface characteristics. Although the electron probe requires high vacuum to operate, SEM can reach resolutions on the order of nanometers, allowing it to observe morphological features much smaller than resolvable by optical microscopy yet with less difficulty than transmission electron microscopy. Additionally, at high accelerating voltages, typically 15 kV and higher, the electrons in the probe have sufficient energy to excite or "kick out" core and valence electrons, leaving electron holes that are filled by higher orbital electrons. The fluoresced x-ray resulting from the change in the orbital electron's energy can be filtered into an energy-discriminating detector for elemental analysis, a process termed energy-dispersive x-ray spectroscopy (EDS). Combined with the high spatial resolution of SEM, EDS can provide linescans and maps of elemental distribution. Details on the mechanism of SEM and EDS are readily found in reference textbooks.

Another common research tool is laboratory-scale x-ray diffraction (XRD), which is typically used to determine crystal structure and phase purity. Because of its wide applicability to crystalline or semi-crystalline materials and rapid data collection, XRD is a well developed technique, to the point of being capably used as a black box

instrument. With the right knowledge and software, a deep amount of information can be extracted from diffraction patterns if deemed valuable, but XRD serves the purpose of screening sample quality and phase purity just as well. The theoretical basis of XRD is well documented and how it specifically pertains to synchrotron x-rays is discussed later in the thesis.

3.3 Principles of core-hole spectroscopies

There are several methods that are commonly used to narrow the data collection to a spatial region of interest. For morphological purposes, electron microscopy has sufficiently high spatial resolution but generally lacks information related to the crystal structure and electronic state. Techniques like x-ray photoelectron spectroscopy (XPS) can have moderate lateral spatial resolutions on the order of tens of microns and specialize in being highly sensitive to the surface, typically probing the top few nanometers. By using precise synthesis methods and idealistic model geometries, gas-solid interfaces and TPBs can be studied for fundamental studies. However, these typically thin film and patterned microstructures do not represent microstructures and environments encountered in real systems. Additionally, techniques like XPS usually require ultra high vacuum (UHV) conditions, which lead to complicated, but not impossible, *in situ* and *operando* experiments. To augment these techniques, XAS provides a wealth of electronic and, more importantly, local atomistic structure on the scale of nearest neighbors. Pair distribution function is the complement to XAS, trading elemental-specificity for greater information fidelity and longer-range measurements of the local structure but is itself not a core-hole spectroscopy. Both XPS and XAS use different photon energies and probe different electron orbitals in atoms to yield information, as depicted in Figure 1.

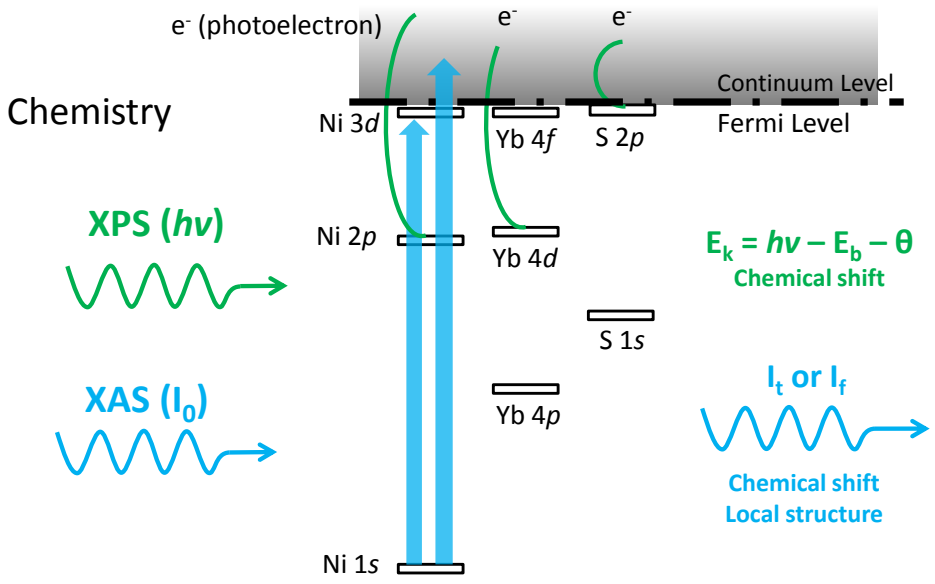

Figure 1: Diagram of how x-ray core-hole spectroscopies (XPS and XAS) promote electrons into different states, the type of signal measured, and the information gained. Due to different photon energy requirements, these spectroscopies are not typically done at the same time.

3.3.1 X-ray photoelectron spectroscopy

Many characterization techniques obtain information from both the bulk and the surface of a material but cannot distinguish their individual contributions to the overall signal. While the bulk properties are essential to understanding materials properties, studying surface phenomena is important because significantly different mechanisms may be active and exerting considerable influence on a material's overall performance. X-ray photoelectron spectroscopy is one of the best suited techniques for studying the chemical and electronic structure of surface species.

3.3.1.1 Theoretical basis

As its name indicates, XPS uses incident x-rays to excite electrons into the continuum, where they become photoelectrons and escape the material. The energy of the incident x-ray, typically Mg K-alpha (1254 eV) or Al K-alpha (1487 eV), is sufficient to overcome the the binding energy of electrons of most elements and impart significant kinetic energy to the photoelectron. These parameters are related in Equation 3,

$$h\nu = E_{KE} + E_{BE} + \phi_{detector} \tag{3}$$

where $h\nu$ is the energy of the incident x-ray photon, E_{KE} is the kinetic energy of the photoelectron referenced to the vacuum level of the spectrometer, E_{BE} is the binding energy of electron referenced to the Fermi level, and $\phi_{detector}$ is the work function of the spectrometer. Since the spectrometer measures the kinetic energy of the photoelectron and the x-rays are monochromatic, the initial binding energy of the photoelectron can be determined, yielding information about an element's chemical state and bonding.

3.3.1.2 Experimental considerations

Incident x-rays are capable of exciting a wide variety of core and valence electrons (s, p, d, and f-shell electrons), which partially enables XPS to characterize the vast

majority of the periodic table. The other enabling factor is an energy-discriminating detector-analyzer, typically a hemispherical detector with an energy resolution of 0.2 eV or better.

The surface sensitivity of XPS arises from the short inelastic mean free path of photoelectrons with kinetic energies ranging from 500 eV to 1400 eV. Although the inelastic mean free path varies with material, density, and kinetic energy, photoelectrons typically escape from the top 5 nm to 10 nm of a surface; the remaining photoelectrons are scattered by the sample bulk. Thus, electronic information from surface species is collected without the need to subtract the bulk's contribution to the signal.

The price of such surface sensitivity is that the sample must be probed under very high or ultra high vacuum. Vacuum is necessitated by the short inelastic mean free path of the photoelectrons, which must be collected for the data. The vacuum requirement has implications for the sample and the scope of feasible experiments. Consequently, *in situ* experiments with atmospheric pressures are mostly unfeasible, but compromises can be made. Some experimental conditions like temperature and electrical polarization are possible depending on the endstation equipment. However, sample-gas interactions cannot easily be probed *in situ*, although using a "pump-probe" type of experiment is a viable alternative. The pump-probe design philosophy originated from light-matter interaction experiments involving two lasers, one which would energize the sample into an excited state (the "pump") and a second laser which would probe the excited state before relaxation occurred (the "probe"). While the lasers are typically controlled to pump and probe at very high time resolutions, the same design philosophy can be applied to any type of experiment where the stimulating and probing events occur asynchronously but with sufficient speed relative to the relaxation timescale. In a UHV x-ray pump-probe experiment, the vacuum chamber is backfilled with the reactive gas of interest (the "pump"), evacuated again

to instrument vacuum levels to collect the spectrum (the "probe"). This type of vacuum-based pump-probe experiment relies on the assumption that the reaction between the reactive gas with the sample is irreversible or sufficiently quasi-irreverisble so that when the gas is evacuated again, the change in the sample is preserved long enough for the x-ray to probe the sample.

3.3.1.3 Advanced XPS techniques

A recent advancement for *in situ* XPS has been the development of ambient pressure XPS or AP-XPS. This technique has three specific aspects that enable an x-ray probe to excite photoelectrons from a sample and collect them at pressures many orders of magnitude higher than ultra high vacuum and only a few orders of magnitude or fewer from ambient pressure. First, a specialized detector-analyzer system uses differential pumping and photoelectron-focusing lenses to collect the photoelectrons and maintain the pressure difference between the sample and the detector. Second, the inlet aperture is brought very close to the sample to maximize the solid angle and the collection of photoelectrons. Lastly, a highly focused, high flux synchrotron x-ray beam, which compensates for the loss of x-rays due to gas absorption and the loss of photoelectrons due to a short inelastic mean free path, is brought in at a glancing angle to accommodate the photoelectron inlet aperture. It is important to note that a synchrotron is only part of the requirement for AP-XPS; many of the significant challenges of AP-XPS are the vacuum chamber and detector-analyzer equipment.

By combining the XPS with an ion gun, samples can be gradually sputtered and photoelectrons periodically collected to obtain a depth profile of the chemical states of various elements. This type of experiment is useful to examining the regions near surfaces and interfaces to determine gradients in the chemical composition, especially if phases tend to segregate in those regions. However, sputtering is a destructive process that introduces defects from ion bombardment and embedding and may be

slow with common Ar ion sources depending on the sputtering yield of the sample.

An alternative to destructive sputtering is to the use of a synchrotron light source. In contrast to the energy of a fixed source, a synchrotron light source provides a large range of selectable energies. By increasing the incident photon energy, more kinetic energy can be imparted to photoelectrons, elongating the inelastic mean free path so that photoelectrons are detected from deeper within the material. Conversely, by decreasing the incident photon energy, the inelastic mean free path is decreased and the data are more sensitive to the signals coming from the surface. Thus, synchrotron-based XPS enables a method for non-destructive depth profiling of chemical and electronic information. The danger of using a variable incident photon energy is that the photoionization cross-section of each element will vary with energy and some photon energies chosen may be insufficient to exceed the binding energy of some electrons or resolve them from the inelastic background, particularly those with low photoionization cross-sections.

3.3.2 X-ray absorption spectroscopy

Other x-ray spectroscopy methods can also provide chemical and electronic information like other electron-based spectroscopies without necessarily requiring UHV conditions, but often at the cost of surface sensitivity. X-ray absorption spectroscopy (XAS) is an x-ray characterization technique that is of significant value because it can selectively provide unique atomic, electronic, and local structural information.

3.3.2.1 Theoretical basis

X-ray absorption spectroscopy relies on having a energy source from which x-rays of a specific energy can be selected. The predominant form of XAS involves using a synchrotron light source, which provides extremely bright x-rays of a very wide bandwidth of energy (known as white light for its mixture of wavelengths), and a double-crystal

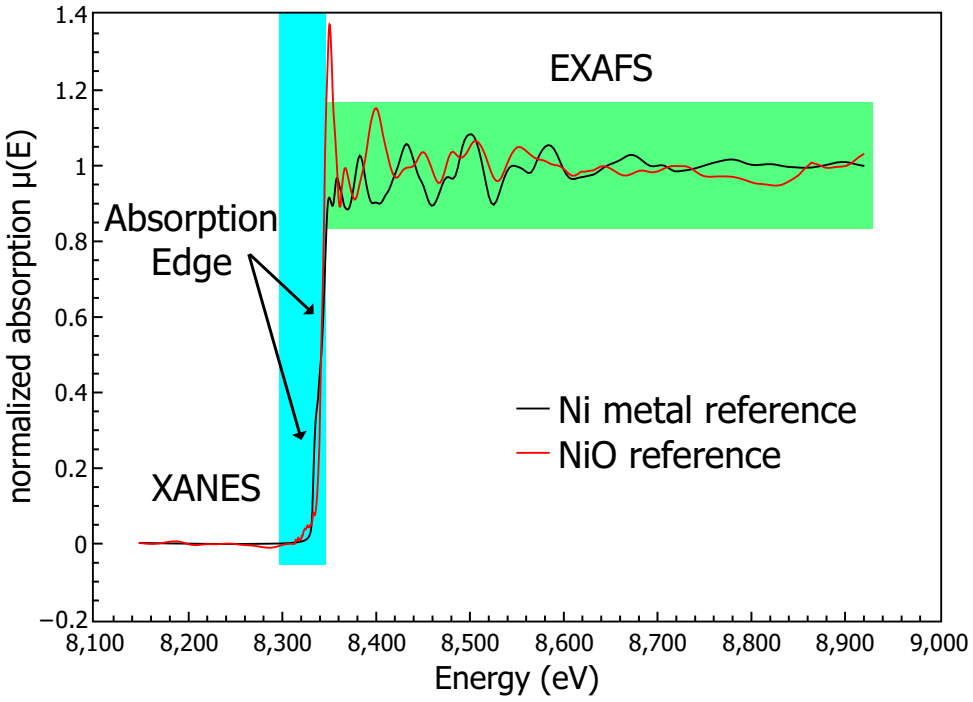

Figure 2: Typical XAS spectrum of Ni metal foil.

monochromator to diffract a specific x-ray wavelength onto the sample. As the x-ray beam scans through energy, it eventually reaches a resonant energy that excites core electrons to higher, unoccupied orbitals and eventually, the continuum, where they are termed "photoelectrons". These two phenomena have particularly distinct absorption responses and are typically distinguished as the x-ray absorption near-edge structure (XANES) and the extended x-ray absorption fine structure (EXAFS) regions. An example of a typical XAS spectrum is shown in Figure 2.

At a sufficiently high incident photon energy, the number of excited core electrons will increase sharply, resulting in a rapid increase in absorbance. The inflection point of the absorbance is identified as the "absorption edge" while the point of maximum absorbance, if it forms into a sharp peak before oscillating, is termed the "white line". This spectral feature will vary in shape, size, and fine structure depending how the atom's electron configuration affects the outgoing photoelectron. Because of its importance and rich information, researchers call the energy range about 50 eV

above and below the absorption edge the "XANES" region or the near-edge x-ray absorption fine structure (NEXAFS).

The absorption edge energy depends on the binding energy of the core electrons, which in turn depends on oxidation state. A higher (i.e., more positive) oxidation state is caused by the removal of the outermost electrons, resulting in a stronger, unbalanced electromagnetic force from the positively-charged atomic nucleus. The binding energy increases accordingly and thus the core electron excitation process requires a slightly higher energy photon. The maximum absorbance in the white line depends on the density of unoccupied states. That is to say, the increase in x-ray absorbance depends on the density of unoccupied states that the excited core electrons can fill. An additional pre-edge peak can be observed if the absorbing atom has hybridized electron orbitals that enable otherwise forbidden transitions at lower photon energies. Consequently, the XANES spectral energy, shape, and intensity depend strongly on the electron configuration of the element being investigated. Analysis of the XANES spectrum can uniquely resolve information such as orbital hybridization, density of unoccupied states, and oxidation states.

As the incident photon energy increases, the spectral signal begins to exhibit oscillatory behavior, which is termed the "EXAFS region" and typically extends to 1000 eV above the absorption edge. Within this energy range, photoelectrons are continuously generated, escaping the absorbing atom with sufficient kinetic energy to impinge upon neighboring atoms. The photoelectrons can be envisioned as spherical waves emanating from the absorbing atom. When the spherical waves encounter neighboring atoms, they become backscattered. The resulting constructive and destructive interference of the incident and backscattered photoelectron waves result in the post-edge absorbance oscillations. Figure 3 illustrates how interference of backscattered photoelectrons translate to post-edge absorbance oscillations. Neighboring atoms of different distances from the absorbing atom will backscatter

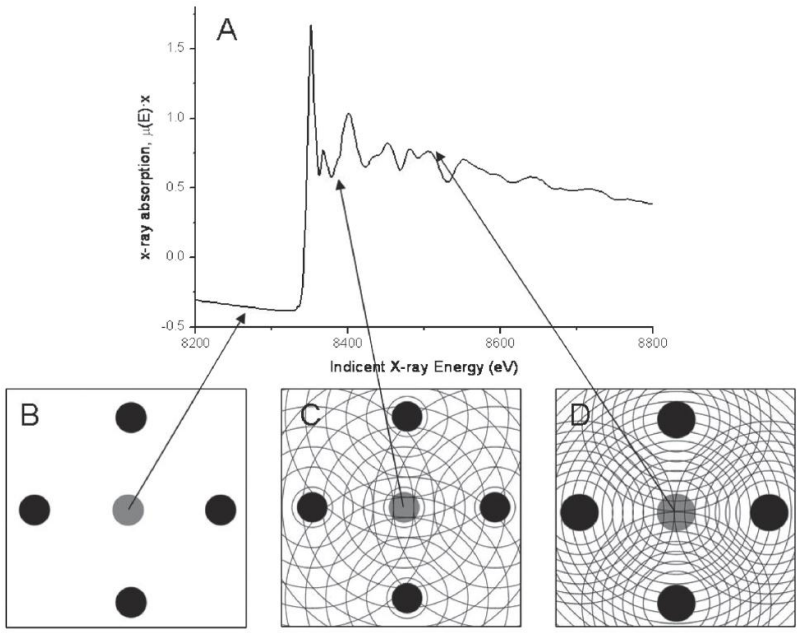

Figure 3: The atomic and local structure analogues to different parts of the XAS spectrum, using the Ni K-edge of NiO as an example. Reproduced from Kelly *et al.* [30].

photoelectrons of different frequencies. With Fourier transforms and other data processing tools, the EXAFS region can yield a function that is proportional to the radial distribution function, which contains information about the local structure and its configurational geometry. The end results are element-specific information about the local atomistic structure and, because the XAS technique averages data over the bulk, a sense of the degree of order and disorder in the bulk.

The function in EXAFS region can be described with the following equation [30]:

$$\chi(k) = \sum_i \chi_i(k)\chi_i(k) = \frac{N_i S_0^2 F_{eff,i}(k)}{kR_i^2} \sin(2kR_i + \phi_i(k)) e^{-2\sigma_i^2 k^2} e^{\frac{-2R_i}{\lambda(k)}} \tag{4}$$

where $\chi_i(k)$ refers to the contribution to the overall absorption for each photoelectron scattering path i as a function of k. R_i is defined as

$$R_i = R_{i,initial} + \Delta R_i \tag{5}$$

and k is simply the wavenumber converted from energy-space using the following

relation:

$$k^2 = \frac{2m_e(E - E_0 + \Delta E_0)}{\hbar} \tag{6}$$

where m_e is the mass of an electron and $\hbar$ is reduced Planck's constant.

Overall, the EXAFS equation can be compartmentalized as a sinusoidal function with its amplitude modified by a structural pre-factor, two exponential post-factors, and a phase shift term within the sinuisoidal function. The structural pre-factor accounts for each path's coordination degeneracy (N_i), the passive electron reduction factor (S_0^2), and effective scattering amplitude ($F_{eff,i}(k)$), which is calculated *ab initio* by a software code called FEFF6. The first exponential post-factor accounts for mean-square displacement of the bond length due to static and thermal disorder (σ_i^2) while the second exponential post-factor accounts for the inelastic mean free path of the scattering photoelectrons ($\lambda(k)$). Variation in the path length from an idealized structure is represented by ΔR_i. The $\phi_i(k)$ term in Equation 4 is the phase shift term for the photoelectron, which, if corrected for, will translate the EXAFS spectrum to higher R distances. Detailed explanation of all the terms can be found in Kelly *et al.*'s work [30], but the terms highlighted above will be used later in the section 3.5 for data analysis.

3.3.2.2 Experimental details of XAS

Experimentally, XAS is measured in two common configurations, each with its advantages and disadvantages. The most ideal configuration is transmission XAS, because it captures the essential information (x-ray absorbance as a function of energy) with the least amount of noise or confounding factors. Transmission XAS follows the Beer-Lambert Law:

$$I_t = I_0 * exp(-\mu * x) \tag{7}$$

To measure the absorbance per length (μ) of a material as described by Beer's

Law, a detector measures the incident x-ray photon intensity (I_0) before the sample and another detector measures the x-ray photon intensity transmitted through the sample (I_t). For calibration purposes, a reference material, described later, and another detector (termed I_r or I_{ref}) further downstream from the sample are also used. By comparing the ratio of two consecutive intensities measured by the detectors and taking the natural log thereof, one can determine the absorbance A of the material between the detectors, assuming negligible absorption by the atmosphere in the beam's pathway. This is illustrated using a rearrangement of the Beer-Lambert Law:

$$A = \mu * x = ln\frac{I_0}{I_t} \tag{8}$$

For the beamline experiments at the National Synchrotron Light Source (NSLS), ionization chambers were used as detectors to measure the x-ray photon intensity. They are relatively simple in construction and, given the proper mixture of common laboratory inert gases, provide useful applicability over a very large range of x-ray energies, which makes them prevalent at facilities like synchrotrons. In an ionization chamber, two parallel plates are positioned along the beam path so that the x-rays travel between them. The chamber is sealed and filled with a mixture of helium, nitrogen, or argon depending on the energy of the incident x-ray. The proportions of the gas mixture affect how many x-rays in the beam are absorbed, as their photoionization cross-section varies with atomic mass and the energy of the incident radiation. The incident radiation ionizes the gas, creating oppositely charged ion pairs, which are attracted to the parallel plates according to the electric field put across them. Contact and electron exchange between the ion pairs and the electrically-charged plates allows a very small current to be measured (typically in the nanoamp and picoamp range). With this information, an I_0 current can be monitored and compared to the current in a downstream detector. Typically, the gas mixture needs to be adjusted for I_0 calibration such that sufficient amounts of gas are ionized into pairs to generate

a detectable level of current but enough photons are preserved to interact with the sample and also ionize the gas in downstream detectors. Various software calculators for this calibration are available for use.

The reference material is usually a high purity metal or alloy which contains an element with a strong absorption edge in the energy range of study. For example, if one wants to study the XAS of iron oxide, one would likely use an iron foil as the reference material. The same element as that contained in the sample does not always need to be used, particularly when stable, high purity forms of an element of interest may not exist or be available. For the purpose of a reference material, any material can be used (in the above example, iron oxide itself could be a reference) as long as the material is well known and well characterized such that the data can be aligned in energy space to known values in literature. Generally, however, metal foils are the best reference materials available.

The above description of the beamline and ionization chamber detectors assume full use of the Beer-Lambert law, as mentioned, for transmission XAS. Transmission mode XAS is always the ideal configuration because it provides the purest information (material absorbance) with minimal intrusion of noise and confounding factors. Transmission XAS relies on a few assumptions of sample in order for the spectra to be obtained and trusted. First, the sample must have a sufficiently low mass attenuation length so that a measurable intensity of x-rays are transmitted through the sample and measurable in the downstream detector. The mass attenuation length is the length of a sample through which the x-ray intensity decreases by $\frac{1}{e}$ and is based on the sample's density, atomic mass, atomic photoabsorption cross-section, and x-ray wavelength. Second, the sample must contain a sufficiently high concentration of the absorbing element such that there is significant, measurable difference in the intensity of the x-rays before and after the sample. In some situations, this requirement may conflict with the first, but workarounds exist. Thirdly, the sample must be uniform in

composition on the scale of the beam spot size. All of these assumptions are aimed at obtaining the best possible signal-to-noise ratio and avoiding potential confounding factors that can skew or bias the data.

However, frequently, there are experimental limitations or sample constraints that prevent transmission XAS from being used. An archetypal example is a geological sample which cannot be separated from its thick substrate without risk of contamination. In such a case, transmission through a thick, highly absorbing substrate is impossible. Fluorescence XAS is an alternative configuration to transmission XAS which can be employed for these situations. In fluorescence XAS, instead of measuring the x-rays transmitted through the material in a downstream detector, a perpendicular fluorescence x-ray detector is used, which measures the characteristic x-rays generated from higher energy orbital electrons filling core electron holes left behind from x-ray excitation. Once the incident x-ray energy reaches the absorption edge, fluorescent x-ray events also rapidly increase from all of the core holes being filled.

The difficulty with fluorescence XAS is that many different fluorescence events of many different energies occur, based on the composition of the sample. At high energies above the absorption edge, other elements in the sample will also fluoresce x-rays; additionally, alpha and beta lines will fluoresce separately. While the alpha line will be the most dominant fluorescence, other unrelated fluorescence will reduce the signal-to-noise ratio. Energy discriminating fluorescence detectors or physical filters can be employed to improve the signal-to-noise ratio at the expense of experimental resources and increased complexity, but even these instruments have limitations. For example, the x-ray fluorescence lines of Ni K-alpha (7478.15 eV) and Yb L-alpha (7415.6 eV) are so near each other that a fluorescence detector may not be able to adequately resolve them. Besides extraneous fluorescence affecting the signal-to-noise ratio, "self-absorption" of fluoresced x-rays can be an issue in thick samples with compositions concentrated in the element of interest. Strong over-absorption of the

x-rays, akin to photon saturation, causes a loss of the fine structure details that are vital for useful information. Nevertheless, fluorescence XAS is useful because it can succeed where transmission XAS falters, optimally in very thin samples (e.g., monolayers) and dilute concentrations of an element of interest (as low as ppm) in thick samples. In these cases, data must be averaged over long collection times and/or many scans to obtain a high quality.

Hybrid forms of transmission and fluorescence XAS are uncommon but are possible. Generally, it requires a specialized setup and a very large beam spot size that can physically divided so that it serves both transmission and fluorescence XAS simultaneously. The unique advantage of a hybrid technique is that a reference foil can be used in conjunction with fluorescence XAS, which normally isn't possible. This allows the energy to be accurately calibrated and for energy shifts to be trusted.

X-ray absorption spectroscopy is more common for an *in situ* technique because of the high penetrating power of high energy x-rays allows it to probe ambient, high pressure, and high temperature environments. However, its unique abilities are in its ability to obtain local atomistic structure information through the EXAFS region. This information has been exploited by other researchers, for example, to understand oxygen vacancy and coordination in SOFC electrolytes [66] and distortion of octahedral coordination in SOFC cathodes [50, 57]. The length-scales at which XAS can probe, the nuanced distortions in the local coordination, and the range of experimental capabilities make XAS a valuable core-hole spectroscopy technique.

3.3.2.3 Applications of XAS

Yildiz and co-workers studied activation of two cathode materials, $La_{0.8}Sr_{0.2}MnO_{3-\delta}$ (LSM8020) and $La_{0.8}Ca_{0.2}MnO_{3-\delta}$ (LCM8020), on single crystal YSZ electrolytes using *in situ* XANES (Mn K-edge and La L_{II}-edge) and X-ray reflectivity [86]. Cathode

activation, also known as current conditioning, is the process of applying a dc polarization to achieve a permanent performance enhancement in the oxygen reduction reaction. XANES data revealed that, contrary to the prevailing hypothesis, Mn was not affected by the current conditioning, in neither porous or dense thin-film samples of LSM8020 or LCM8020. The La L_{II}-edge however in LCM8020, revealed a decreasing trend in intensity with cathodic polarization, implying an active role of La with oxygen reduction processes but only at the surface, since the trend was only observed below the critical angle of reflectivity. X-ray reflectivity was used to study the cathode/electrolyte interface with depth-sensitivity by controlling the angle of incidence with a Huber six-circle goniometer. Near the critical angle for total external reflection, evanescent waves cause X-ray fluorescence from only near the interface, since the X-rays are otherwise reflected from the substrate. X-ray reflectivity was also used to study the internal roughness between the cathode and electrolyte. The *in situ* configuration was achieved by using an infrared heating cone with apertures for the beam and fluorescence detector.

A similar study was done by Chang *et al.* using similar equipment and total reflection X-ray fluorescence on epitaxial thin film LSM on single crystal YSZ [7]. In this particular study, the focus was on Sr segregation into 10 nm to 40 nm surface particles, detected by AFM, which was found to occur at room temperature. Both annealing and cathodic current conditioning revealed reduced Sr segregation, with annealing resulting in more uniform distribution than current conditioning, as the sheet resistance limits the electrically active area to the Pt contact wires.

Melo *et al.* conducted an XAFS study of compositions of $La_{1-x}Sr_xMnO_3$ with varying Sr content and emphasis on the local structure of Sr and Mn [50]. At the time of publication, 2006, they touted it as one of the first studies on LSM as prepared by pyrolysis of polymeric precursors. Using a Si(111) monochromator and three ionization chambers at Brazilian Synchrotron Light Laboratory (LNLS), they studied

the Sr and Mn K-edges under *ex situ* conditions at room temperature in transmittance mode. In general, they obtained information about MnO_6 octahedron distortion as a function of Sr content from 0 to 0.6. FEFF calculations were used to get numerical values for Mn-O octahedrons. In the k^2-weighted signal, decreasing the Sr content dampened the Mn signal. From the Fourier transforms of the k^2-weighted data, an increase in Sr content is correlated with an increase in amplitude of the peak R = 1.6 Å, which corresponds to the Mn-O bond and first shell of nearest neighbors. The shorter peak between 2.5 Å and 3 Å corresponds to the Mn-La/Sr bond, which becomes longer with increasing Sr content and more intense, which indicates more ordering of the overall structure. The structure from 1 Å to 7 Å had the same features but different intensities. In the Sr K-edge FT, there were two peaks observed for Sr-O and Sr-Mn, respectively. As Sr content increases, Sr-Mn coordination and bond length decreases, according to FEFF fitting. Oxygen temperature-programmed desorption shows that less oxygen desorbs with higher Sr content. In Mn K-edge XANES, shift in edge energy points to an oxidation state change in Mn to compensate Sr^{2+} replacing La^{3+}. A post-edge oscillation is interpreted to be further evidence of the Mn-Mn bond lengthening and structural ordering by shifting to lower energies along with increasing Sr.

X-ray absorption spectroscopy has the unique capability to identify oxidation states and local coordination, which fundamentally affect chemical and electronic properties. A soft x-ray experiment by Braun and co-workers examined the O K-edge and Fe L-edge in $La_{1-x}Sr_xFeO_3$ at room temperature and under ultra high vacuum (5×10^{-10} Torr) [4]. Small variations in the $2p_{3/2}$ t_{2g} shoulder and e_g peak heights for both $2p_{3/2}$ and $2p_{1/2}$ were based on substitution of Fe with 10% or 20% Ti or Ta. The resulting oxidation state change and unit cell expansion caused Fe^{3+} to adopt a high spin electron configuration and a tetrahedral coordination compared to the octahedral coordination of Fe^{4+}. In the oxygen pre-peak region, they inferred

information about Fe $3d$ and La $5d$ empty bands because of hybridization with O $2p$ orbitals. After deconvoluting the O K-edge prepeaks into individual t_{2g} and e_g spin up and spin down bands, they discovered a correlation between a ratio of peak heights and conductivity and the Fe^{4+}/Fe^{3+} ratio.

3.3.2.4 Frontiers and challenges in XAS

Using XAS to uniquely obtain structural information with elemental specificity and on a scale of angstroms averaged over the whole bulk helps answer hypotheses about chemical mechanisms, changes in structural ordering, and other phenomena observed in SOFC materials. Without XAS, understanding would be limited to the surface information obtained by XPS and generalized bulk crystal structure information from x-ray diffraction (XRD). Furthermore, *in situ* and *operando* experiments are vital to fully understanding how complex materials are affected by complex operating conditions, particularly when corresponding *ex situ* experiments fail to capture the effect of interdependent relationships, such as between chemical gas and electrical potential. The goal is to observe the effects that the true operating conditions, including temperature, partial pressure of reactive or poisoning gases, and oxidizing or reducing conditions. *Operando* spectroscopy is essential for providing insight into the reaction mechanisms and information for the rational design of novel materials [41].

Low atomic number elements are inherently challenging to study in bulk phases, because of their low x-ray fluorescence yields. After a core hole is created from photon absorption, the hole may be filled by a radiative or nonradiative relaxation process. A radiative process means that a fluorescent x-ray will be emitted as a higher energy electron falls down to fill the core hole. A nonradiative process is one in which the relaxing electron transfers its energy to another electron, which is then ejected and termed an "Auger electron". The proportion of radiative and nonradiative processes depends on the atomic number of the absorber. For low atomic number elements

with few electrons, the relaxation is overwhelmingly dominated by the nonradiative process and thus, the generation of Auger electrons, so electron detectors must be used to obtain good signal-to-noise ratios. Because electrons have a much shorter inelastic mean free path than radiated x-rays, information on low atomic number elements is thus constrained to the surface.

3.4 X-ray diffraction and pair distribution function

X-ray diffraction (XRD) is a workhorse of materials science, providing rapid crystal structure information with high fidelity. Much about XRD has been studied and developed since first proposed by Bragg and Bragg in 1913, but this discussion will focus on the advantages of using synchrotron radiation in the context of Bragg's law. Pair distribution function (PDF) is closely related to XRD and most aptly described by Takeshi and Billinge as the data "underneath the Bragg peaks" [73] since it is based on the diffuse scattering intensity.

3.4.1 Theoretical basis of XRD

In XRD, incident x-rays are diffracted by the regular spacing of atoms in a crystal when they impinge upon the crystal at a specific angle. As the angle changes, the intensity of the diffracted x-rays varies because the outgoing x-rays may interfere constructively or destructively depending on their phase, which originates from the spacing of the diffracting planes. When the phase difference between diffracted x-rays is 2π, the x-rays constructively interfere and generate an intense peak signal in the detector. The conditions for a diffraction peak depend on the wavelength of the x-ray (λ) or an integer multiple thereof (n), the incident angle (θ), and the distance between atomic planes in the crystal (d). These parameters are related together by Bragg's Law, shown in Equation 9.

$$n\lambda = 2d\sin\theta \tag{9}$$

3.4.2 Applications of XRD

X-ray diffraction (XRD) is a widely used tool to determine fundamental information such as phase identification, phase stability, and crystal structure. It has a wide range of applications and is capable of studying many different types of materials. The technique can be adapted for *in situ* experiments, which is not uncommon in the literature. Furthermore, a synchrotron light source's extremely high flux enables fast time-resolved studies.

While XRD has already been proven to be invaluable for attaining crystallographic information, synchrotron-based XRD offers unique advantages and information. From the native brilliance of the synchrotron light, diffraction patterns can be collected quickly for finely time-resolved experiments of transient phenomena. Several examples of how *in situ* synchrotron XRD can observe phase changes and inform materials design are offered by Shen and co-workers [69]. They studied the phase transformations of mixed-valence β-MnO_2 during hydrothermal synthesis and could observe the temperatures at which the diffraction peaks grew or shrank as a result of changes in crystal structure. The results led to future syntheses at key temperatures and distinct morphologies were observed under electron microscopy. By studying the parameter space, the authors could tailor the specific surface area of synthesized mixed-valent β-MnO_2.

Liu and Almer conducted a phase and strain mapping study through XRD of a conventional Ni-YSZ/YSZ/LSM-YSZ planar SOFC with gradients of YSZ in the cathode [39]. After operating the fuel cell with chromium-containing ferritic stainless steels to induce Cr poisoning, the fuel cell was cross-sectioned and the layers were characterized using synchrotron x-rays. From this, Cr_2O_3 and $(MnCr)_3O_4$, the Cr-containing contaminants, were identified and mapped. Across the layers in the cross-section, the weight fractions of each phase were calculated using Rietveld analysis and deviatoric strain was quantified and mapped based on changes in the d-spacing.

These results enabled the researchers to propose mechanisms of Cr oxide formation based on location and exclude interconnect geometry as a dependency for where Cr oxides might form. Synchrotron radiation provides both expedited data collection and spatial resolution not found in conventional XRD.

3.4.3 Theoretical basis of PDF

A brief overview of the theory of pair distribution function as a subset of x-ray scattering will be given. A complete and thorough explanation is given by Takeshi and Billinge [73], on which much of this section is based. Like diffraction, the intensity of the scattered x-ray is measured as a function of photon wavelength and scattering angle. The scattering vector **Q** represents the total change in direction and magnitude of the scattered photon. If only elastic scattering is considered, then the magnitude of the **Q** vector can be calculated as follows:

$$|Q| = \frac{4\pi \sin\theta}{\lambda} \tag{10}$$

where λ is the wavelength of the photon and θ is one-half angle of the scattered photon relative to the incident photon. Thus, the magnitude of the **Q** vector results in nm^{-1} or $\mathrm{\AA}^{-1}$ and obtaining high values of Q require both measuring photon intensity at large scattering angles and using photons with small wavelengths. The measured intensity as a function of Q is termed $S(Q)$, or the total scattering structure function. By applying equation 11,

$$F(Q) = Q[S(Q) - 1] \tag{11}$$

a reduced form of the total scattering structure function called $F(Q)$ is obtained. This reduced scattering structure function is then Fourier transformed to convert from reciprocal space (Q-space or momentum space) to real space, resulting in $G(r)$, which is termed the reduced pair distribution function. Except for some proportional factors accounting for the bulk density of the material and a vertical offset, the $G(r)$ function is analogous to the radial distribution function in describing local structure

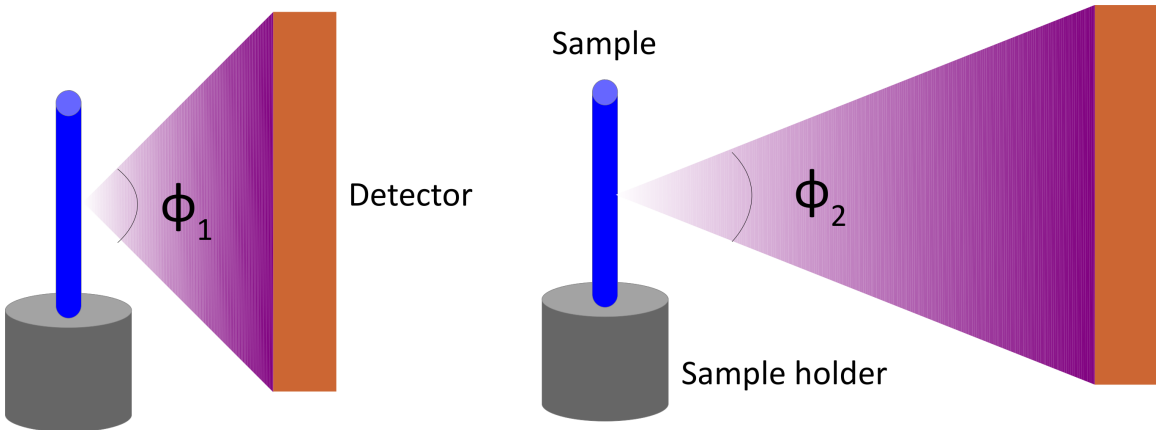

Figure 4: Different distances affect the ϕ or 2θ angle. For PDF, the configuration on the left is more favorable.

except it is in a form such that uncertainties in the data are not dependent on the r-value. Additionally, compared to EXAFS, the quality of the data in PDF is not affected by the multiple scattering or inelastic scattering of a photoelectron and thus does not decay at longer distances. At this point, the $G(r)$ can be used for qualitative interpretation and discussion of evolving features.

3.4.4 Experimental considerations of PDF

Given the typically very high energy of x-rays used in PDF, most samples are generally thin enough that absorption will not impede elastic scattering. For 2-dimensional (2-D) area detectors, a balanced consideration must be taken when determining the distance from the sample as a closer distance will enlarge the 2θ angle but the fixed size of each charged-couple detector pixel also means that a closer distance will result in a lower resolution of 2θ. This effect of distance on angle is well illustrated in Figure 4.

For *in situ* experiments, specialized setups are used to control the temperature and gas environment while minimizing the absorption and scattering effects of the x-ray probe. One example of how to achieve these requirements simultaneously is shown in Figure 5. The sample is loaded into a quartz tube along with a thermocouple to

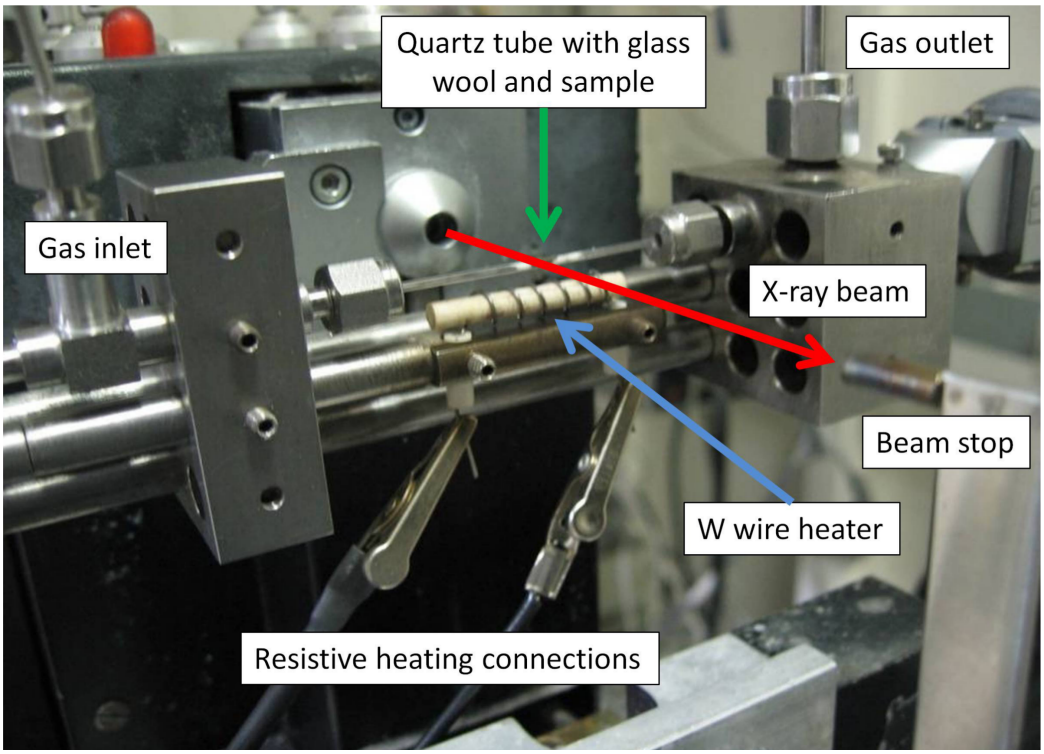

Figure 5: Picture of the X7B experimental setup with descriptive arrows and text for the components that control the gas and temperature. The 2-D area detector is behind the perspective of the camera.

measure the temperature. Glass wool is used to compress and immobilize the sample while the gas flows through the quartz tube. Graphite gaskets are also used inside the nuts to help seal the quartz tube. An alternative wire heating arrangement can be a tungsten wire wrapped around the quartz tube itself but wrapped with an opening for the x-ray beam. Because the beam passes through the quartz tube, measurement of an empty tube is a necessity to PDF data processing.

3.4.5 Applications of PDF

The development of pair distribution function was originally inspired by a need to measure the local structure of amorphous materials, which did not have the long-range, periodic atomic order found in crystaline materials. Thus, the local interactions of metallic glasses and even liquids could be characterized. However, as the technique matured, it became clear that PDF could also provide unique insights into

the behavior of crystalline materials, such as doping in semiconductor materials [58] or order-disorder phenomena in inorganic compounds [23]. The length-scales of the PDF information naturally lends itself to the study of nano-sized materials such as quantum dots [48] or Pt/C fuel cell catalysts [61].

However, applications of PDF toward the study of solid oxide fuel cells are sparse and primarily focus on phenomena related to the solid electrolyte. For example, Coduri and co-workers studied the effect of lanthanum doping in ceria for a lower temperature electrolyte using neutron powder diffraction and pair distribution function [13]. They were able to observe strong doping-induced disorder, which was further exacerbated by exposure to a reducing gas, but is not apparent in the long-range order. As needed for an *in situ* temperature experiment reaching 750 °C, they also tracked the thermal expansion effects on the pair distribution function and thus, could identify evidence of static disorder from dopants and vacancies in the structure.

Mamontov *et al.* also studied nano-scaled powdered ceria but in the context of automotive exhaust emission control [46]. Pair distribution function and neutron diffraction identified interstitial oxygen defects as being the mechanism for oxygen mobility at lower temperatures and why ceria loses its ability to store oxygen after thermal aging. By fitting different model structures of ceria and analyzing their theoretical PDFs, an explanation for the structural shift toward an ideal fluorite could be narrowed down to the high temperature causing Frenkel-type defects to merge with vacancies, resulting in the loss of the oxygen interstitials.

Nevertheless, even as recently as September 2015, it has been recognized in a review paper by Yashima that while recent PDF work on ceria-based materials has been extensive, "further study is required to establish the correlation between the local structure and materials properties such as catalytic activity and oxide-ion diffusivity" [85], properties which are fundamental to the operation of solid electrolytes in SOFCs. Based on a search in the literature, applications of PDF on SOFC electrodes

are even less common and less developed.

3.5 Data analysis software

3.5.1 XAS data analysis

To analyze XAS data, the freely available Demeter software package developed by Ravel *et al.* contains the widely used and robust processing programs, Athena and Artemis, specifically designed for XAS data [60]. Athena is capable of rapidly fitting backgrounds, aligning scans according to reference energies, reducing noise through merging multiple scans and smoothing, and performing Fourier transforms to obtain the EXAFS data. Athena is suitable for all types of XAS data, from soft x-ray NEXAFS of low atomic number elements to hard x-ray XANES of high atomic number elements.

The Artemis software, in conjunction with IFEFFIT, can create and simulate EXAFS data from idealized crystal structures for comparison and more rigorous analysis of the experimental EXAFS data. From a crystallographic information file (CIF), an ideal crystal can be digitally constructed out to a chosen distance in angstroms centered on a chosen absorbing element using a built-in ATOMS program. Within this constructed crystal, x-ray scattering paths from a chosen absorbing element can be calculated using the built-in FEFF problem. Single and multiple-scattering paths are generated in a list with various data about their strength, distance, and multiple-scattering shape characteristics. These paths are then chosen to be included in the simulated fit of the experimental data. Some parameters of the paths are allowed to vary in a controlled manner, which allows the program to iteratively calculate a new fit, adjust the path variables, and recalculate the fit in a process called refinement.

For each path, four major parameters of the EXAFS equation are allowed to vary, denoted as: e_0, δR, S_0^2, and σ^2. The e_0 parameter refers to a fixed energy shift of the entire spectrum. The δR parameter refers to a proportional factor that

modifies the path length, which helps accommodate phenomena like crystal structure deformation. S_0^2 is a pre-factor commonly referred to as the amplitude, as it controls the amplitude of the simulated EXAFS oscillations. As a pre-factor in the EXAFS equation 4, it is multiplied with the degeneracy of a path (N), which is usually fixed based on the crystal structure. As a result, changes in the coordination number, assuming a single scattering path, are reflected by changes in the the amplitude fitting parameter, which represents a product of S_0^2 and N. The σ^2 parameter contains both the static and thermal disorder present in the crystal. Static disorder refers to the displacement of atoms from their crystallographically defined positions, such as vacancies and interstitial defects, while thermal disorder reflects the variation in position due to vibrations of the atoms, otherwise known as the Debye-Waller factor.

When defining the parameters, it is helpful to reduce the number of variables by redundancy, or use the same variable across multiple paths. There are often logical justifications for using variable redundancy. For example, since the spectrum alignment on the energy scale depends on the beam energy calibration done during the experiment, the same e_0 factor can be used for all of the paths. Similarly, it is usually reasonable to assume that σ^2 is consistent for each element, unless there is an expectation of static disorder of a specific site in a specific path. For δR, redundancy can also be introduced but the assumptions of which paths are redundant require prudent judgment and exploration with the quality of the fit and the desired information or hypothesis to be tested. The S_0^2 parameter is usually fit according to each path and further redundancy is at the investigator's discretion.

3.5.2 XANES data analysis

The L-edge XANES of transition metal $2p$ and $3p$ core level excitations can be simulated using CTM4XAS software, which is an abbreviation of Charge-Transfer Multiplet for X-ray Absorption Spectroscopy [71]. It uses a semi-empirical approach to

simulating L-edge spectra with various controls to include core-hole charge transfer effects and other interactions not included in current density-functional theory (DFT) models. Although it can calculate many types of spectra, including XPS and EELS spectra, for the thesis work, it primarily focuses on studying how the L-edge XANES is influenced by changing oxidation state and local coordination, which also affects the crystal field splitting energy.

3.5.3 XRD and PDF data analysis

Since synchrotron XRD and PDF data are typically collected in the same format, the same software can be used to process them. In fact, by using different data processing parameters, XRD data can be extracted from PDF data. To read the data collected using a 2-D area detector, apply masks, and integrate into a line scan, a program called Fit2D is used [22, 21]. This program can also output the data into units for Q (nm^{-1}) for PDF instead of 2θ (degrees) for XRD. For XRD 2θ data, any XRD software, such PANalytical's X'Pert HighScore Plus, can be used to analyze the data and search for matching powder diffraction files (frequently called "PDFs", not to be confused with pair distribution functions). For PDF Q-data, a command-line program called PDFgetX3 [27] is used to convert the Q-data into a $G(r)$ function, also known as the reduced pair distribution function. For further analysis, a model structure can be generated and its PDF simulated for refinement purposes using another software program called PDFgui [20], but this type of effort was beyond the scope of the thesis.

3.6 Summary of x-ray techniques

Table 1 shows the unique advantages and roles of each technique as well as some of their qualitative characteristics for their relative difficulty in conducting *in situ* and *operando* experiments.

Table 1: X-ray core-hole spectroscopies and scattering provide different vantage points and have varying difficulties in conducting *in situ* and *operando* experiments. Naturally, the most difficult experiments to accomplish are also the most novel and have the greatest potential for scientific impact.

Type	X-ray energy	Length-scale sensitivity	*In situ* difficulty	*Operando* difficulty
XPS	1 keV to 5 keV	Surface (nm)	Low (pump-probe), feasible	Feasible
Soft XAS	400 eV to 1200 eV	Surface (nm)	Low (pump-probe), feasible	High
Tender XAS	1.2 keV to 5 keV	Sub-surface (μm)	Moderate	High
Hard XAS	5 keV to >25 keV	Bulk	Low	Feasible
XRD/PDF	Varies; 8 keV (Cu), 39 keV (PDF)	Bulk	Low	Feasible

CHAPTER IV

ELECTRONIC AND LOCAL STRUCTURE ORDERING IN LSM-INFILTRATED LSCF

In this chapter, the goal was to first demonstrate the plausibility *in situ* transmission XAS and then determine how the information from XAS would be useful in deepening our understanding of complex SOFC electrode materials. Additionally, the data analysis and interpretation techniques employed here for XAS are used in later chapters. Although *in situ* transmission XAS is not revisited in later experiments due to its difficulty and limitations, it serves as a conceptual foundation for later iterations of *in situ* and *operando* experimental design.

4.1 Experimental

4.1.1 Fabrication of LSM-infiltrated LSCF cathode

Similar to our cathode fabrication as described elsewhere [45], porous LSCF cathodes with a thickness of 50 µm were prepared by tape casting process using a commercial powder from Fuel Cell Materials [55]. Pellets of 6 mm diameter were punched out and then calcined at about 1080 °C for 2 h to get porous LSCF substrates. The average mass of each LSCF pellet was measured to be 3.84 mg.

To fabricate $La_{0.85}Sr_{0.15}MnO_{3\pm\delta}$ (LSM) coating onto the porous LSCF cathode, appropriate stoichiometric amounts of $La(NO_3)_3{\cdot}6H_2O$, $Sr(NO_3)_2$ and $Mn(NO_3)_2{\cdot}4H_2O$ were dissolved in a mixture of water and ethanol (1:1, vol/vol) to create a 0.2 M solution. Glycine was added as the chelating agent (the molar ratio of glycine to metal was 1.3:1). Polyvinyl pyrrolidone (PVP) was used (5 wt% relative to the amount of LSM) as a surfactant to improve the wetting of the solution onto the LSCF backbone.

Using a microliter syringe, 1 µL of the 0.2 M as-prepared LSM solution was infiltrated into a porous LSCF electrode, resulting in a weight loading of about 10 % of LSM. After allowing the solution to soak into the porous cathode and dry in air for 30 min, the infiltrated cells were fired at 900 °C for 1 h to obtain the desired phase of LSM. All of the chemicals were purchased from Alfa, USA. Pure LSM powders derived from the same solution were calcined at 900 °C for 1 h for phase identification. The as-prepared LSM powders together with commercial LSCF powders were selected as reference materials in the XAS study. In order to study the phase and structure stability of LSM-infiltrated LSCF cathodes (LSM-LSCF), some of the samples were annealed at 850 °C for 400 h in air.

4.1.2 X-ray absorption spectroscopy

4.1.2.1 Soft x-ray spectroscopy

Synchrotron-based X-ray absorption spectroscopy (XAS) was performed at the National Synchrotron Light Source at Brookhaven National Laboratory. For the soft x-ray experiment, near-edge XAS (XANES) was performed with bending magnet radiation at the U7A endstation using a 0.5 m toroidal spherical grating monochromator and a gold-coated ultra low expansion glass toroidal mirror to focus the beam to a spot size of about 1 mm by 0.5 mm. An electron detector with a −150 V grid bias collected Auger photoelectrons. Inside the load-lock chamber, the sample was heated in stages to 225 °C, 425 °C, and 750 °C via a resistive heating element behind the sample holder and held for 1 h at each temperature. Since the voltage of the power supply had to be controlled manually, the heating rate varied from 5 °C to 10 °C per minute, based off of visually observing a thermocouple reading and periodic recording of the time and temperature. The conditions were held until the outgassing slowed to the point where the baseline pressure of 5×10^{-7} Torr was recovered after which XANES data was collected. To protect the equipment and to minimize sample outgassing after holding at 750 °C for 1 h, the sample was cooled to room temperature before

being examined with XANES. A multi-element mesh was used as a reference sample to calibrate the energy. Since the XANES was based on partial Auger electron yield, the technique employed here is surface-sensitive.

4.1.2.2 Hard x-ray spectroscopy

For the hard x-ray experiments, XAS data were collected in either transmission or fluorescence mode using bending magnet radiation at the X23A2 endstation of the National Synchrotron Light Source. A Si (311) monochromator with a single bounce harmonic rejection mirror was used in a fixed exit Golovchenko-Cowan design and was stabilized using piezoelectric feedback. Mechanical beam slits were used to control the beam to a spot size of about 3.5 mm in width and 0.5 mm in height. When possible, the spectroscopy was performed *in situ* in transmission mode using a clamshell furnace mounted onto an *xyz*-translational stage with micron movement resolution. The samples were loaded into a six-slot stainless steel sample holder with individual alumina rings for mechanical support. The sample holder was inserted into a quartz tube, the ends of which extended outside the clamshell furnace and which were fitted with O-rings, stainless steel gas connections, an internal thermocouple, and Kapton windows. To achieve x-ray transmission, the length of the tube was aligned with the beam path. The furnace was heated to 750 °C at 7.5 °C per min and 2 h were allowed for equilibration. After each gas change at high temperature, 1 h was allowed for equilibration. A cross-sectional view of the samples in the furnace at temperature is shown in Figure 6 while a panoramic view of the experimental setup is shown in Figure 7.

For the Mn K-edge, because of its dilute concentration, the thermal treatments were performed *ex situ* and a four-element Vortex silicon drift fluorescence detector was employed *ex situ*. Metal foils, or metallic oxides when pure metals were unavailable, were used for reference and energy calibration in transmission experiments.

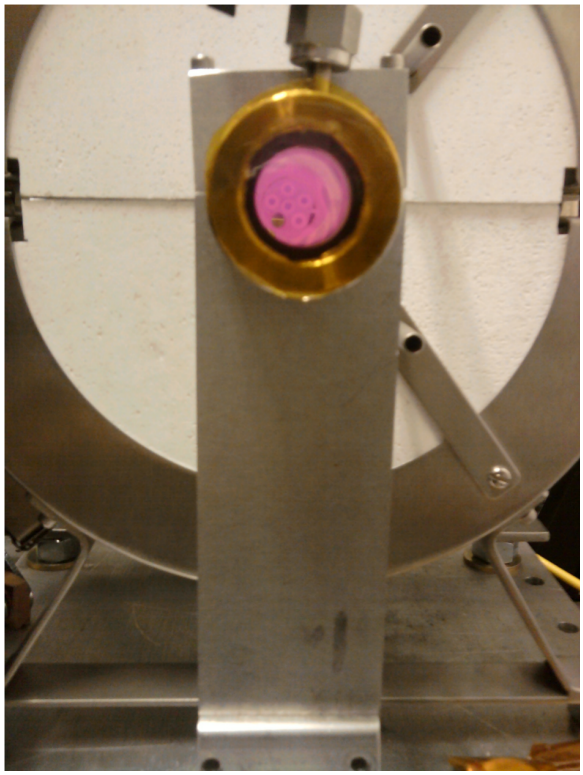

Figure 6: Cross-sectional view of the tube furnace showing the sample slot-holder for transmission XAS. The yellow covering is Kapton tape, which has low x-ray absorbance, to seal the tube gas environment.

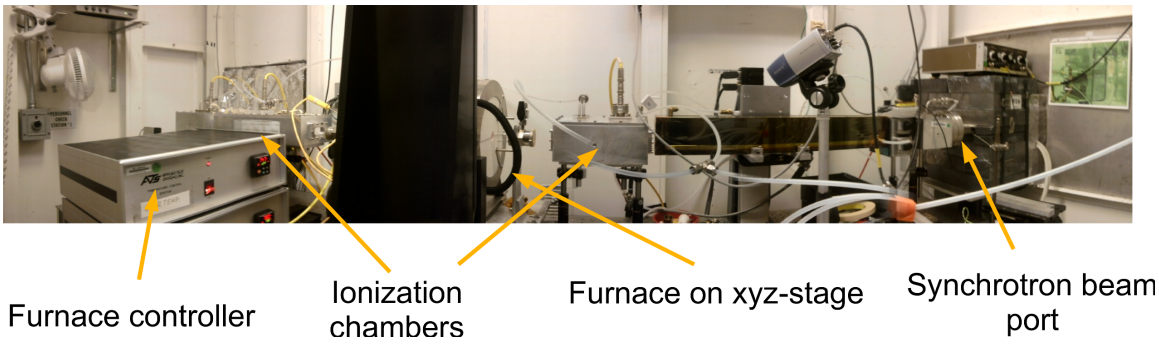

Figure 7: Panorama of the experimental setup for *in situ* transmission XAS showing the beam path and the equipment used. The furnace is somewhat hidden by the black z-axis control of the stage mount.

Table 2: Characterization modes for each sample in tabular form. Due to the low concentration of Mn cations, *ex situ* fluorescence was used with time averaging.

Sample	X-ray Energy	Characterization
as-prepared	Soft	*ex situ* partial electron yield
LSM	Hard	*ex situ* transmission XAS
as-prepared	Soft	*ex situ* partial electron yield
LSCF	Hard	*ex situ* transmission XAS
as-prepared	Soft	*ex situ* partial electron yield
LSM-LSCF	Hard	*in situ* transmission XAS
	Hard	*ex situ* fluorescence XAS (Mn only)
annealed	Soft	*ex situ* partial electron yield
LSM-LSCF	Hard	*in situ* transmission XAS
	Hard	*ex situ* fluorescence XAS (Mn only)

Reference data were unavailable in fluorescence experiments due to the configuration of the equipment. A complete description of the samples and the different soft and hard x-ray experiments are tabulated in Table 2. While transmission XAS is preferable to fluorescence XAS, due to the low concentration of Mn in the samples, *ex situ* fluorescence was used with time averaging.

4.1.2.3 Artemis FT EXAFS fitting

To further analyze the structure features and phenomena observed in the FT EXAFS of the Mn cation, the Artemis program from the Demeter software suite was used [60]. The $LaMnO_3$ parent cubic perovskite structure was used as the model unit cell [62]. The justification for using this simplified structure was to avoid developing a complex system of averaging the fitted results from multiple models needed to accurately represent the stoichiometry of LSM for the sake of answering a few simple questions. Using Mn as the core absorber atom, the built-in ATOMS program created an 8.0 Å cluster with a maximum path length of 5.0 Å. FEFF6 was used calculate the scattering path parameters. All of the single and multiple scattering paths up to the Mn-Mn scattering path were selected. Within this distance, multiple scattering paths

only involve oxygen atoms. Individual $S0^2$ variables were assigned to each path, $\delta\ R$ and σ^2 values were assigned by element, and one $\delta\ E_0$ value was used for all of the paths. Variables were individually refined procedurally, with all other variables kept constant.

4.1.2.4 CTM4XAS simulation

To further analyze the L-edge XANES of key transition metal cations, CTM4XAS 5.5 software was used to simulate the peak positions of the cations at different valence states [71]. For purposes of simplicity, a crystal symmetry of D_{4h} was assumed and the crystal field splitting energy (CFSE) was set between 0.0 eV to 2.0 eV in 0.5 eV increments. Gaussian and Lorentzian broadening factors were both set at 0.5. The spectra for each formal valence charge was manually modified in intensity to approximate the data.

4.2 Results and Discussion

4.2.1 Microstructure and crystal structure characterization

Scanning electron microscopy was performed using a LEO 1530 thermally-assisted field emission electron beam. Qualitatively speaking, the individual particles in Figures 8 and 9 are fairly homogeneous in morphology and variably distributed in size. The LSM thin film is unresolvable from the LSCF core particles. TEM results from related work indicates that the LSM thin film thickness varies from 2 nm to 20 nm and that the film is conformal to the LSCF core particle [45]. However, TEM is a selective sampling of the particles and does poorly to represent the properties of the population. Phase contrast can be ineffective in resolving substrates from infiltrated catalysts, particularly when catalysts are similar to the substrate in composition and morphology [29]. For catalyst infiltrations, the morphological result is predominantly particles, but thin films could be formed if sufficiently dense populations of particles are sintered together. X-ray diffraction indicated that the desired phases of LSM and

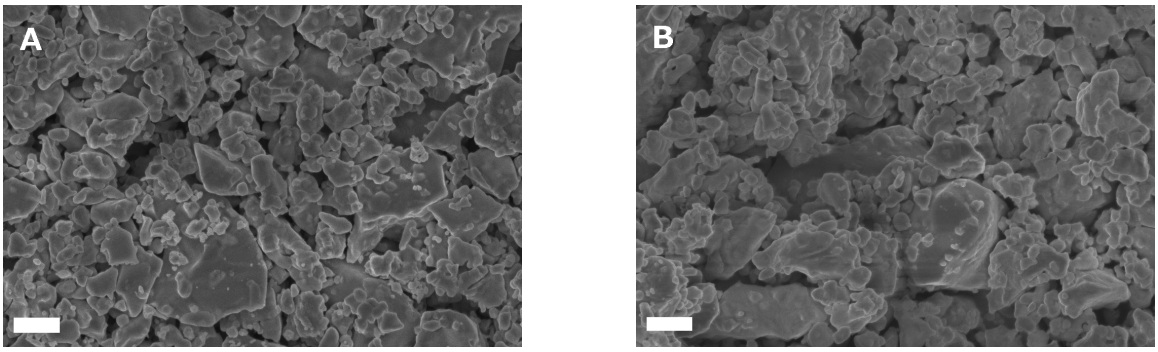

Figure 8: Scanning electron micrograph of (A) as-prepared LSM-infiltrated LSCF and (B) annealed LSM-infiltrated LSCF. Scale bars are 1 µm.

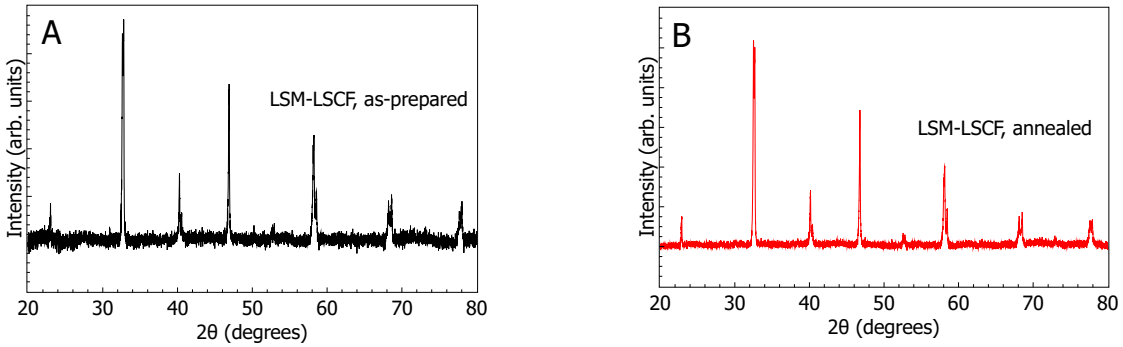

Figure 9: X-ray diffraction patterns of (A) as-prepared LSM-infiltrated LSCF and (B) annealed LSM-infiltrated LSCF.

LSCF were formed. XRD was performed using a PANalytical XPert PRO Alpha-1, which uses Cu K-alpha radiation.

4.2.2 Sr K-edge XANES and EXAFS

The study of Sr cation migration and segregation is an area of interest for FT EXAFS investigation, because the FT EXAFS provides information about the local structure. It is important to note that the Sr cations in LSM and LSCF cannot be distinguished from each other in transmission XAS and the fluorescence XAS does not have the surface-specific resolution to probe solely the LSM thin film. Although the LSM thin film coating contains Sr in a different local structure, the LSM is dilute in concentration, so the Sr signal is predominantly representative of the LSCF backbone. The LSCF is the material of interest to probe what kind of effect the LSM thin film has

on the LSCF chemically or structurally.

As shown in Figure 10, there are several peaks of interest in the spectra for as-prepared LSCF, annealed LSCF, and annealed LSM-LSCF. The first two peaks around 1.6 Å and 2.1 Å are proportional to the radial distance between the Sr cation and the first two coordination shells. Since a phase shift correction factor was not applied in this study, the values in the FT EXAFS are proportional to the radial distances and not equal to the true bond lengths. From the tetragonal perovskite structure of LSCF, it can be inferred that the first two peaks correspond to the local coordination of oxygen at two slightly different lengths. The large peak at 2.8 Å corresponds to the next coordination shell to Sr, which is the B-site atom where Fe and Co reside in LSCF. While the remaining peaks in the range of 3.5 Å to 4.5 Å and beyond can be roughly associated with the coordination to a additional shells of A-site and O atoms, generally, the interpretation becomes more difficult and less clear at those radial distances because of the existence of multiple scattering paths.

From Figure 10, the spectrum of the annealed LSCF has a few distinct features. The peaks at 2.8 Å and 3.6 Å all shift slightly towards shorter distances while peaks at 2.0 Å and 4.0 Å shift slight towards longer distances. Thus, the local structure around Sr seems to be deforming as a result from the annealing, but maintaining the same overall shape. Additionally, some peaks are more easily resolved in the first and third groups of peaks centered at 1.8 Å and 4.0 Å, partly due to peaks splitting apart from each other. Lastly, the decrease in the intensity of the first two peaks suggest that the quantity of oxygen nearest neighbors decreased. The loss of oxygen around Sr may be evidence of degradation of the LSCF structure, which has been proposed to be caused by Sr enrichment [70, 37, 74]. The bulk-sensitive XAS and beamline used in this experiment, however, would not have the spatial resolution necessary to specifically examine localized regions of Sr enrichment, as Choi and co-workers observed with TEM EDS [11]. Thus, the FT EXAFS of annealed LSCF is too similar

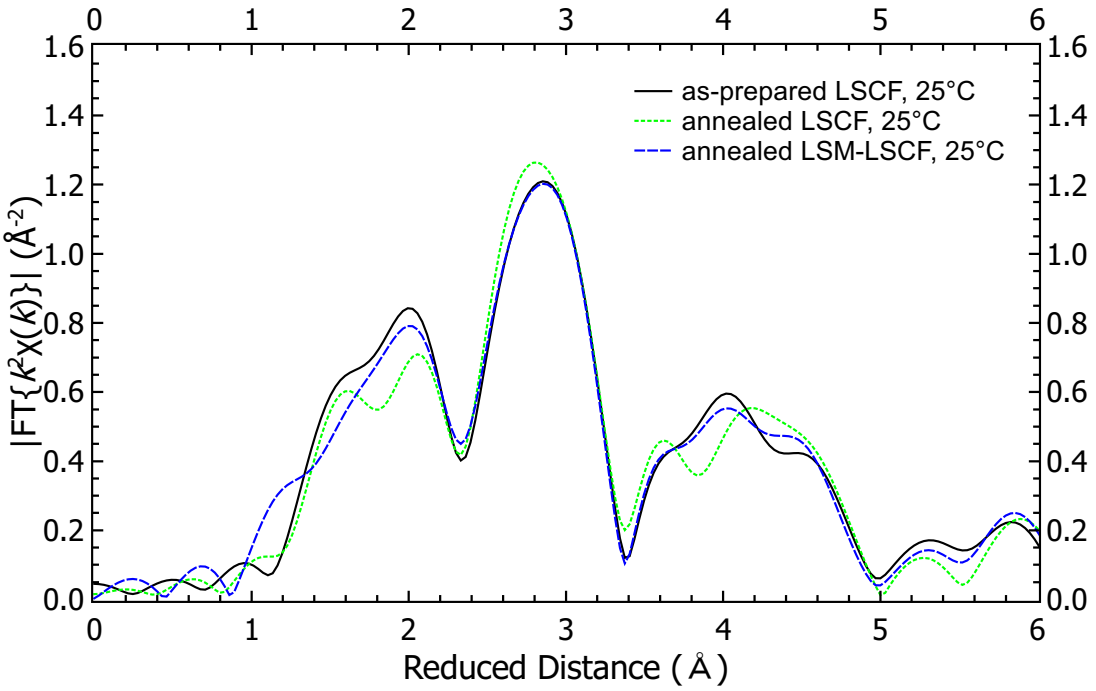

Figure 10: The Sr K-edge Fourier-transformed (FT) EXAFS of as-prepared LSCF, annealed LSCF, and annealed LSM-infiltrated LSCF at ambient temperature and pressure.

to that of LSCF to suggest that the majority of the Sr was in a segregated phase. The distinctions observed appear to be related to atoms adjusting to slightly different equilibrium positions and perhaps bond stretching and contraction.

In contrast, the FT EXAFS of the annealed LSM-LSCF closely matches that of the as-prepared LSCF, which implies that the Sr local structure in annealed LSM-LSCF is stable after long-term annealing. The solution-infiltrated coating of LSM appears to have stabilized the Sr in the LSCF against even small changes in local structure. The coinciding position of the troughs at 2.4 Å, 3.4 Å, and 5.0 Å are indicators that the majority of the Sr have a well preserved local structure.

4.2.3 Co L-edge XANES

From Figure 11, the soft X-ray XANES indicate that the Co cations in both as-prepared LSM-LSCF and annealed LSM-LSCF are reduced at 750 °C under ultra

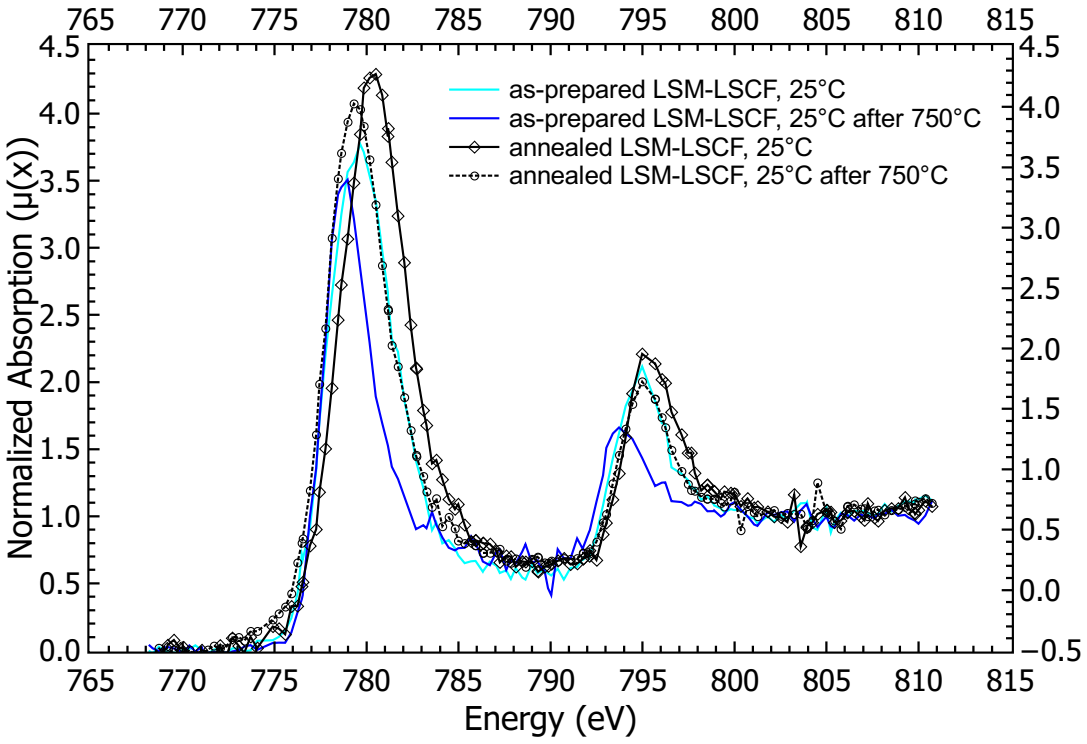

Figure 11: The Co L-edge XANES of as-prepared and annealed LSM-LSCF measured before and after thermal treatments of 750 °C.

high vacuum. Ultra high vacuum is a sufficiently low in oxygen partial pressure to generate oxygen vacancies [47], so the detection of Co using partial electron yield suggests that the LSCF backbone is partially exposed because the LSM solution infiltrated thin film coating is not conformal, and as a result, the reduction in the Co oxidation state is caused by the free electrons created with the oxygen vacancies.

4.2.4 Co K-edge XANES and EXAFS

In the Co K-edge XANES of as-prepared LSM-LSCF, shown in Figure 12, there does not appear to be a significant edge shift after the *in situ* heat treatment. However, the white line intensity increases and decreases after heat treatment with nitrogen and oxygen, respectively. Since a change in the white line intensity reflects a change in the density of unoccupied states, the heat treatment in nitrogen appears to have caused an increase in the density of unoccupied states. Some factors may possibly

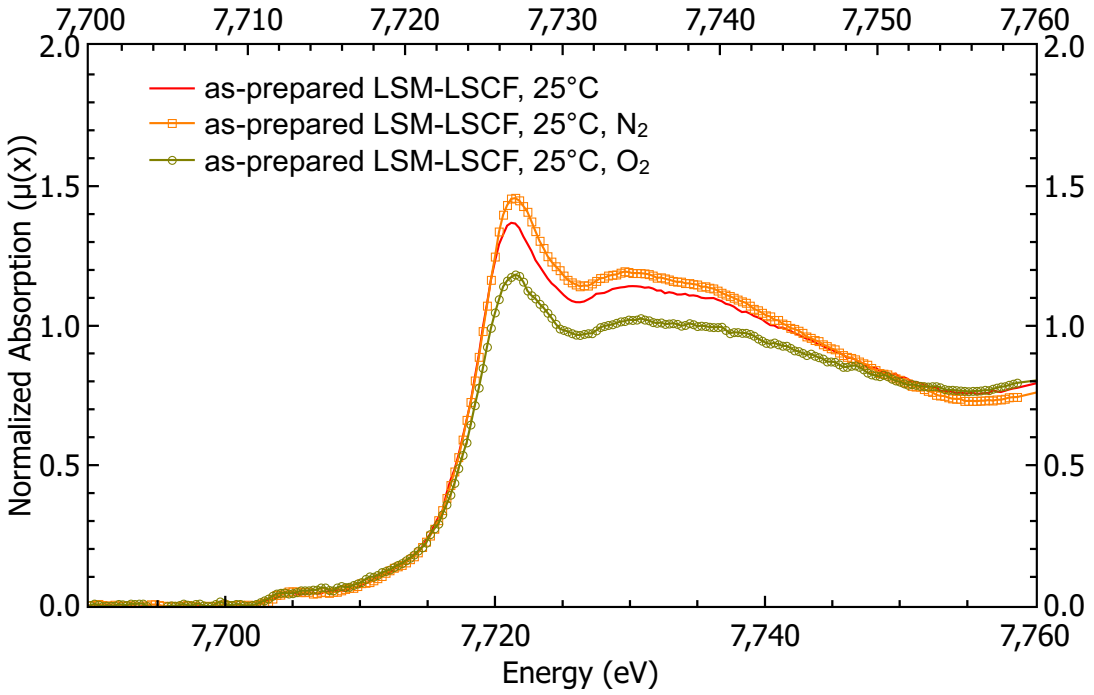

Figure 12: The Co K-edge XANES of as-prepared LSM-LSCF measured before and after thermal treatments of 750 °C under oxygen and nitrogen.

explain why the Co edge shift does not appear in the hard X-ray experiment but does appear in the soft X-ray experiment. First, the soft X-ray spectroscopy is measuring the L-edge p-d electron transition, whereas the hard X-ray spectroscopy measures the K-edge s-p electron transition. Second, the partial pressure of oxygen in ultra high vacuum is several more orders of magnitude lower than ambient oxygen partial pressure compared to pure nitrogen or oxygen. Third, the Mn cation is observed to reduce significantly during the heat treatment, as discussed later, which may indicate preferential charge compensation over the reduction of Co. Additionally, the spectra were measured *ex situ* but the samples were quenched in their respective atmosphere and sealed in Kapton during measurement. It is unlikely but it could possibly contribute to the lack of edge shift.

When the Co K-edge XANES of the annealed LSM-LSCF is examined at high temperature under reducing conditions, the edge energy decreases, as shown in Figure 13, indicating a lower oxidation state. However, the Co oxidation state increases

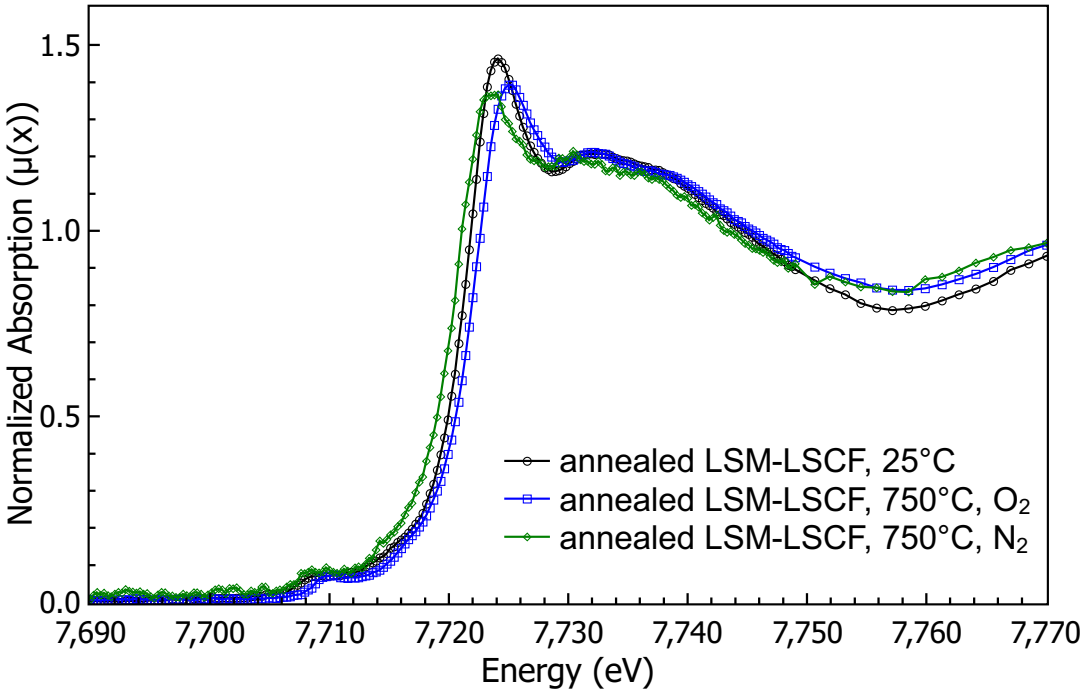

Figure 13: The Co K-edge XANES of annealed LSM-infiltrated LSCF measured *in situ* at 750 °C under oxygen and nitrogen.

when the atmosphere is switched to oxygen, which is evidence that the Co oxidation state compensates for excess charge from changes in oxygen stoichiometry. In contrast to the previous observations in soft x-ray XANES and in hard x-ray XANES of as-prepared LSM-LSCF where the Co oxidation state was unaffected, the annealing caused some modification of oxidation states and local structure so that the Co is compensating for changes in oxygen stoichiometry. The nature of this modification is made clearer later when taken in context with the Mn XANES and FT EXAFS data.

The FT EXAFS of the Co K-edge shown in Figure 14 indicates the first two coordination shells at 1.2 Å and 1.6 Å shortened and lengthened, respectively, in annealed LSCF in comparison to as-prepared LSCF. In as-prepared LSCF, the first two coordination lengths are located at 1.2 Å and 1.6 Å. Annealing the LSCF causes the two coordination lengths to stretch to 1.3 Å and 1.8 Å, respectively. The intensity of both peaks also increased. The significant increase in the first peak suggests that the neighboring oxygens bonded to the Co cation increased in their regularity. The

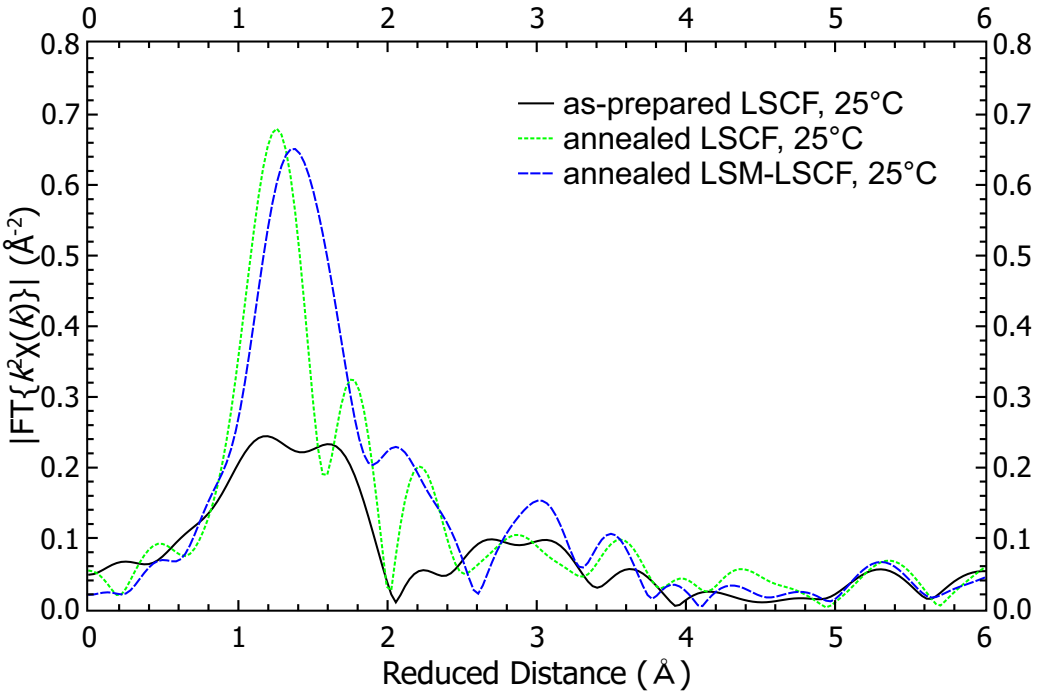

Figure 14: The Co K-edge FT EXAFS of as-prepared LSCF, annealed LSCF, and annealed LSM-LSCF measured at ambient temperature and pressure.

divergence of the two coordination lengths in combination with the change intensity suggest that the local atomistic environment of the Co in LSCF is affected by long-term annealing. A Co-containing oxide, such as Co_3O_4, has been suspected of segregating out of LSCF after long-term operation [42] and would have a different local atomistic structure, particularly for the first coordination length with oxygen. Although the FT EXAFS of as-prepared and annealed LSCF are too similar unambiguously determine the presence of a segregated phase, it is clear that the annealing has caused a rearrangement in the Co local structure.

The local structure of Co in annealed LSM-LSCF is unlike that of as-prepared LSCF or annealed LSCF, as shown in Figure 15. The two coordination lengths previously observed in as-prepared LSCF appear to become convoluted into a single coordination length of 1.4 Å. Similar to the FT EXAFS of annealed LSCF, the intensity of the first peak increased, suggesting that annealing causes local ordering of the first coordination shell. However, the various new peak positions observed at

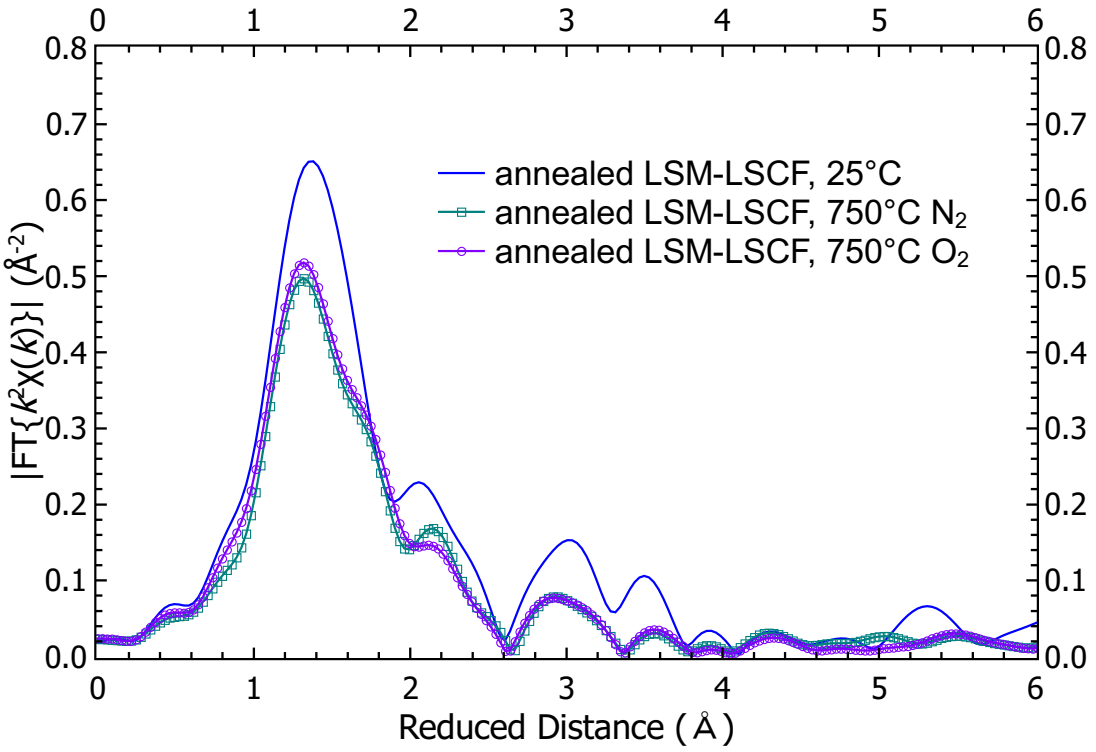

Figure 15: The Co K-edge FT EXAFS of annealed LSM-LSCF measured *in situ* at 750 °C under oxygen and nitrogen.

1.4 Å, 2.1 Å, and 3.0 Å suggest that the Co local structure in annealed LSM-LSCF is not the same as that of annealed LSCF. The slight changes observed may result from the Co diffusing into the LSM thin film, as observed by TEM and EDS [45], and achieving a similar but distinct local structure.

When the FT EXAFS of annealed LSM-LSCF is obtained *in situ* under oxidizing and reducing conditions, as shown in Figure 15, there is no significant change in the local structure. The first coordination length appears to shorten by 0.05 Å. The second coordination length expands slightly into a peak shoulder, which indicates that the first coordination length at 1.4 Å is a convolution of two peaks. The shortening of the first coordination length was also observed in the Sr FT EXAFS of annealed LSM-LSCF. The significance of the larger Debye-Waller factor at high temperatures is apparent, dampening the intensity and broadening the peaks, which make interpretation less trustworthy. However, there are no significant differences between reducing

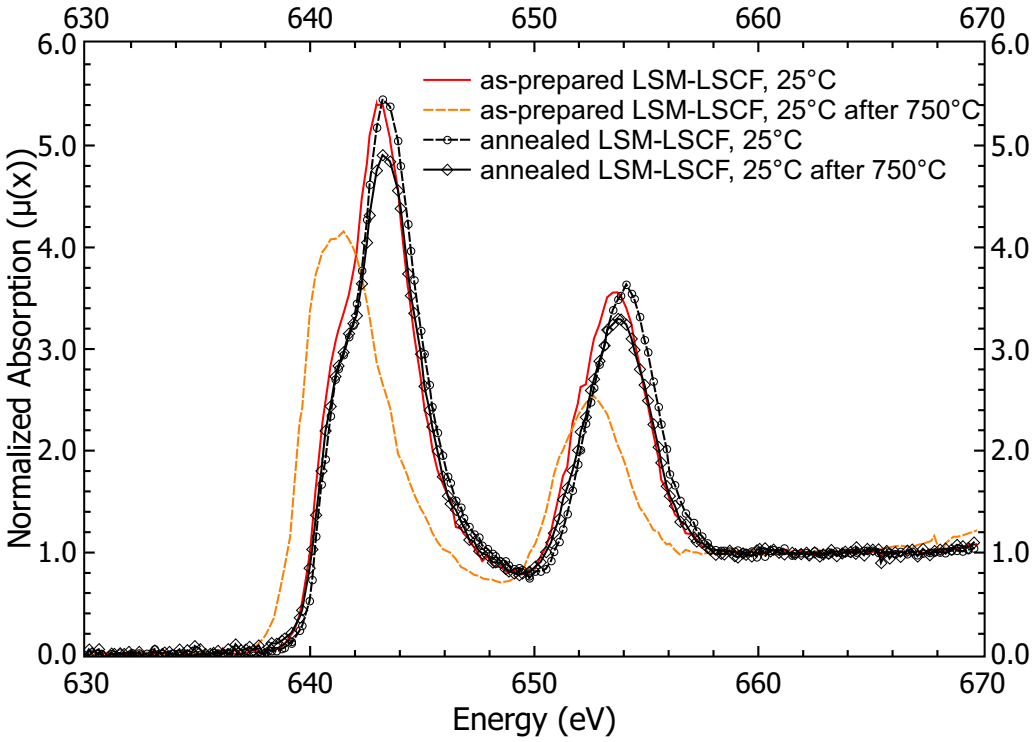

Figure 16: The Mn L-edge XANES of as-prepared and annealed LSM-LSCF measured before and after thermal treatments of 750 °C.

and oxidizing conditions and the rest of the structure is similar after accounting for the Debye-Waller factor.

4.2.5 Mn L-edge XANES

In Figure 16, the soft X-ray XANES showed a shift in the Mn L-edge of 1.0 eV between the as-prepared LSM-LSCF and the LSM-LSCF heated *in situ* at 750 °C. The shift in the Mn L-edge energy indicates that the Mn cation, as seen from the Mn L-edge (p-to-d transition), is reduced after a thermal treatment of 750 °C under UHV. However, in annealed LSM-LSCF, the spectra do not shift, indicating that the Mn cation's oxidation state was not affected by the thermal treatment of 750 °C. Thus, the Mn cation undergoes an oxidation state change from the thermal treatment. It is believed that the Mn cation undergoes a reaction with the underlying LSCF which causes this thermally-activated shift in oxidation state.

Using CTM4XAS v5.5, the L-edge XANES of Mn of various formal valence states were simulated and manually refined to roughly approximate the experimental data. Although quantitative results could not be obtained without custom programming scripts to further refine the fit, the relative ratios of each Mn formal valence state can be determined qualitatively. Additionally, some insight about the low or high spin states of the Mn cation can be gained by adjusting the crystal field splitting energy (CFSE) parameter of the fit. As mentioned earlier, the as-prepared LSM-LSCF Mn L-edge spectrum shows a significant peak shift after the thermal treatment. Based on Figure 17, a CTM4XAS simulation fit contained two Mn^{3+} valence states, one weak and one strong field, accompanied by a Mn^{2+} species with a weak field. Here, "weak" and "strong" fields reference small and large crystal field splitting energies, assuming octahedral coordination with oxygen. A weak CFSE parameter implies that electrons will occupy the higher energy e_g orbitals and remain unpaired, usually resulting in a high spin state for Mn, depending on the valence state. A strong CFSE parameter, conversely, implies that the electron pairing energy barrier is lower than the CFSE, resulting in low spin states of Mn. Through the fitting process, it became evident that both weak and strong (high and low spin, respectively) field Mn^{3+} spectra were needed to approximate the experimental data. For clarity, the Mn^{4+} weak field spectrum, which was the best fitting Mn^{4+} calculated spectrum, was also plotted to show the poorness of its fit. It was noted from the simulation that the trend of higher CFSE values was the main peak shifting to higher energy while a much smaller peak at lower energy formed and grew.

The CTM4XAS simulation fit for the annealed LSM-LSCF, shown in Figure 18, similarly consisted of the weak and strong field Mn^{3+} valence states. The summation of the two Mn^{3+} simulated spectra contains the majority of the experimental data but insufficiently captures the shoulder feature at 641 eV and overcompensates at 639 eV. However, it is clear that adding a weak field Mn^{2+} spectrum to the fit would not

adequately fit the shoulder. It is speculated that the shoulder may require simulated spectra with a finer resolution of the CFSE parameter to fit. It should be noted that the weak field Mn^{3+} would have a high spin state and asymmetrically filled e_g orbitals, implying active Jahn-Teller distortion of the octahedral coordination, which was not accounted for in the simulation. As was done for the as-prepared LSM-LSCF spectra, the weak field Mn^{4+} spectrum is also plotted in cross-hatch to show that it would not fit well.

Initially, it can be concluded that the thermal treatment in UHV caused lattice oxygen to depart the as-prepared LSM-LSCF material, leaving behind oxygen vacancies and corresponding free electrons. These electrons reduced the Mn cation in as-prepared LSM-LSCF, which explains the presence of the Mn^{2+} weak field/high spin species found by CTM4XAS. The as-prepared LSM-LSCF showed higher ratio of Mn^{3+} weak field/high spin to Mn^{3+} strong field/low spin than the annealed LSM-LSCF, which showed a nearly even ratio of the two Mn^{3+} species. Assuming that the low spin Mn^{3+} species has more stable bonds with oxygen because it has fewer electrons in the e_g anti-bonding orbitals, the change in the relative ratio of Mn^{3+} species suggests increased stability of the Mn local crystal field, hence explaining why the Mn is not active in charge compensation of oxygen vacancy generation. Thus, the spectra of annealed LSM-LSCF closely match those of as-prepared LSM-LSCF before the thermal treatment in UHV while the Co cation continues to compensate charge imbalance. This phenomenon is consistent with both the Co and Mn hard x-ray spectra, the latter of which is discussed later, and is evidence that the benefits of LSM as a thin film surface modification originate from structural causes and may not be as related to enhanced catalysis of the oxygen reduction reaction at the surface as initially suspected.

Although the models have some of deficiency in fitting the intensity, only a modest energy scale adjustment of 0.5 eV was made to the simulated spectra, so the positions

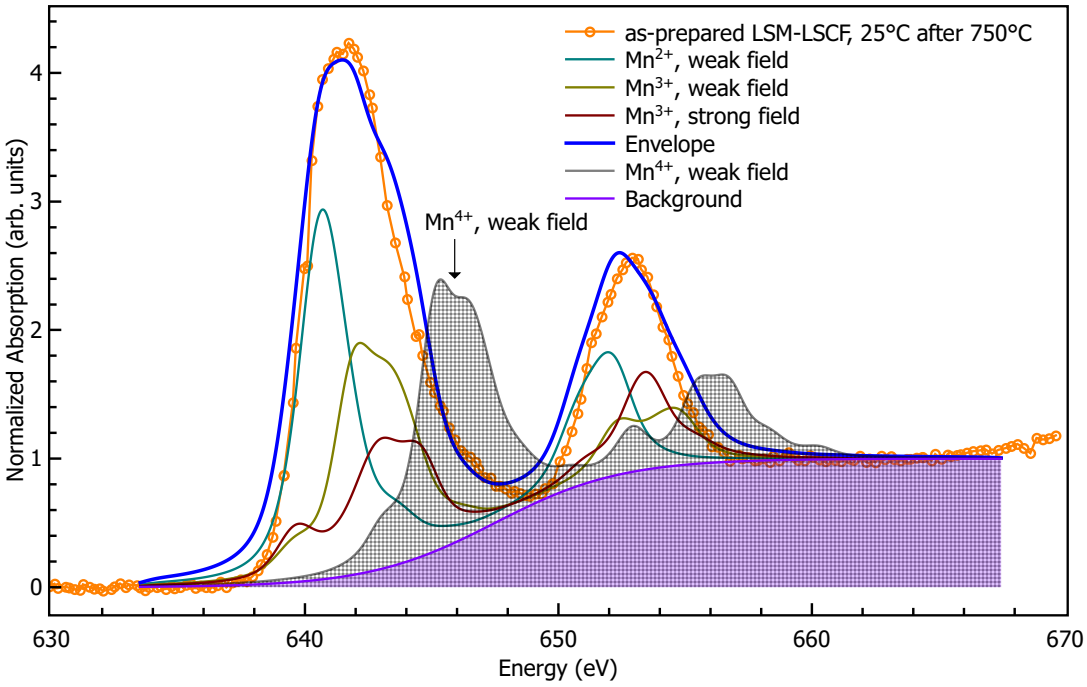

Figure 17: The CTM4XAS simulations fitting of the Mn L-edge XANES of as-prepared LSM-LSCF measured after heating to 750 °C and cooling to room temperature.

of the valence states in the experimental spectra are relatively close to the theoretical values. The intensity mismatch in the L_2 peak could potentially be fixed by using more nuanced parameters (D_t, D_s) in the CTM4XAS calculation. Reducing the Gaussian and Lorentzian broadening factors did not aid the fitting of sharper peaks.

4.2.6 Mn K-edge XANES and EXAFS

In the hard x-ray *ex situ* fluorescence Mn K-edge experiment, several unique behaviors of the Mn cation are observed. Figure 19 shows that the Mn cations in as-prepared LSM, as-prepared LSM-LSCF, and annealed LSM-LSCF at 25 °C are in different electronic states, respectively. From this, it can be concluded that both the presence of underlying LSCF and thermal treatment both have an effect on the Mn oxidation state. In Figure 20, the Mn in as-prepared LSM-LSCF is reduced after heat treatment of 750 °C under nitrogen. When the same heat treatment occurs under an oxygen

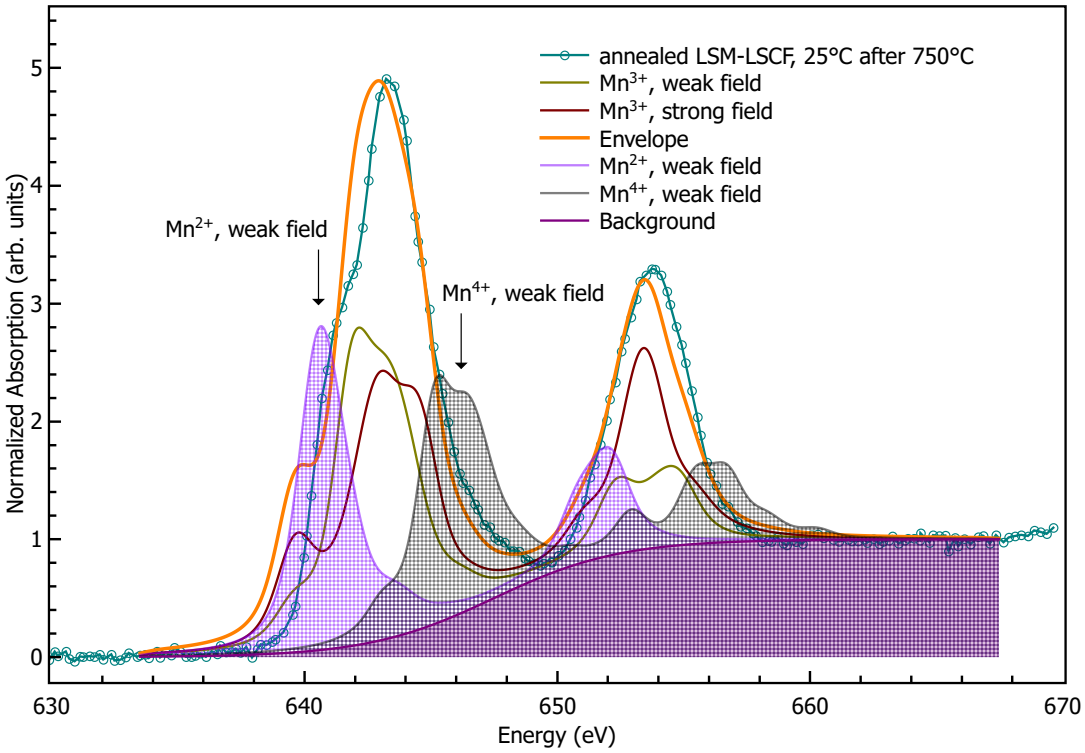

Figure 18: The CTM4XAS simulations fitting of the Mn L-edge XANES of annealed LSM-LSCF measured after heating to 750 °C and cooling to room temperature.

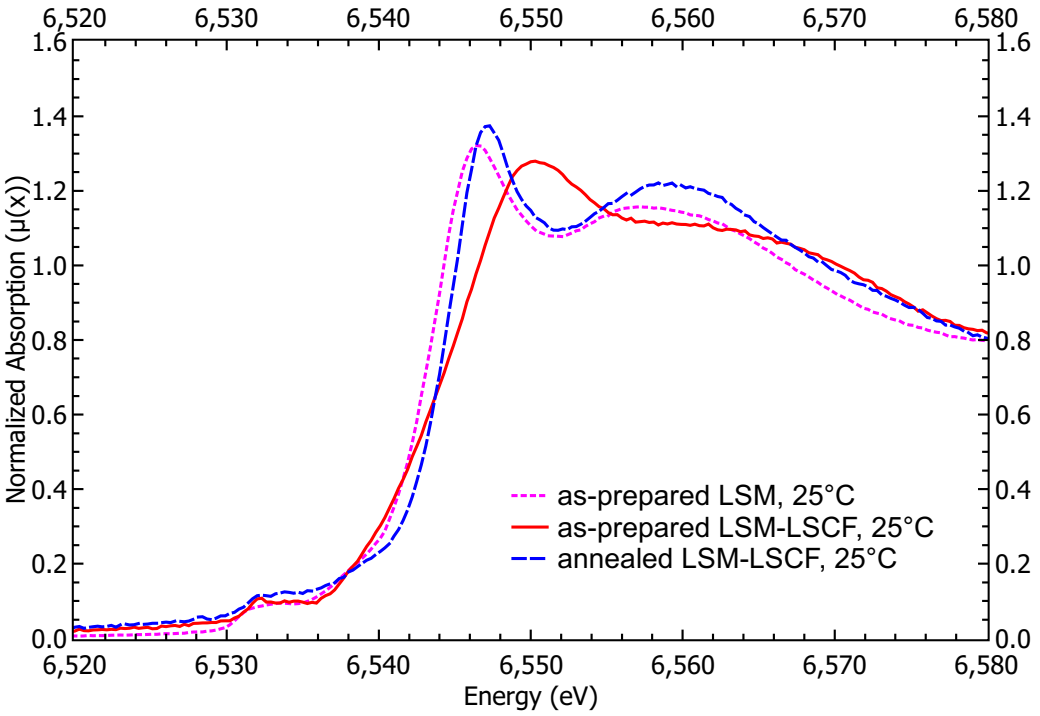

Figure 19: The Mn K-edge XANES of as-prepared LSM, as-prepared LSM-LSCF, and annealed LSM-LSCF measured at ambient temperature and pressure.

atmosphere, the Mn cation is further reduced. Thus, it seems that reduction of Mn oxidation state is a function of the thermal treatment and independent of an oxidizing or reducing environment.

In the annealed LSM-LSCF, the Mn cation oxidation state is unaffected by heat treatments under nitrogen or oxygen, as seen in Figure 21. Thus, both the Mn K-edge and L-edge XANES data both indicate that the Mn cation is reduced in as-prepared LSM-LSCF but is unaffected in annealed LSM-LSCF. With no change in the Mn valence state, it is concluded that the Mn no longer provides charge compensation for oxygen incorporation in annealed LSM-LSCF.

More insight regarding the local atomistic environment of the Mn cation can be derived from the FT EXAFS. From the FT EXAFS of the Mn K-edge, the local atomistic structures of Mn in as-prepared LSM-LSCF and annealed LSM-LSCF are shown in Figure 22. The FT EXAFS of as-prepared LSM is included for reference.

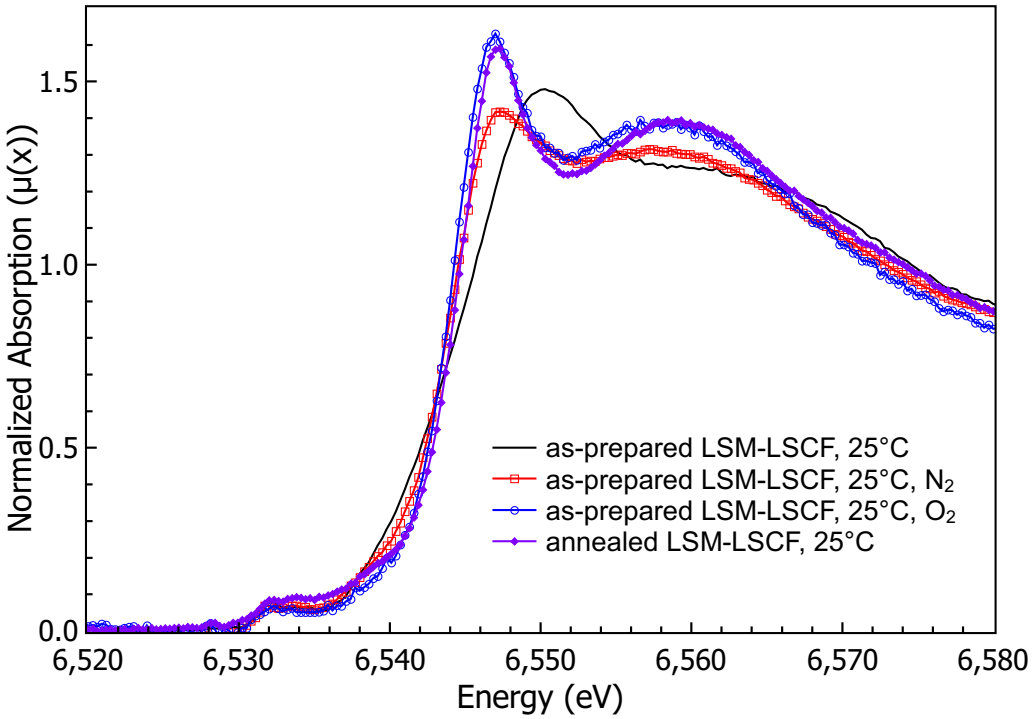

Figure 20: The Mn K-edge XANES of as-prepared LSM-LSCF measured *ex situ* before and after thermal treatments of 750 °C in oxygen and nitrogen.

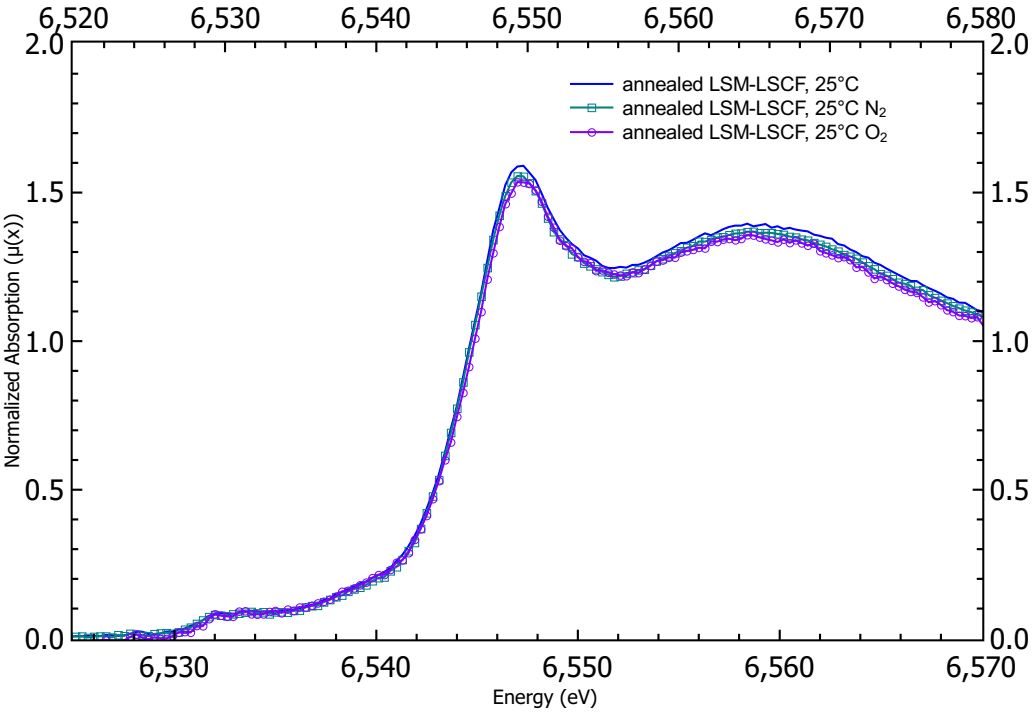

Figure 21: The Mn K-edge XANES of annealed LSM-LSCF measured *ex situ* before and after thermal treatments of 750 °C under oxygen and nitrogen.

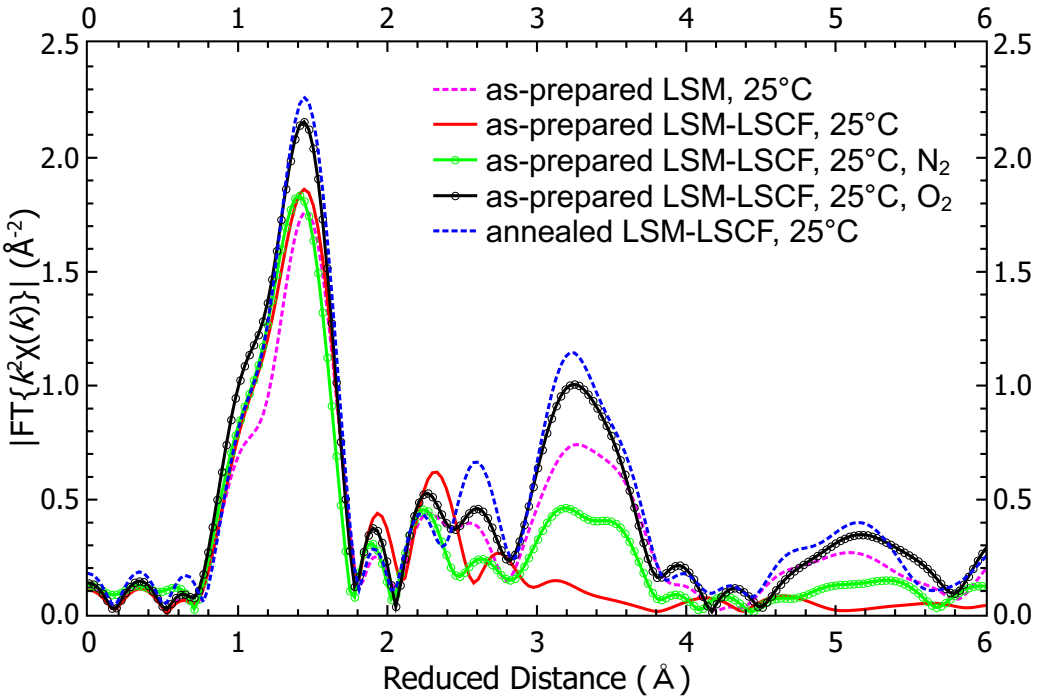

Figure 22: The Mn K-edge FT EXAFS of as-prepared LSM-LSCF measured *ex situ* before and after thermal treatments of 750 °C under oxygen and nitrogen.

The first peak at 1.4 Å is assigned to the first oxygen coordination shell, which is assumed to be octahedral.

In the as-prepared LSM-LSCF, there are two particular patterns to note. Firstly, two peaks appear at 3.2 Å and 3.5 Å when the as-prepared LSM-LSCF is heated at 750 °C in nitrogen for 1 h. These peaks are more intense after the heat treatment is subsequently repeated in oxygen. Second, when the as-prepared LSM-LSCF is heat treated under nitrogen, there is little change in the nearest oxygen coordination shell except a slight shortening and small decrease in intensity. In contrast, when the as-prepared LSM-LSCF is heat treated under oxygen, there is an increase in the peak intensity for both the nearest oxygen coordination and the two peaks at 3.2 Å and 3.5 Å. Incorporation of oxygen from the atmosphere may explain the increase in the oxygen coordination around the Mn cation. The other emerging peaks were later analyzed using Artemis EXAFS modeling.

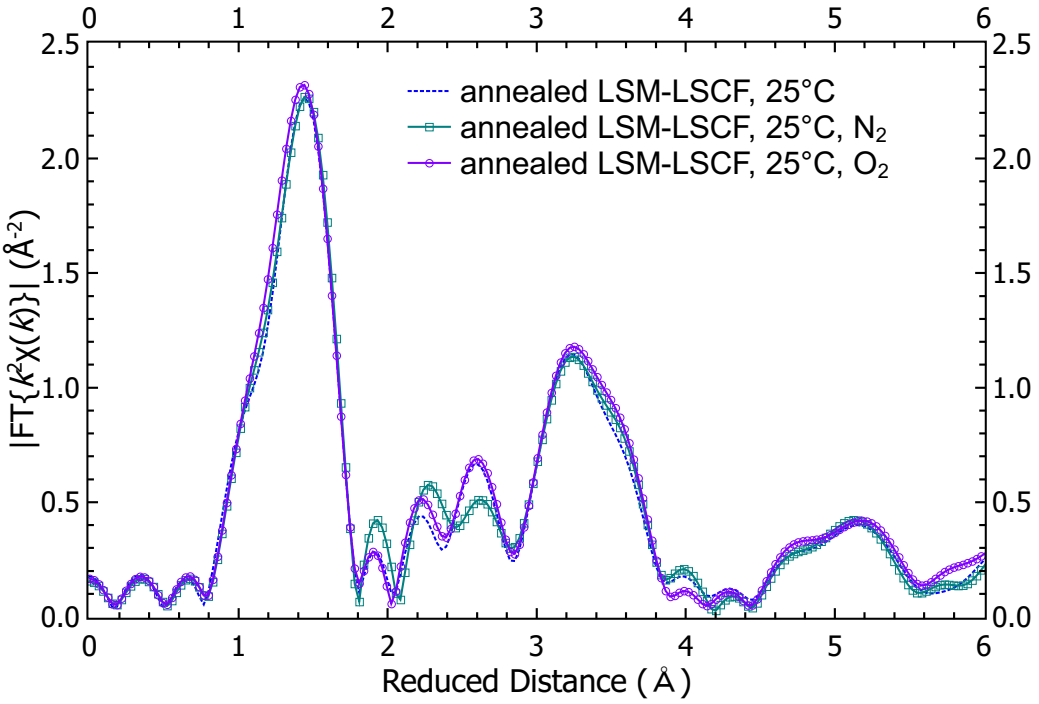

Figure 23: The Mn K-edge FT EXAFS of annealed LSM-LSCF measured *ex situ* before and after thermal treatments of 750 °C under oxygen and nitrogen.

In the annealed LSM-LSCF, there are no remarkable differences in the FT EXAFS in Figure 23 caused by the heat treatments under oxygen and nitrogen. The oxygen coordination and metal cation coordination around the Mn cation increased slightly, which suggest that a slight amount of oxygen incorporation is likely occurring. The FT EXAFS from the hard X-ray *ex situ* fluorescence spectroscopy shows that the reordering reaction has proceeded to completion after annealing and that annealed LSM-LSCF is relatively stable in comparison to the as-prepared LSM-LSCF, as would be expected.

To investigate the spectroscopic trends in Figure 22, Artemis EXAFS modeling software was used. At a rudimentary level, the Artemis analysis results could be used to gain insight on some of the possible mechanisms that would explain the transformation of the local structure observed in the Mn EXAFS, particularly between 2 Å and 4 Å.

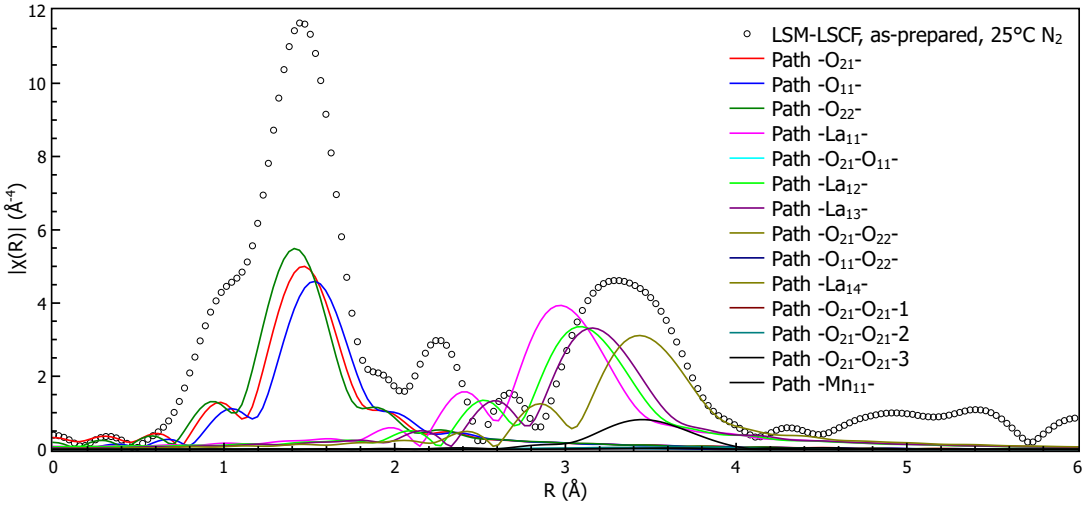

Figure 24: Each single- and multi-scattering path contributes to the overall EXAFS single at different distances. Single-scattering paths contribute significantly more than multi-scattering paths.

Individual paths with respect to the overall calculated fit are shown in Figure 24. The first major peak feature at 1.5 Å is representative of the oxygen in the first nearest neighbors shell and the peak magnitude grows with increasing exposure to oxygen-containing atmosphere, whether by a pure oxygen environment or by a long-term anneal in air at high temperature. It can be reasoned that changes in the proportional intensity of different scattering paths of the oxygen nearest neighbors could explain the shift in the shoulder at 1.0 Å. Additionally, the scattering paths have some effect on the peaks between 2.0 Å and 2.5 Å.

The positions of the individual scattering path spectra make clear that both La and Mn scattering paths in the model cluster contribute to the ordering phenomenon observed between 3 Å and 4 Å. Trends in select fit parameters are plotted in Figure 25. The amplitude values for the La paths tend to increase as the ordering increases. When significant peak structure was present to fit, the amplitude values of Mn tended to reach the constraint limit of 1. When there was a lack of peak structure to fit, the amplitude values had very large error uncertainty so the values were set to 0 but the fit still appeared to agree with the data. It should be noted that the model is based

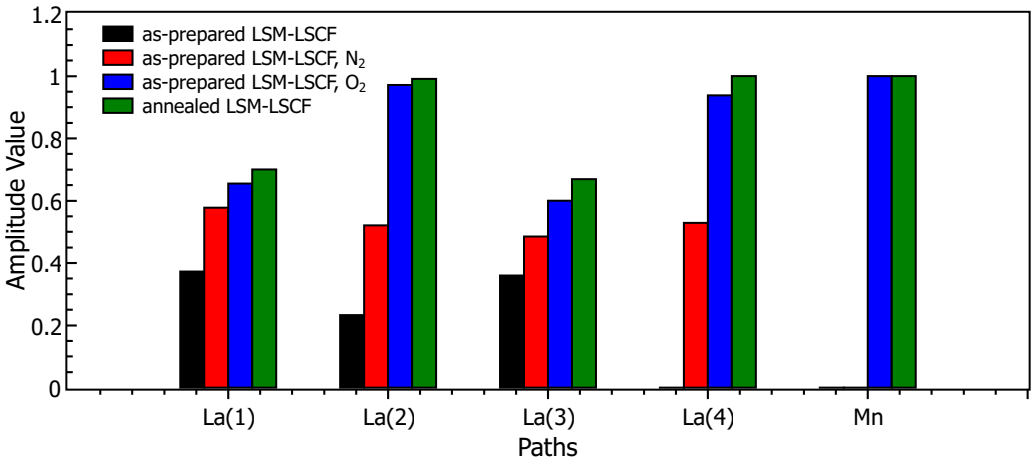

Figure 25: Amplitude values for La and Mn scattering paths for EXAFS fits of as-prepared LSM-LSCF in air and after treatments in nitrogen and oxygen and annealed LSM-LSCF.

on $LaMnO_3$, but since the experimental data reflect a doped LSM-LSCF sample, the ordering should be generalized to occur at both the A-sites and B-sites relative to the Mn cation.

Another subtle trend is observed for the two smaller peaks in the region between 2 Å and 3 Å, which appear to be inversely related in magnitude with increasing thermal treatment under oxygen. When comparing the extreme cases of as-prepared LSM-LSCF and annealed LSM-LSCF in Figure 26, the peak at 2.33 Å decreases in magnitude while the peak at 2.73 Å increases in magnitude, while contracting to 2.20 Å and 2.60 Å, respectively, in the annealed LSM-LSCF spectrum. The Mn FT EXAFS of as-prepared LSM-LSCF after treatment in nitrogen and oxygen show consistent, intermediate steps of the changes in peak magnitude (see Figures 61 and 62). Based on the paths in the region between 2.0 Å to 3.0 Å, the main contributions come from secondary peaks of the La paths, which partly explains why the underfitting in as-prepared LSM-LSCF, which lacks the main structure of the La paths between 3.0 Å to 4.0 Å. However, multiple scattering oxygen paths can be excluded as being too lengthy for this region. Thus, it is difficult to speculate the physical meaning of this trend.

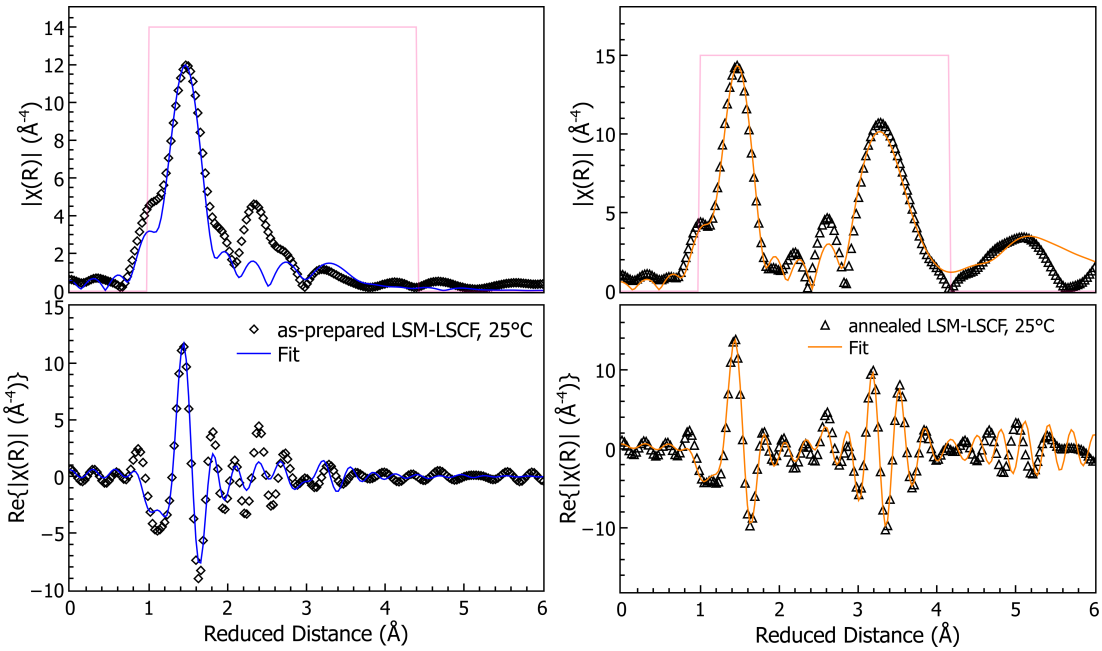

Figure 26: Artemis fitting results of the Mn local structure in (a) as-prepared LSM-LSCF and (b) annealed LSM-LSCF.

The combination of the phenomena observed in soft X-ray XANES, hard X-ray XANES, and hard X-ray FT EXAFS of Mn suggest that the Mn cation in as-prepared LSM-LSCF is in a non-equilibrium state but reaches an equilibrium valence state and local crystal field after heat treatment at high temperature. The appearance and growth of the hard X-ray FT EXAFS peaks suggest that the A-site cations and Mn in the LSM becomes more ordered. The ordering phenomenon may occur due to local heterogeneities in the cation concentrations of the LSM solution during infiltration and drying, leading to a non-equilibrium stoichiometry when synthesized. Additionally, reaction with the underlying LSCF substrate and interdiffusion of cations, as observed by Lynch *et al.* [45] may cause the local structure of Mn cations to become more ordered as a function of annealing time and temperature. The oxygen-rich atmosphere also appears to have assisted in the ordering phenomenon, because the intensity of the FT EXAFS peak growth is greater when the as-prepared LSM-LSCF is heat treated under oxygen compared to peak growth observed after heat treating

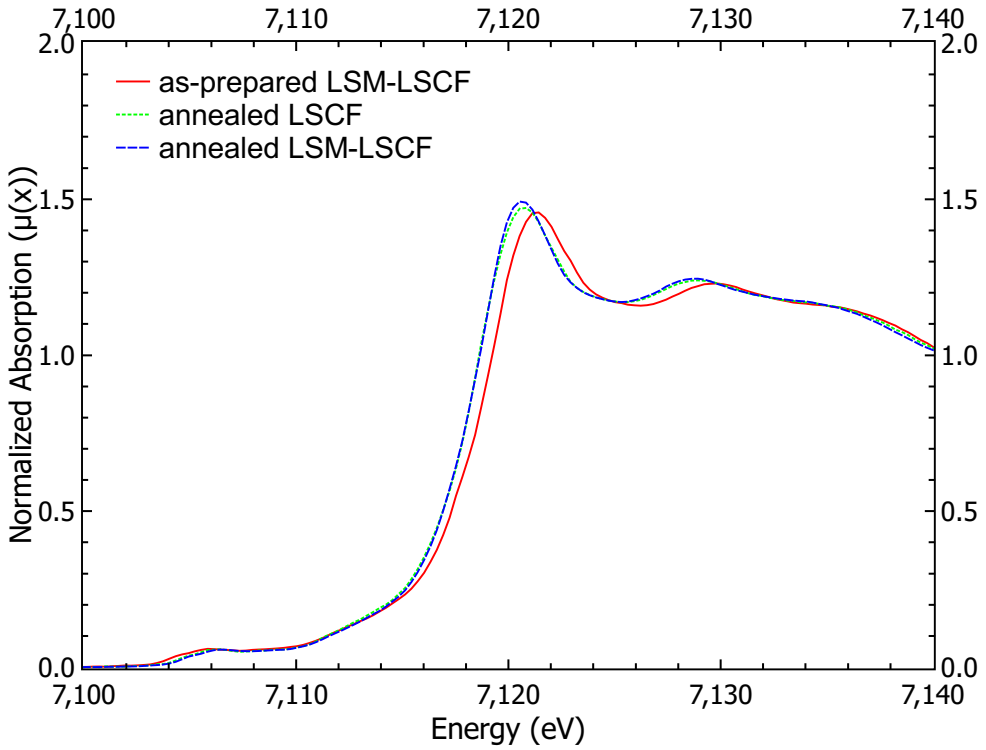

Figure 27: The Fe K-edge XANES of annealed LSCF, as-prepared LSM-LSCF, and annealed LSM-LSCF measured at ambient temperature and pressure.

under nitrogen.

4.2.7 Fe K-edge XANES and EXAFS

The Fe K-edge XANES in Figure 27 show a slight reduction in the Fe cation in annealed LSCF and in annealed LSM-LSCF, in contrast to as-prepared LSM-LSCF. No significant change was expected in the Fe oxidation state or local structure of LSCF but the slight reduction of the Fe cation is similar to the Mn cation reduction observed after annealing and thus, is suspected to be related to the reordering reaction.

The comparison of the Fe cation FT EXAFS between as-prepared LSM-LSCF and annealed LSM-LSCF in Figure 28 reveals similar local atomistic structures. The first oxygen coordination shell shortened by 0.03 Å as a result of the annealing, compared to the 0.6 Å negative shift observed in annealed LSCF. The shortening of the first oxygen coordination is similar to the structural contraction observed in Sr and Co.

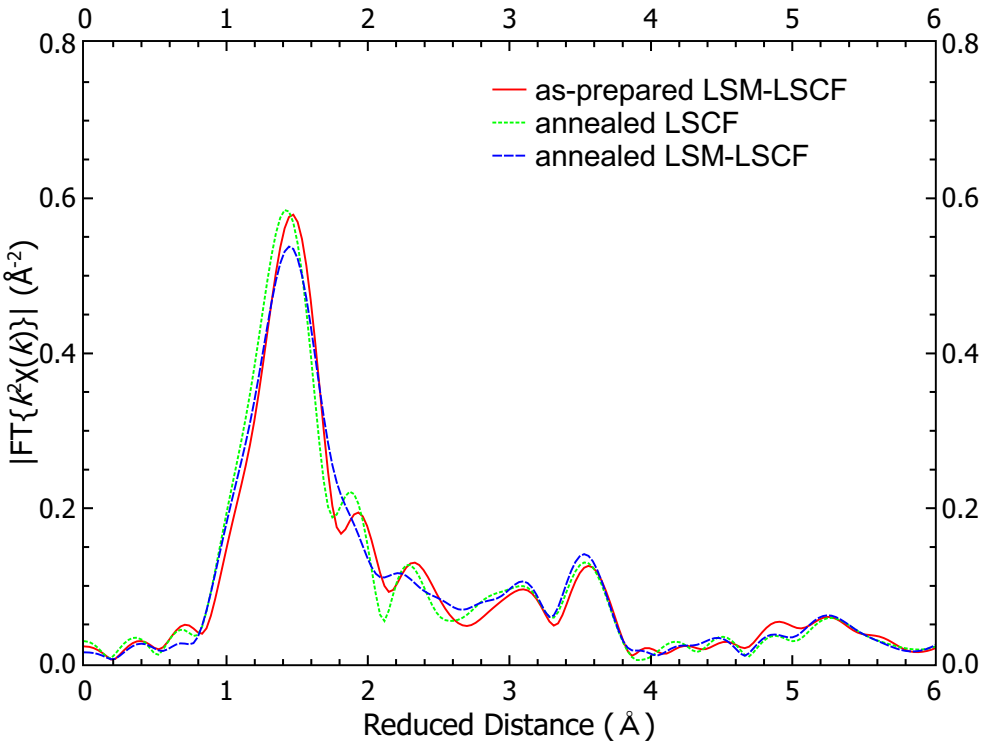

Figure 28: The Fe K-edge FT EXAFS of annealed LSCF, as-prepared LSM-LSCF, and annealed LSM-LSCF measured at ambient temperature and pressure.

The lower intensity of the first oxygen coordination shell is believed to be an effect of the aforementioned reordering reaction. Slight changes in intensity of the coordination shells farther than the first oxygen coordination shell could be attributed to Co diffusing out of the LSCF structure. The stable local structure of the Fe cation is not unexpected, given that its low diffusivity in annealed LSM-LSCF [45] and that the Fe^{3+} has a relatively stable $3d^5$ electron configuration. The unchanged local structure state of the Fe cation in the annealed LSM-LSCF is further evidence that the LSM thin film and subsequent annealing treatment help stabilize the LSCF material.

4.3 Conclusions

A series of *in situ* and *ex situ* soft and hard x-ray spectroscopies were performed under reducing or oxidizing conditions at operating temperatures for the purpose of identifying element-specific phase segregation and investigating the electronic states

and local atomistic structures of metal cations of a novel LSM-coated LSCF composite cathode. Probing the NEXAFS of transition metal cations *in situ* with soft x-rays revealed that both Co and Mn experience reduction edge shifts in as-prepared LSM-LSCF but only Co is reduced in annealed LSM-LSCF as a result of oxygen vacancy formation. Using hard x-ray *in situ* XAS, the Co cation was observed to change oxidation state in response to changing the gas atmosphere from air to nitrogen to oxygen at 750 °C while the bulk Sr oxidation state is unaffected by external stimuli. The overall local structures of Sr and Co in as-prepared and annealed LSM-LSCF are similar to as-prepared LSCF and did not strongly resemble the local structure annealed LSCF, indicating preservation of the structure on the local scale and that the solution infiltrated LSM aided in prevent degradation. Lastly, it is clear that the Fe cation is not strongly influenced by oxygen partial pressure or heat treatment. The Fe cation was determined to have a relatively stable local structure regardless of thermal treatment or gas atmosphere.

Combined, the information from the spectroscopy of the transition metal cations can support some conclusions on the interaction between LSM, LSCF, and the heat treatment. There are two major phenomena occurring: first, charge compensation of oxygen vacancies shifts preference from Mn to Co as a function of thermal treatment and second, ordering in the local structure of the Mn cation as a function of heat treatment. Since the ordering phenomenon indicates both A-site and B-site cations contributing to the increased regularity of the local structure, it is speculated that diffusion of the Mn cation into LSCF helps stabilize both the Sr and Co so that they still function for oxygen anion conduction without phase segregating, which would explain the enhanced performance of LSM-LSCF compared to the slow degradation in performance of unmodified LSCF. Further investigation of the interface between LSM and LSCF, particularly before and after annealing, and modeling, albeit limited

for such complexly-doped material systems, may help validate this hypothesis. However, based on the unresponsiveness of the Mn cation in LSM to changes in oxygen stoichiometry (via L- and K-edge XANES) and the overall increased stability in both the crystal field (via CTM4XAS) and the local structure (via EXAFS), it seems clear that, contrary to expectations in the literature [29, 17], the improvement in performance from LSM infiltration is owed to its increased structural stability and not its catalytic properties. In conclusion, a combination of *in situ* and *ex situ* XAS uniquely identified the behavior of metal cations with elemental specificity and this approach should be considered for future investigations into the electronic and local atomistic structures of complex composite cathodes designed for enhanced performance through solution infiltration of catalysts.

CHAPTER V

OPERANDO AND IN SITU SPECTROSCOPY OF THE DEGRADATION OF LSCF FROM AIR CONTAINING CARBON DIOXIDE AND WATER

In this chapter[1], we demonstrate the use of a custom-designed testing assembly for *operando* XAS studies of SOFC electrode materials under practical operating conditions. The *operando* cell may be configured for the study of cathode or anode materials and emphasizes surface information by using a glancing, incident X-ray angle, allowing key gas-solid interactions on or near electrode surfaces to be investigated under operating conditions. We studied the effects of CO_2 and H_2O gas contaminants on the electronic and local atomistic structure of the Fe and Co cations in a $La_{0.6}Sr_{0.4}Fe_{0.8}Co_{0.2}O_{3-\delta}$ (LSCF) thin film cathode of a symmetrical SOFC in operation. Together with complementary X-ray photoelectron spectroscopy (XPS) measurements, we are able to provide new insight into the poisoning mechanisms from H_2O and CO_2 under operating conditions.

5.1 Experimental details

Material synthesis method for electrochemical impedance spectroscopy: To test the LSCF thin film cell performance through electrochemical impedance spectroscopy (EIS), we fabricated quasi-symmetrical cells composed of a porous LSCF electrode that serves as the counter electrode, a dense thin film LSCF electrode that serves as the working electrode, and a thick electrolyte of gadolinium-doped ceria (GDC).

[1]Text in this chapter has been reproduced from Ref. [33] with copyright permission from John Wiley and Sons.

Dense GDC pellets were achieved by dry-pressing the GDC powders (Daiichi, Japan) at 300 MPa and sintering at 1450 °C for 5 h. A polishing process was applied for the one side of the GDC pellet and LSCF ink was screen-printed on the other side with a firing process of 1080 °C for 2 h. A dense LSCF thin film was sputtered on the polished side and annealed at 800 °C for 1 h. Since the counter electrode is highly porous, its contribution to the overall polarization resistance is much smaller than that of the thin film LSCF electrode. This is an effect resulting from the lower concentration polarization of a porous microstructure, whereas a thin film would be diffusion-limited. This has been demonstrated in our previous work [44, 45]. As a result, when the overall polarization resistance is measured and the thin film is influenced by exposure to air containing H_2O or CO_2, the change in the overall polarization resistance can be mostly attributed to the thin film. Thus, the electrochemical performance of the quasi-symmetrical cell is dominated by the thin film LSCF working electrode. Impedance spectra were acquired using a Solartron 1255 HF frequency response analyzer interfaced with an EG&G PAR potentiostat model 273A with an amplitude of 10 mV in the frequency range from 0.1 Hz to 100 kHz. Compressed air was used as the carrier gas and was mixed with the desired gas at a specific flow rate to obtain desired concentration as a volumetric percentage. To obtain 5% Ar or CO_2, for example, the flow rate of air set to 95 sccm and Ar or CO_2 as 5 sccm, respectively. To achieve a concentration of 5% H_2O, a humidifier was used to maintain the temperature of the water at 33 °C, which corresponds to a 5.04 kPa of saturated vapor pressure of water, thus 4.98% as volumetric percentage.

To prepare an ideal cell for X-ray characterization, we began with a single crystal of YSZ (1 cm x 1 cm x 0.1 cm. A quasi-symmetrical cathode cell configuration was again used, with a porous LSCF counter electrode with a $Sm_0.2Ce_0.8O_1.95$ (SDC) buffer layer and an LSCF thin film working electrode, which would be open to gas contaminants and X-rays for characterization. The porous LSCF counter electrode

with a thickness of 50 m was fabricated via tape-casting using a commercial powder from Fuel Cell Materials, as described previously [42, 45]. A 5 mm circular electrode was created by a hole puncher and was laid on top of an SDC layer, which was drop-coated as a slurry on the unpolished side of the YSZ single crystal. The assembly was co-fired at 1080 °C for 2 h before LSCF thin film cathode was sputter deposited on the polished side.

For the LSCF thin film cathode, we desired a cathode with a model geometry so that the interaction phenomenon would be limited to a controlled region of study. Thus, we attempted to fabricate a 200 nm LSCF thin film on YSZ single crystal by two stages of sputtering 100 nm. The cell was annealed at 500 °C for 1 h in air in between the sputtering stages to relieve mechanical stress and reconstruct the surface before the second stage of sputtering. A final annealing stage at 800 °C for 1 h in air was used to complete the synthesis. Electrical contacts were made using silver wire attached via silver paste. A FEI Tecnai F30 Super Twin field emission gun transmission electron microscope (TEM) with a 300 kV accelerating voltage was used to acquire the scanning transmission electron microscopy (STEM) and TEM images.

Testing assembly design: A custom furnace was designed and constructed in-house to satisfy all of the requirements for an *operando* experiment. A schematic of the furnace design is shown in Figure 29. The external housing was made using a 1.5 mm thick aluminum sheet for the furnace walls and a 3.18 mm thick aluminum sheet (both McMaster) as a support base with flanges for safe handling while the furnace was hot. Heating elements consisted of two Watlow E2J80L12H 6.35 mm diameter cartridge heaters. The cell was affixed to a 9.5 mm diameter (7.0 mm inner diameter) Type 321 high strength stainless steel tube (McMaster) using a silver-based electrically conductive adhesive (Shanghai Research Institute for Synthetic Resins). The use of a stainless steel tube aids in heat conduction to the cell, which is exposed for spectroscopy purposes. For the current collection of the top side of the cell, 0.5 mm

diameter silver wire was threaded through a two-bore 3.18 mm diameter alumina tube (Ortech, Inc.) and twisted together at the end for mechanical strength. The bores in the alumina tube helped prevent electrical shorting and the tube itself was tied to the sample holder tube using silver wires. Alumina fish spine beads were threaded on the protruding silver wire to electrically isolate a sufficient length to reach the alligator clips used by the potentiostat. The cartridge heaters, fuel cell sample holder, and the alumina tube were held in place by a pair of insulation bricks through individually machined holes. Externally, the sample holder was clamped to a crossbeam support between the support base flanges. The insulation was also hollowed out to create an air gap between the sample holder and the cartridge heaters for heat conduction. The maximum reliable temperature the cartridge heaters could reach is 700 °C. The X-ray window material used was Kapton film.

A WaveNano potentiostat (Pine Instruments) was used to apply the electrical bias. Since no reference electrode was included in the design, the counter electrode was used as the reference electrode. A key challenge of the experiment was obtaining a good fluorescent yield and signal-to-noise ratio. Traditionally, maximizing the detector's solid angle for photon capture is achieved by bringing the detector close to the sample. However, difficulties originate from the large amount of infrared light coming from the furnace and the convective heat transfer to the detector in close proximity. As a compromise, increased distance to detector and an IR filter are recommended for optimal signal quality. For detectors used in close proximity, active cooling with flowing water or another fluid is recommended both to improve signal quality and safeguard the detector's heat-sensitive components.

Another key challenge was calibration of the beam spot size to maximize incidence on the sample while using the glancing angle geometry to emphasize data collection from the surface. The sample angle must be steep enough to be reliably covered by the beam spot size but shallow enough to splay the beam across the maximum amount

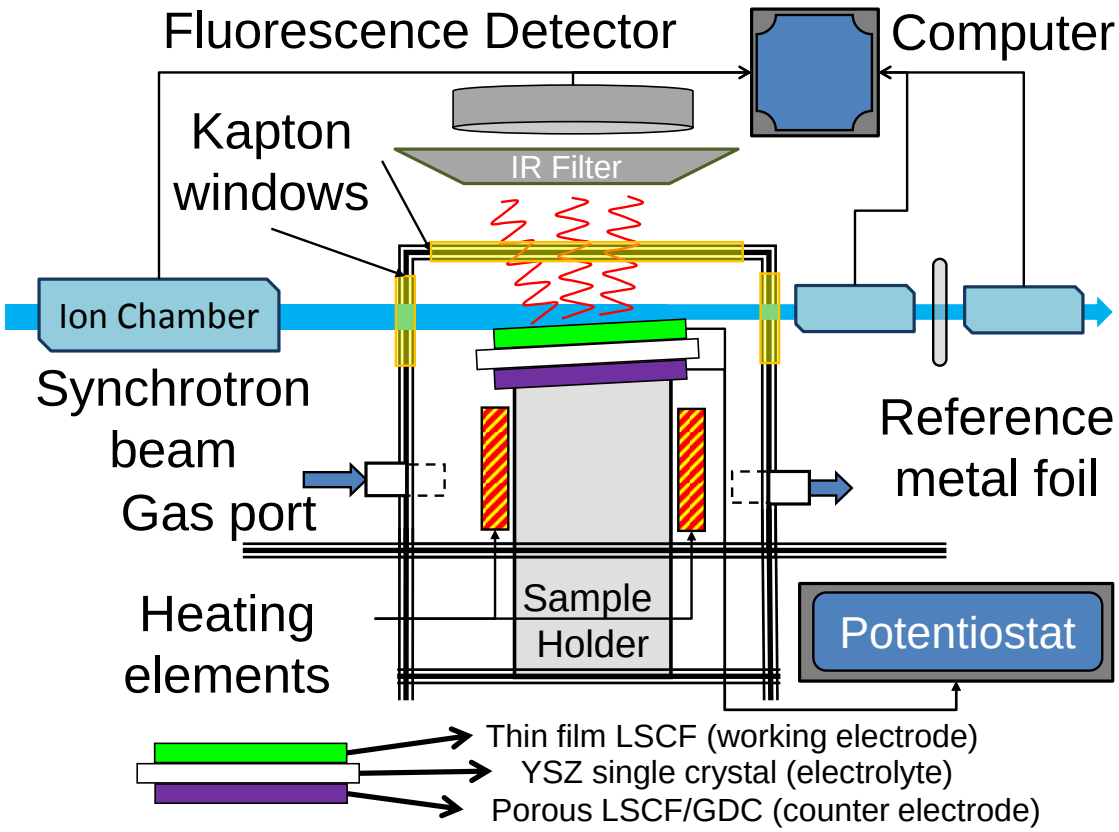

Figure 29: Schematic of the *operando* XAS testing assembly, which controls the temperature, atmosphere, and polarization while allowing a glancing incidence X-ray beam to interact with a sample and a reference foil through Kapton film windows. Reproduced with permission from reference [33].

of area. Additionally, a sufficient amount of the beam must pass over the sample into the downstream ion chambers for measurement of the reference foil's absorption. A shallow angle of 2° will splay a beam with a 1.0 mm vertical height across 28.7 mm of angled length, which is sufficient to cover a 10 mm long sample (that only blocks 0.35 mm of the vertical beam height at a 2° angle) and extends over the sample into the downstream reference ion chambers. With respect to the information depth, the absorption length of the LSCF using 7.112 eV (Fe K-edge) photons is 7.2 µm, which at a 2° incident angle, results in an incident photon penetration depth of about 250 nm normal to the surface. Although photons can penetrate beyond one absorption length, due to the exponential decay of Beer's Law, the majority of the signal originates from within the first absorption length.

To achieve the aforementioned considerations experimentally, a large piece of fluorescent paper was used to optimize the initial beam spot size. After the *in situ* testing assembly was in place, a thin square of fluorescent paper was laid over the sample and used to further optimize the beam size, sample height, and angle. After removing the fluorescent paper, the sample height was then adjusted to correct for the thickness of the fluorescent paper.

5.1.1 *Operando* experimental conditions

The temperature recorded is based on a K-type thermocouple placed inside of the furnace. The gas contaminant was introduced via a glass pipet inserted through a small hole in the Kapton X-ray window and positioned toward the cell but not in the path of the X-ray beam. To introduce water vapor, nitrogen as a carrier gas was bubbled through a heated flask of water between 55 °C to 60 °C. The electrical polarization is the voltage across the whole cell as applied by the potentiostat. The combinations of testing parameters are shown in the Table 3.

Table 3: Experimental conditions during the *operando* experiment. Flow of gas contaminant was 30 mL min^{-1} when not using ambient air. Reproduced with permission from reference [33].

Classification	Temperature (°C)	Electrical polarization	Gas contaminants
in situ	400	open circuit	air, CO_2
in situ	700	open circuit	air, CO_2
operando	400	applied, −1.0 V	air, CO_2, 18 to 20% H_2O in N_2
operando	700	applied, −1.0 V	air, CO_2, 18 to 20% H_2O in N_2

5.1.2 X-ray absorption spectroscopy

XAS was performed at Beamline X18B of the National Synchrotron Light Source (NSLS) at Brookhaven National Laboratory (BNL). Incident photon energy was calibrated using an Fe foil and set at 7112.0 eV. The beamline uses a channel cut Si(111) double monochromator system with vertical and horizontal slits to control the beam spot size to be 8 mm wide and 1 mm in height. Higher harmonics are suppressed by detuning the second monochromator crystal to allow 70% of the maximum intensity using a piezoelectric picomotor. Ionization chambers filled with the appropriate mixture of nitrogen and argon gas were used to measure the incident, transmitted, and reference X-ray intensities. A passivated implanted planar silicon (PIPS) detector was mounted overhead to capture the fluorescent X-ray signal.

5.1.3 X-ray photoelectron spectroscopy

Synchrotron-based soft XPS was performed at Beamline U12A of the NSLS at BNL using a photon energy of 600 eV for high surface specificity. The same kind of LSCF thin film symmetrical cathode sample was mounted on a tungsten wire heating stage attached to the manipulator arm. Reference photoelectron spectra were collected at 25 °C and 750 °C under UHV without any *in situ* gas exposure. Afterward, the sample was cooled to 25 °C in an equal mixture of H_2O and CO_2 at a roughly constant

partial pressure. After evacuating the chamber to UHV conditions, the photoemission spectra were collected again.

5.1.4 Data analysis

Data processing for the x-ray absorption data was performed using the Athena program in the Demeter software package [60]. Multiple scans were deglitched by hand, aligned using derivatives of the accompanying reference foil scan, merged using raw absorption μ(E), and normalized by hand-picked pre-edge and post-edge ranges, which were optimized for maximum range and linearity. Smoothing was conducted with three-point averaging for eleven repetitions. The energy scale was calibrated using the data from a Fe reference foil. Some R_{bkg} values were adjusted slightly but typically a value of 1.0 was sufficient. Edge shifts in energy were measured according to the difference in the derivative curves at the abscissa. A Hanning window was used for the forward Fourier transform and chosen in the k-space region where the signal-to-noise ratio was acceptable. Since data were compared across the same temperatures, the same k-range was used for each set of data. Radial distances in the Fourier-transformed data were not corrected for phase shift.

For the XPS data, the binding energy scale was calibrated by setting the adventitious carbon peak to 284.8 eV. For normalization of the intensity, raw intensity counts were divided by the product of the number of scans, the dwell time for energy step (constant for all scans), and the mesh current, which accounts for the gradual decay in the intensity of the incident synchrotron beam. The normalized data were then imported into XPSPeak v4.1 for background subtraction using a Shirley background.

5.2 Electrochemical performance

Figure 30 shows a cross-sectional view of a thin-film LSCF cathode deposited on a single crystal YSZ substrate. The thickness of the LSCF film is about 70 nm and is clearly porous. The thin film allows the X-ray to probe the triple phase boundaries

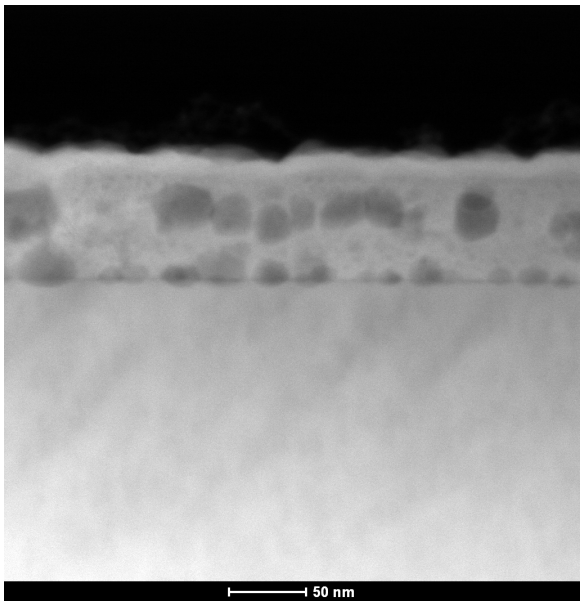

Figure 30: TEM image of the LSCF thin film cross-section. Reproduced with permission from reference [33].

at the cathode/electrolyte interface while the porosity creates high specific surface area of LSCF so that there are more atoms active in the solid/vapor interface region. Figure 31 shows some typical impedance spectra of the test cells with thin-film LSCF in the presence of 5% Ar, 5% CO_2, and 5% H_2O at 750 °C. The use of 5% Ar is to eliminate the Nernst effect, or the contribution from a difference in oxygen partial pressure due to the dilution of oxygen when air is mixed with other gases (e.g., CO_2 and H_2O). The polarization resistance is 2.4% and 8.4% higher for CO_2 and H_2O, respectively, meaning that both cause degradation in the performance of the LSCF cathode at operating temperatures. Corresponding impedance spectra at 600 °C are shown in Figure 63 in the Appendix.

5.3 Operando *XAS*

Figure 31 shows the correlation between the rigid shift in the XAS edge energy and the percentage change in polarization resistance as a function of temperature and

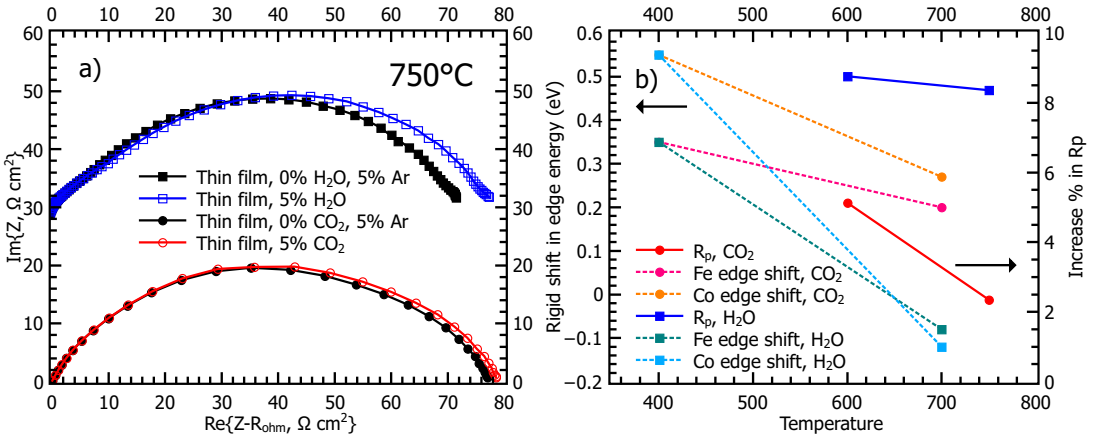

Figure 31: a) Impedance spectra of a thin film LSCF cathode show the increase in polarization resistance caused by H_2O and CO_2. b) The correlation between performance, operating conditions, and rigid shifts in absorption edge energy can be observed. Reproduced with permission from reference [33].

gas contaminant. An increase in the binding energy of electrons in core-hole spectroscopy (XAS, XPS) is related to a net electron transfer away from the absorbing atom, which chemically corresponds to oxidation. At lower temperatures, both Fe and Co cations tend to become oxidized and the polarization resistance tends to increase. With increasing temperature, the positive shift in the edge energy (indicating oxidation) decreases with H_2O, showing a stronger temperature dependence than CO_2. While exposure to H_2O results in an overall higher polarization resistance, the relative change in polarization resistance due to temperature is larger for exposure to CO_2. The trend may be caused by a saturation effect of H_2O on the surface, which could be corroborated by the shift in edge energy. In contrast, the shift in edge energy from exposure to CO_2 is less significant but the polarization resistance is more influenced by temperature. This phenomenon is the first indicator that while both H_2O and CO_2 cause performance degradation, the nature of the interactions with the LSCF cathode is distinctly different, as will be discussed later.

Operando XAS was performed to better understand the chemical influences of temperature and gas contaminants like CO_2 and H_2O under operating conditions.

Figure 32 shows the derivative of the normalized absorption for Fe and Co, which more clearly depicts the rigid shifts in edge energy in the XANES region. Examples of the full XAS spectrum (Figures 68 and 69) in energy space are included in the Appendix. When the cathode is cathodically polarized, the presence of CO_2 causes a slight oxidation of Fe and Co while that of H_2O has a slightly reducing or no effect on the oxidation state. The edge energy shifts in Fe and Co under CO_2 are 0.20 eV and 0.27 eV, respectively, referenced to their polarized state under air without contaminants. The oxidizing effects of CO_2 are supported by the Fourier-transformed extended X-ray absorption fine structure (FT-EXAFS) of Fe and Co, in which a significant increase in the magnitude of the first-shell coordination peak represents an increase in the number of oxygen bonds relative to the cathode in air. Conversely, the magnitude of the first-shell coordination peak decreases when H_2O is introduced.

Additionally, H_2O has little influence on the overall local structure of the Fe but significantly affects the Co local structure. The new peak is lower in magnitude and has a broader full width half maximum (FWHM) than the first-shell coordination peak, which is likely due to the convolution of two smaller peaks, and the phase-shift uncorrected length is 0.31 Å longer. It is speculated that the local structure distortion is caused by elongated Co bonds, which could be to a hydroxide or carbonate ligand based on the gas contaminant introduced. Further insight into the chemical phenomena is provided by synchrotron-based XPS, as discussed later.

At 400 °C, the degree of oxidation is increased in both Fe and Co, as shown in Figure 33, which correlates with the larger degradation in performance at lower temperatures. The edge energy shift is approximately the same whether the cathode is exposed to CO_2 or H_2O and is 0.35 eV and 0.55 eV for Fe and Co, respectively. As previously exhibited by the FT-EXAFS at 700 °C, an oxidation shift in the edge energy is accompanied by an increase in the magnitude of the first-shell coordination peak, representing the increase in the number of oxygen ligands caused by exposure

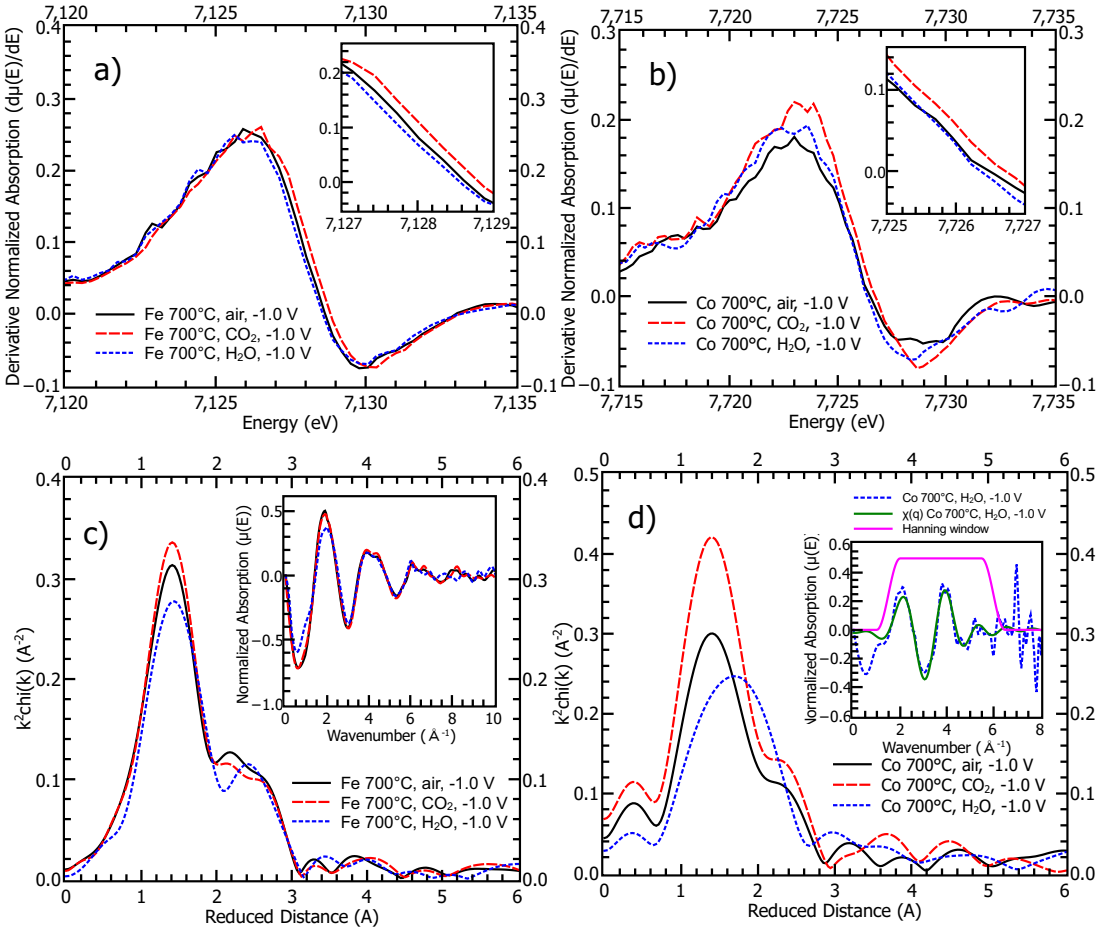

Figure 32: The derivative of the near-edge absorption of a) Fe and b) Co at 700 °C under cathodic bias while exposed to H_2O and CO_2. Closer views of the edge shift are provided in the insets. The EXAFS data for c) Fe and d) Co support the observation of oxidation. The inset in c) shows the wavevector form of the absorption spectroscopy. The inset in d) compares the wavevector form of the spectrum under H_2O exposure to the backwards Fourier transform X(q) and indicates the window used for the forward Fourier transform. A k^2 factor was used to weight the relative variation in the absorption coefficient, $\chi(k)$, before the Fourier transform. Reproduced with permission from reference [33].

to CO_2 and H_2O. Beyond the first-shell coordination, the overall Fe local structure is relatively stable. The Co local structure also exhibits similar evidence of oxidation, based on the increase in magnitude of the first-shell coordination peak and a relatively stable structure with none of the deformations observed at 700 °C.

5.4 In situ *pump-probe XPS*

Synchrotron-based XPS was performed to complement the *operando* XAS results with a highly surface sensitive technique that could better identify new ligand formation, particularly carbonates. The C 1s photoemission spectra shown in Figure 34 belong to the as-prepared LSCF thin film at 25 °C, 750 °C, and 25 °C after cooling in an equal mixture of H_2O and CO_2. The reference condition indicates that the spectrum was collected under ultrahigh vacuum (UHV) conditions without an immediately prior exposure to CO_2 and H_2O. The adventitious carbon peak at 284.8 eV was used for calibrating the binding energy scale. At a higher binding energy of 288.4 eV, a small shoulder can be identified as related to C 1s emission from a carbonate type of species. As this species is present on the sample prior to the thermal and exposure treatments that follow, this feature is ascribed to adventitious carbonate on the surface. The binding energy of the shoulder peak closely matches literature values for various carbonate species. [68, 76, 75] The shoulder peak is clearly absent in the spectrum collected at 750 °C. It is presumed that the carbonate species that previously existed decomposed into CO_2 and the respective oxide. After cooling in the presence of H_2O and CO_2, the carbonate peak reappears, implying that the carbonate species reformed on the surface during the thermal quenching of the LSCF thin film.

In Figure 35, the Fe and Co 3p photoemissions are shown. The Fe photoemission is relatively stable, showing slight oxidation at high temperature and slight reduction upon cool down under H_2O and CO_2. In contrast, no Co 3p photoemission is detectable at room temperature, which is typically in the range of 59 eV to 61 eV

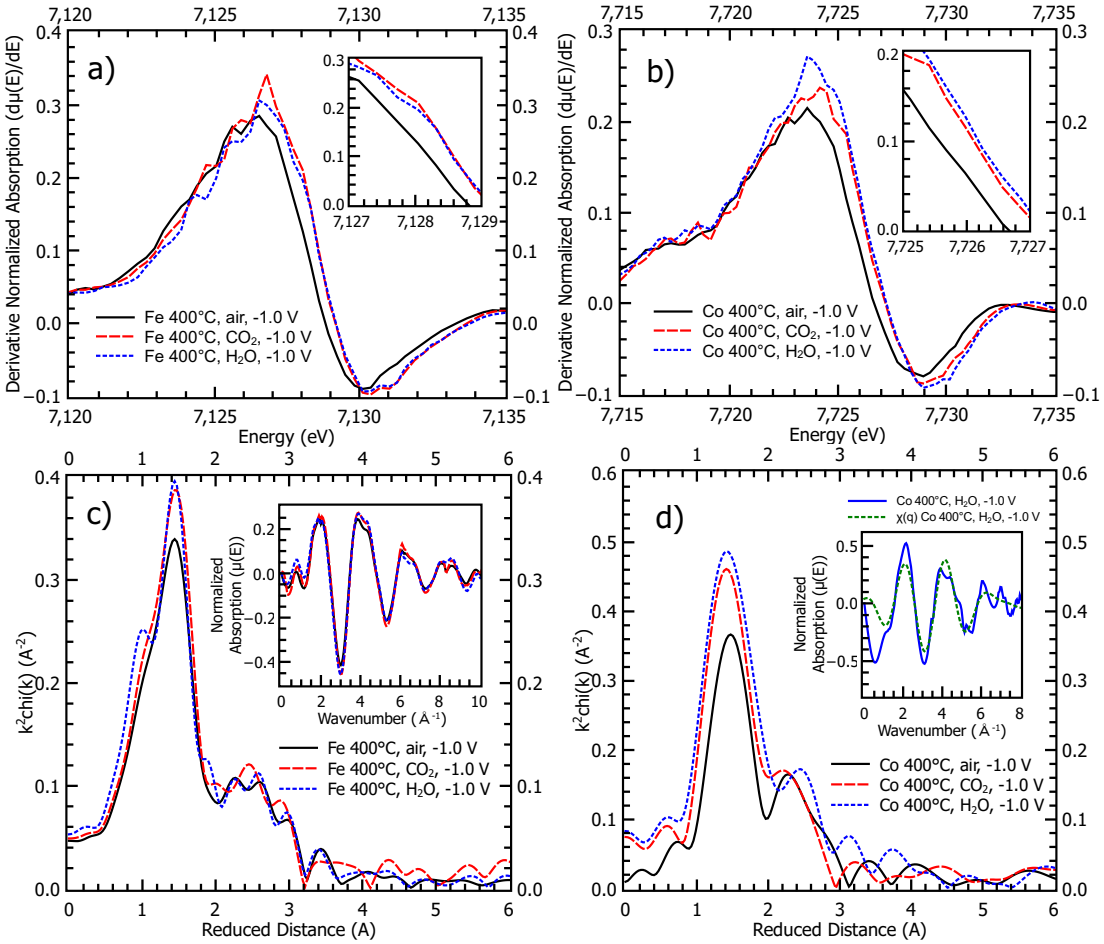

Figure 33: The derivative of the near-edge absorption of a) Fe and b) Co at 400 °C under cathodic bias while exposed to H_2O and CO_2. Closer views of the edge shift are provided in the insets. The EXAFS data for c) Fe and d) Co support the observation of oxidation. The inset in c) shows the wavevector form of the absorption spectroscopy. The inset in d) compares the wavevector form of the spectrum under H_2O exposure to the backwards Fourier transform X(q) and indicates the window used for the forward Fourier transform. A k^2 factor was used to weight the relative variation in the absorption coefficient, $\chi(k)$, before the Fourier transform. Reproduced with permission from reference [33].

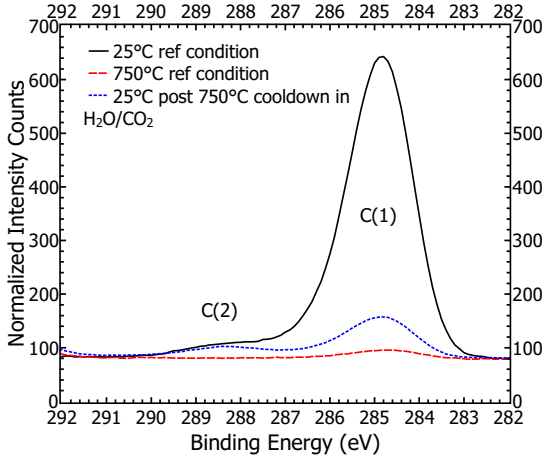

Figure 34: XPS results which indicate that carbonate formation disappears at high temperature and then reappears on cooling in the presence of CO_2 and H_2O. The reference condition indicates measurement of spectra under UHV conditions without an immediately prior exposure to CO_2 and H_2O. Reproduced with permission from reference [33].

for the 2+ and 3+ oxidation states. [49, 15] Upon heating, a new peak at 64 eV is formed, which is believed to be Co-related but there is little literature to identify a formal peak at such a high energy. The current assumption is that the Co species is a Co_{3+} species with highly electronegative ligands. After cooling down under H_2O and CO_2, the new photoemission peak remains, suggesting that the Co-containing phase was irreversibly formed, and shifts to lower binding energy. This new Co-containing phase is presumed to be an oxide resulting from the decomposition of the carbonate. The bonding of hydroxide ions to the oxide during the cool down, as evidenced below by the O 1s photoemission, would cause a net reduction in the Co oxidation state and thus, a shift in the 3p photoemission to lower binding energy.

Also shown in Figure 35 is the O 1s photoemission. At room temperature, the main peak labeled O(1) is attributed to surface oxygen, although other possibilities have been suggested, [72, 18] while the lesser peak labeled O(2) at 529.6 eV can be matched to lattice oxygen. [72, 24] Since the peak at high binding energy increases, rather than diminishes, at 750 °C, the temperature at which the carbonate signal was depleted,

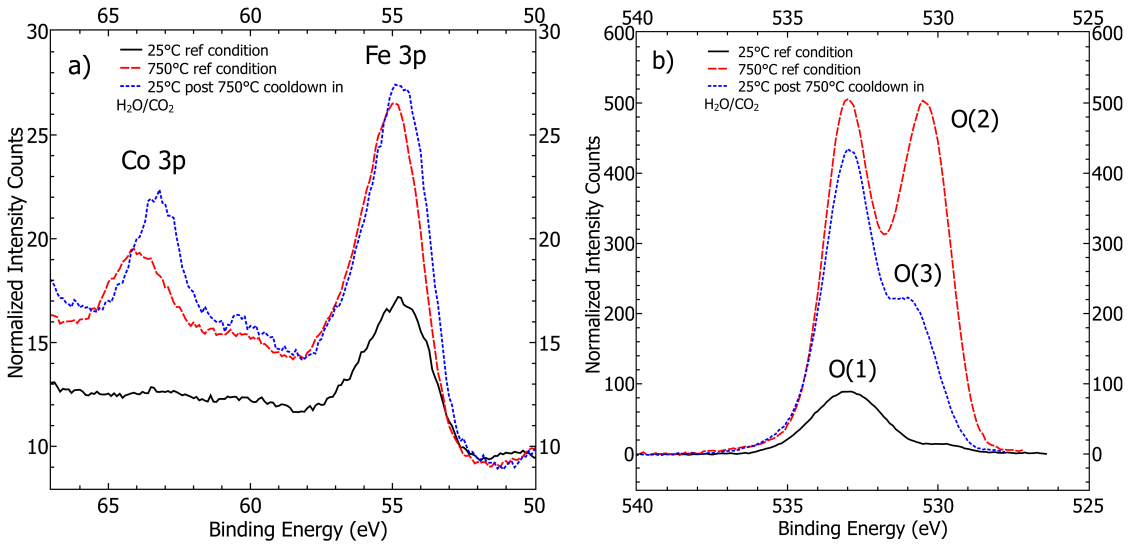

Figure 35: a) Fe and Co 3p and b) O 1s photoemissions from XPS. O(1), O(2), and O(3) identify photoemission peaks characteristic of surface oxygen, lattice oxygen, and hydroxide oxygen species, respectively. Reproduced with permission from reference [33].

it is concluded that the O(1) peak is not solely representative of oxygen in carbonate but the signal is likely convoluted. Upon heating, adventitious carbon is removed, which increases overall signal intensities, and the carbonate decomposes into an oxide, which populates the surface with oxygen in a lattice valence state. The cool down under H_2O and CO_2 causes significant hydroxide and carbonate formation, the former resulting in the peak shoulder photoemission, labeled O(3), which is characteristic of oxygen in a hydroxide, [49, 6] and the latter contributing to the greater intensity of the O(1) peak relative to the initial reference condition.

To separate and identify the individual contributions of different operating parameters, *in situ* XAS was performed under varying conditions. In Figure 64 in the Appendix, the presence of CO_2 causes a slight edge energy shift of 0.07 eV in Fe at 700 °C. When the same experiment was performed with cathodic bias, the edge energy shift in Fe was 0.20 eV. In the case of Co, the presence of CO_2 caused an edge energy shift of 0.21 eV at 700 °C. The same experiment with cathodic bias caused an edge energy shift of 0.27 eV. Again, the influence of cathodic bias led to a larger

magnitude shift in the edge energy. In Figure 65 in the Appendix, it can be seen that, as with the *operando* results, the oxidizing effect of CO_2 is greater at 400 °C than at 700 °C. The edge energy shifts are 0.29 eV and 0.34 eV for the Fe and Co edges, respectively, compared to 0.35 eV and 0.55 eV edge shifts as measured *operando* at 400 °C. As with the trend at 700 °C, the *operando* results at 400 °C indicate a greater magnitude in edge energy shift, which implies that the cathodic bias caused more severe oxidation.

The influence of cathodic bias was examined *in situ*. Shown in Figure 66 in the Appendix, is the derivative of the Fe XANES spectrum after normalization, with and without polarization at 400 °C. The application of a cathodic bias caused an edge energy shift of −0.11 eV, which is expected as a cathodic bias would have a slight reducing effect. A similar effect was observed in the Co XANES spectrum under the same conditions, as seen in Figure 67 in the Appendix.

Figure 36 summarizes how the edge shifts in energy caused by exposure to CO_2 were greater for both Fe and Co under *operando* conditions than they were under *in situ* conditions without polarization at both 400 °C and 700 °C. The presence of CO_2 has an oxidizing effect and cathodic bias exacerbates the degree of oxidation as measured by the shift in the absorption edge energy.

The combined results of the *operando* XAS and the synchrotron XPS provide some useful insights into the chemical phenomena, particularly on the differences in the influence of H_2O and CO_2. Based on the synchrotron-based XPS results, it is speculated that the carbonate species forms with Co at room temperature, according to Equation 12. At high temperature, the carbonate species decomposes into Co_3O_4 and releases CO_2 per Equation 13. Subsequent exposure to CO_2 results in slight oxidation of Fe and Co. Thus, the adsorption of CO_2 was consuming oxygen vacancies on the surface and slightly increasing the polarization resistance. Continuous formation and decomposition of $CoCO_3$ from high temperature exposure to CO_2

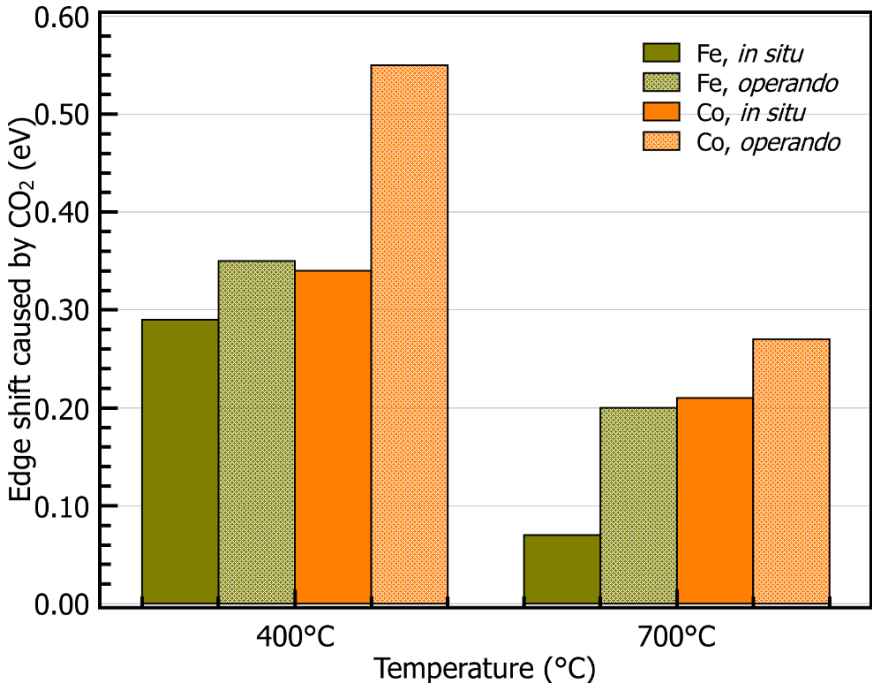

Figure 36: Absorption edge shift in energy in both Fe and Co caused by the presence of CO_2 at 400 °C and 700 °C. The shift is greater in *operando* experiments than in *in situ* experiments. Reproduced with permission from reference [33].

would contribute to long-term degradation. The proposed reaction mechanisms are depicted schematically using Kröger-Vink notation in Figure 37, and in Eqs. 12 and 13, where superscript 'X' indicates a neutral charge relative to the nominal charge in a stoichiometric lattice.

$$CO_2 + Co_{Co}^X + O_O^X \rightleftharpoons CoCO_3 \tag{12}$$

$$3CoCO_3 + O_O^X \rightleftharpoons CO_3O_4 + 3CO_2 \tag{13}$$

The role of H_2O also has a significant effect on both the oxidation states and local structure. Given that the exposure to H_2O appeared to cause oxidation in Fe and Co at 400 °C, it would be expected that the same effect, but to a lesser degree would occur at 700 °C, similar to what was observed from CO_2. The increase in polarization resistance during H_2O exposure observed in the impedance measurements also supports this expectation. However, the effect of H_2O on the oxidation of Fe and Co at 700 °C was slightly reducing or negligible, respectively. One plausible explanation

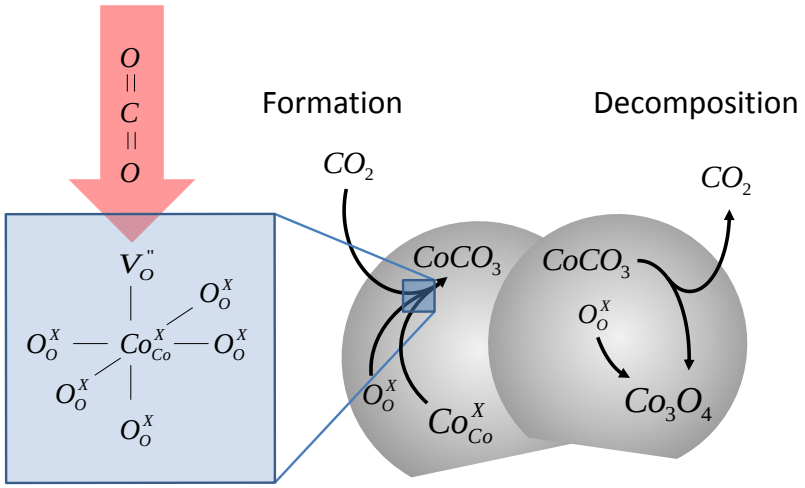

Figure 37: Reaction mechanisms proposed for the formation and decomposition of cobalt carbonate, using KrögerVink notation. The CO_2 is hypothesized to bond to the Co atom in the octahedral site through an oxygen vacancy. Reproduced with permission from reference [33].

is that if hydroxide anions were to replace oxygen anions in the perovskite lattice, the net result could be that the Fe and Co cations experience a slight reduction. As hydroxide anions diffuse into the bulk, they would also impede the diffusion pathways for oxygen vacancies, resulting in the observed increased polarization resistance. Disruption of the diffusion pathways for oxygen vacancies below the surface could explain why the magnitude of the increase in polarization resistance is greater under H_2O relative to CO_2.

Water vapor was also observed to have a significant effect on the Co local structure but less so on the Fe structure. If the deformation in local structure in Co is attributed to the formation of Co_3O_4, then the presence of water may likely assist in that reaction. For example, a hydroxide anion may provide a source of oxygen anions to form carbonate ligands. Since the X-ray beam is probing to some extent into the

bulk, a combination of both nominal Co in the LSCF structure and Co in the segregated oxide phase would contribute to the broad FT-EXAFS peak. The presence of a segregated Co oxide is also supported by the Co 3p and O 1s photoemissions in XPS. The indication that a Co oxide is forming could explain the gradual but continuous long-term degradation behavior. On the other hand, Fe cation FT-EXAFS does not indicate significant change in the local structure when exposed to H_2O and its photoemission shows relatively little change during high temperature or after reaction with H_2O and CO_2. It should be noted that loss of B-site cations due to phase segregation could lead to A-site cation stoichiometric imbalance, resulting indirectly in the widely observed Sr segregation. [14, 28, 10] The susceptibility of Co to diffusion and phase segregation, as suggested by both FT-EXAFS and XPS, should be explored in future experiments.

The *operando* results at 400 °C show that both H_2O and CO_2 exhibit strong oxidation effects on Fe and Co. Both the Fe and Co local structures indicate an increase in the magnitude of the first coordination shell peak, suggesting that the oxygen vacancies are depleted, which explains the increase in the polarization resistance observed in impedance spectroscopy. However, the Fe and Co FT-EXAFS results did not show a significant difference between the CO_2 and H_2O. The reason these effects differ from those observed at high temperature may also be because the carbonate species present at room temperature, as detected by XPS, may be stable on the surface at 400 °C and prevent H_2O from interacting with the Fe and Co and diffusing further. It may be that high temperatures, at which the carbonate decomposes, are required for the H_2O to have an influence.

One of the key aspects of this study was to demonstrate the unique capabilities and advantages of *operando* experiments. The *in situ* experiments indicate that the cathodic bias has a reducing effect and the CO_2 had an oxidizing effect on both Fe and Co. However, in the *operando* experiment, the presence of cathodic bias

increased the degree of oxidation caused by CO_2. Therefore, the combined effects cannot be predicted by a linear sum. The effect of cathodic bias may be attributed to generating partially reduced oxygen species that can react with CO_2 on the surface to form carbonates ligands. If these surface carbonates bond to the transition metal cations via an oxygen atom occupying an oxygen vacancy, then the overall oxidation state of the transition metal cations would increase. This effect may be less apparent at high temperatures because the carbonate would be decomposing and the remaining oxygen atom could diffuse to the substrate. At lower temperatures, an accumulation of stable carbonate surface species could lead to a greater average oxidation state of Fe and Co. Without the cathodic bias to catalyze the oxygen reduction reaction, fewer carbonate species on the surface would then lead to less oxidation of Fe and Co and thus explain the smaller shifts in edge energy observed in the *in situ* experiments. These phenomena emphasize the uniqueness and necessity of *operando* experiments to obtain better insights into the fundamental mechanisms at work.

5.5 Conclusions

We have designed and implemented an *operando* SOFC testing assembly capable of probing the electronic and local atomistic structure of a specific element in an operating cathode of a quasi-symmetrical cell with proper control of temperature, gas contamination, and electrical polarization. These *operando* experiments provided useful insight into the different influences of CO_2 and H_2O on the Fe and Co cations of the LSCF thin film cathode. It was found that the magnitude of the increase in polarization resistance is correlated with the degree of oxidation according to the shift in edge energy for both Fe and Co, but the influence of temperature on the polarization resistance differed between H_2O and CO_2. The XANES indicated that CO_2 had slightly oxidizing effects while H_2O had a neutral effect on Co and slightly

reducing effect on Fe at 700 °C. However, the FT-EXAFS showed that Co local structure underwent significant deformation in the first coordination shell, resulting in an elongated bond length. Meanwhile, the Fe local structure appeared to be relatively stable and only increased in the magnitude of the first coordination shell peak, indicating filling of oxygen vacancies by lattice oxygen, carbonate, or hydroxide ligands. Synchrotron-based XPS complemented the *operando* XAS by providing information about the stability of the carbonate species at 400 °C and its instability at 750 °C. The combination of these techniques, along with impedance spectroscopy and *in situ* XAS, enabled us to speculate that the Co cation is particularly susceptible deformation in the local structure and phase segregation over time, and thus, it should be the focus of future investigations and rational materials design. Lastly, a comparison of the results from *operando* and *in situ* testing revealed that *operando* results cannot be predicted by their *in situ* components, strengthening the rationale for pursuing challenging *operando* experiments.

It is presumed that H_2O may play a key role in the transformation of CO_2 to CO_3^{-2} readily. However, further investigations using high pressure synchrotron-based XPS are warranted to fully elucidate the details of CO_2 and H_2O interactions under *operando* techniques. *Operando* experiments, such as those described above, will also be of further use in understanding how solution-infiltrated coatings for SOFC electrode materials confer their beneficial properties.

CHAPTER VI

X-RAY SPECTROSCOPIC AND SCATTERING STUDIES ON NICKEL-BZCYYB ANODES UNDER HYDROGEN SULFIDE

The motivation for using X-ray absorption spectroscopy (XAS) is to obtain unique yet relevant electronic and structural information. By using XAS, we can obtain the electronic state and local coordination by an element-specific basis. These types of experiments enable the ability to fundamentally study the influence of external stimuli on particular cations and correlate their response with other data to explain observed changes in performance. In this particular experiment, our goal is to determine the particular elements that sulfur interacts with and how sulfur and nickel may affect the local atomistic structure of key cations important to the sulfur tolerance observed in BZCYYb.

6.1 Experimental details

6.1.1 *Ex situ* XAS

BZCYYb was synthesized by a conventional solid-state reaction. Stoichiometric amounts of barium carbonate, zirconium oxide, yttrium oxide, and ytterbium oxide were were mixed, ball-milled in ethanol for 24 h, dried in a vacuum oven, and fired at 1050 °C for 5 h.

To simulate the interaction between H_2S and BZCYYb as an electrolyte, as-synthesized BZCYYb was ground in a mortar and pestle for 30 min and 300 mg were used to form a 13 mm pellet by using 2000 kg of force. The formed pellet was fired at 1400 °C for 5 h in air to sinter.

To simulate a composite anode used in operating fuel cells, nickel oxide was mixed in with as-synthesized BZCYYb at a 65:35 weight ratio, hereby known as NiO-BZCYYb, which equates to a 1:1 volume ratio after reduction. The powders were mixed, ball-milled in ethanol for 24 h, dried in a vacuum oven, and then ground in a mortar and pestle for 30 min and formed into a 13 mm pellet by using 2000 kg of force before being fired at 1400 °C for 5 h in air. After firing, the pellets were ground again and pressed at 2000 kg to reform into a pellet.

Both BZCYYb and NiO-BZCYYb pellets were loaded into an alumina boat on a bed of YSZ powder and sealed inside a reaction tube. The assembly was loaded into a furnace and heated to 750 °C under H_2 to first reduce. Then, 50 ppm of H_2S in H_2 was introduced and the samples were exposed for several hours. After exposure, the samples were quenched at room temperature under H_2 atmosphere by removing the reaction tube from the furnace. The samples were then quickly extracted and transferred to an argon glovebox to protect the surface sulfur from gradual oxidation by the environment. Inside the glovebox, the samples were sealed with Kapton tape for transport.

X-ray absorption data were collected using bending magnet radiation at the X23A2 endstation of the National Synchrotron Light Source. A Si(311) monochromator with a single-bounce, harmonic rejection mirror was used in a fixed exit Golovchenko-Cowan design and was stabilized using piezoelectric feedback. Mechanical beam slits were used to collimate the beam to a spot size of about 3.5 mm in width and 0.5 mm in height and a four-element Vortex silicon drifts fluorescence detector. To maximize the quality of data, the dilute elements in the samples were measured in fluorescence mode. The samples were then diluted with boron nitride to measure concentrated elements in transmission mode and avoiding significant self-absorption.

6.1.2 *In situ* XAS

Patterned Ni electrodes were sputtered onto a sintered BZCYYb pellet (prepared like *ex situ* XAS samples) via radio frequency (RF) sputtering under a 2.5×10^{-2} mbar pressure and a constant power of 20 W. A square mesh grid with 40 µm spacing was used to make the patterned electrode. Samples were then mounted on a stainless steel tube using silver paste.

A custom-made testing apparatus similar to the one used for *operando* cathode XAS experiments was used for the *in situ* XAS on anodes. The design is analogous to that shown in Figure 29, except more compact and with the heating element inside the cell mounting tube. Additionally, the upper portion of the testing apparatus that contains the dead volume for the gas was fitted with Swagelok fittings for gas flow inlet and outlet and a septum rubber stopper port above a short, 5 mm-diameter glass dish. To generate H_2S gas *in situ*, a small piece of FeS is placed inside the glass dish and 0.3 mL of concentrated HCl is added via a syringe through the septum port. The purge gas was 5 % H_2 in He.

Beamline X18B at the NSLS was used to measure the Ni and Yb K-edge XAS. Similar to Beamline X23A2, it uses bending magnet radiation through a Si (111) channel cut monochromator with similar detuning measures in place. For *in situ* experiments, like the *operando* experiments for the cathode, a glancing angle was used to splay the x-ray beam over the area of the sample while allowing some of the beam to pass over the sample into a reference channel where Ni foil was used. A passivated implanted planar silicon (PIPS) detector was wrapped with Al foil to block strong infrared signals and mounted above the testing apparatus to capture the fluorescent X-ray signal.

6.1.3 *In situ* synchrotron XRD

The XRD and PDF experiments used the same NiO and BZCYYb as the *ex situ* XAS. Each sample was packed between two pieces of glass wool in a 1 mm quartz capillary tube. A thermocouple was inserted the quartz capillary tube close to the sample and the testing apparatus was assembled with graphite gaskets, Swagelok fittings, and tungsten heating element. The testing apparatus was mounted to the sample holder in the hutch of Beamline X7B and connected to the gas system to be purged with nitrogen or hydrogen gas. The gas flow rate was $10\,\mathrm{mL\,min^{-1}}$.

The energy of the x-ray beam was fixed to 38.8 keV during the experiment. A 2048-by-2048 pixel area detector set 39.98 cm from the sample was used to measure the scattering. A typical scan measured 5 exposures for 4 s each, including corresponding dark exposures, and averaged them together. Since the wavelength of the X7B beamline is 0.1396 Å, a simple proportional equation using Bragg's Law must be used to convert the 2θ angle so that it matches the same scale seen for Cu K-α_1 radiation, which has a wavelength of 1.5406 Å. Using the Bragg's Law (Equation 9, the following relation can be derived:

$$\frac{\lambda_1}{\lambda_2} = \frac{sin(\theta_1)}{sin(\theta_2)} \tag{14}$$

For *in situ* experiments with H_2S, a round-bottom flask and gas bubbler was connected in line with the gas flow into quartz capillary tube. The flask was filled with distilled water and small pieces of FeS. When the experiment needed to change the gas to include H_2S gas, 1 mL of 3.7 % HCl was added to the flask and the 5 % H_2 in He purge gas flowrate is reduced to $5\,\mathrm{mL\,min^{-1}}$. When bubbling was observed to slow, roughly every 30 min, additional amounts of HCl were added.

6.1.4 *In situ* PDF

The experimental procedure for the *in situ* PDF is identical to the *in situ* XRD experiments performed at X7B except that the area detector is moved closer to the

sample to capture higher 2θ angles. The distance between the sample and detector was 12.06 cm.

The *in situ* pair distribution function experiments were performed using the same experimental set up as the x-ray diffraction. As with the *in situ* XRD data, NiO and BZCYYb were first examined individually. Since crystalline materials have significant numbers of coordinated pairs of atoms, the PDF data are much more populated with peaks and troughs than with XRD. As a result, the figures were constrained to a shorter range of distances from 0 Å to 15 Å in order to more clearly identify the differences between samples.

As with the XRD data, the change in temperature also causes a subtle shift in the data. In contrast to the XRD temperature phenomenon, the bowed or curved shape of the data is instead convex shaped. This result is because the PDF is plotted in real space, meaning that the thermal expansion of the crystal structure is directly represented by peak shift to higher R in the PDF. The thermal expansion effect is also cumulative and thus is more influential at larger distances. This cumulative effect is easily detected by the increased curvature of the "boomerangs" in Figure 55 at further distances. The thermal expansion effect is quantified more precisely later at a more relevant point in the analysis.

6.1.5 Data analysis

Data processing for the XAS data was performed using the Athena program in the Demeter software package [60] and procedural steps are identical to those in Sections 3.5 and 5.1.4. Data analysis of the XRD and PDF data follow the steps described in Section 3.5.3.

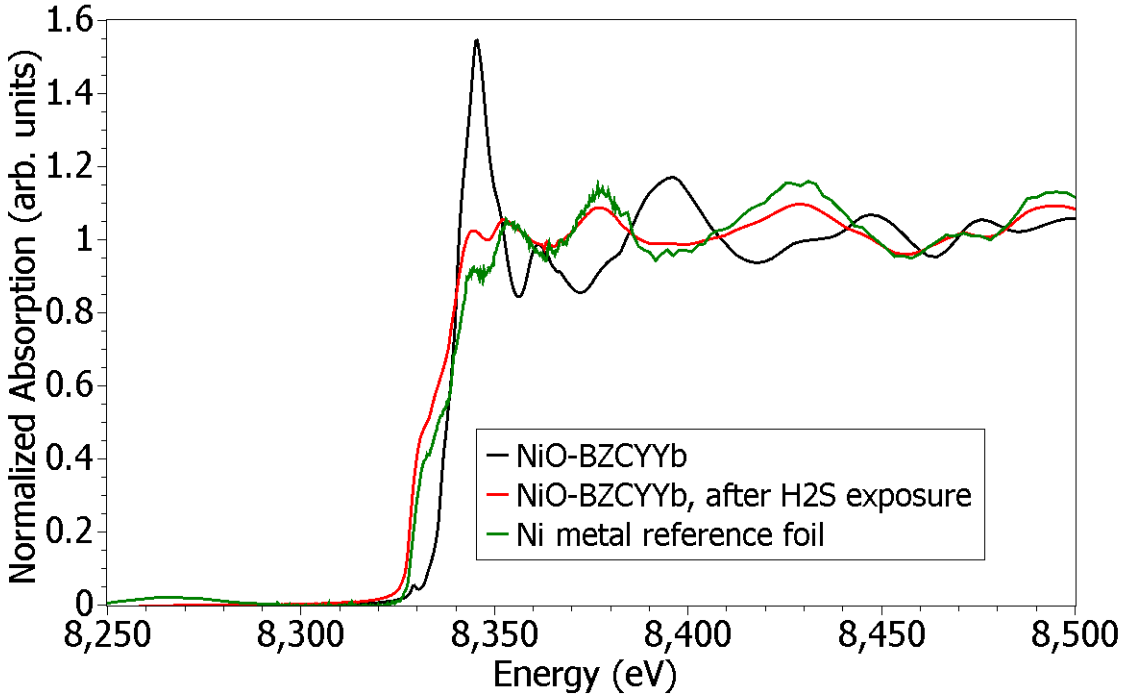

Figure 38: Ni K-edge XANES of NiO-BZCYYb before and after reduction in 100 ppm of H_2S in H_2, measured *ex situ*.

6.2 Ex situ *XAS*

6.2.1 Ni K-edge in NiO-BZCYYb before and after sulfur exposure

The Ni atoms were observed to be affected both in oxidation state and local structure. First, in as-prepared NiO-BZCYYb, the Ni K-edge is located at 8339.5 eV, as seen in Figure 38 which is representative of the NiO that was mixed into the BZCYYb during synthesis. As expected, exposure to H_2S at high temperature resulted in reducing NiO to Ni metal, as evidenced by the edge shift to 8333 eV, the Ni K-edge. Comparison of the spectrum with that of the Ni metal reference foil indicates in strong agreement. Thus, Ni metal is detected as present in the H_2-exposed NiO-BZCYYb and NiO-BZCYYb is further confirmed to preserve the Ni metal from sulfur poisoning.

In the FT-EXAFS of the Ni K-edge, depicted in Figure 39, some expected differences in the local structures of Ni metal and NiO are readily observed. The FT-EXAFS of the as-prepared NiO-BZCYYb features two prominent features at 1.60 Å

and 2.55 Å. Given that NiO was mixed in the as-prepared NiO-BZCYYb, the two features should correspond to the Ni-O and Ni-O-Ni bonds, respectively. The FT-EXAFS of the Ni metal reference foil has two features located at a shorter radial distance of 1.47 Å for the first feature and a much shorter radial distance of 2.09 Å for the second feature. In this case, the first feature is similar to the radial distance for the Ni-O bond so the Ni metal reference foil appears to contain some amount of NiO. However, the second feature is about 0.46 Å shorter and represents the Ni-Ni metal bond. For the H_2-exposed NiO-BZCYYb, there is only one prominent feature at 2.15 Å, which is similar to the second feature of the Ni metal reference foil. Given that the edge energy and shape of Ni in H_2-exposed NiO-BZCYYb strongly resembles that of the Ni metal reference foil, the conclusion made is that the Ni in H_2-exposed NiO-BZCYYb is primarily of a metallic nature. The lack of a peak for the Ni-O bond indicates that the sample was well-sealed after H_2 exposure and during the transit time between exposure treatment and characterization. Features above a radial distance of 3 Å are more difficult to assign specific coordination bonds without computational fitting because of contributions from multiple scattering paths. In conclusion, after reduction at high temperature, the Ni remains stable in metallic form under H_2 exposure both in its electronic state and its local structure.

6.2.2 Ba L-edge in NiO-BZCYYb and BZCYYb

The results in Figure 40 indicate that Ba in both BZCYYb and NiO-BZCYYb has no significant changes in edge energy after exposure to H_2, which suggests that the H_2 exposure did not permanently affect the oxidation state of Ba. However, with the addition of Ni, the intensity of the white line is greater and slight more so after H_2 exposure. The increase in the white line intensity represents an increase in the density of unoccupied states. In the corresponding FT-EXAFS in Figure 41, there is a corresponding increase in the magnitude of coordination at 2.15 Å and 3.50 Å. These

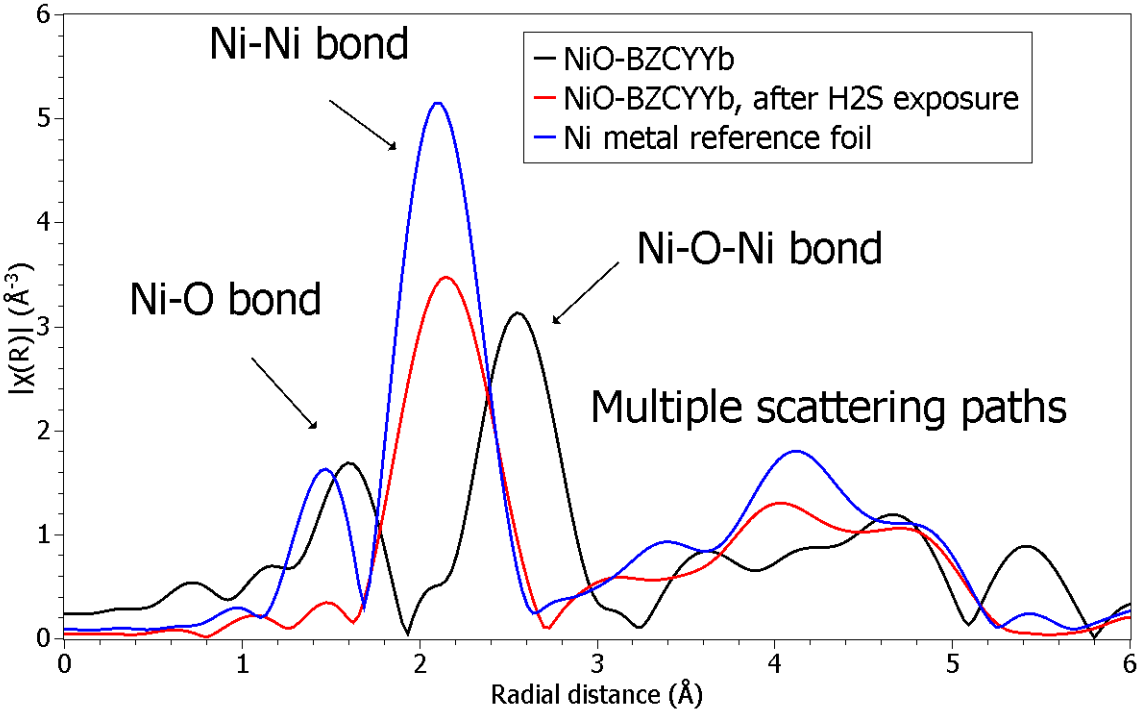

Figure 39: Ni K-edge FT EXAFS of NiO-BZCYYb before and after reduction in 100 ppm of H_2S in H_2, measured *ex situ*.

two radial distances are tentatively assigned to the coordination of B-site atoms (Zr, Ce, Y, and Yb) and neighboring A-site atoms (Ba). The combination of increased density of unoccupied states and increased coordination indicate that the bonding of the Ba atom with neighboring cations becomes slightly more regular with the introduction of NiO and subsequent reduction to Ni metal. Overall, the Ba oxidation state and local structure are stable and resistant to adverse reactions in the bulk caused by H_2S exposure.

6.2.3 Y L-edge in NiO-BZCYYb and BZCYYb

From the spectra in Figure 42, there appear to be no significant differences in the edge shape or energy in the Y L-edge of as-prepared and H_2-exposed NiO-BZCYYb and BZCYYb. In the FT-EXAFS of the Y L-edge, there are some minute variations in the local structure of as-prepared NiO-BZCYYb but the local structure Y atoms in H_2-exposed NiO-BZCYYb is largely the same as that in as-prepared BZCYYb and

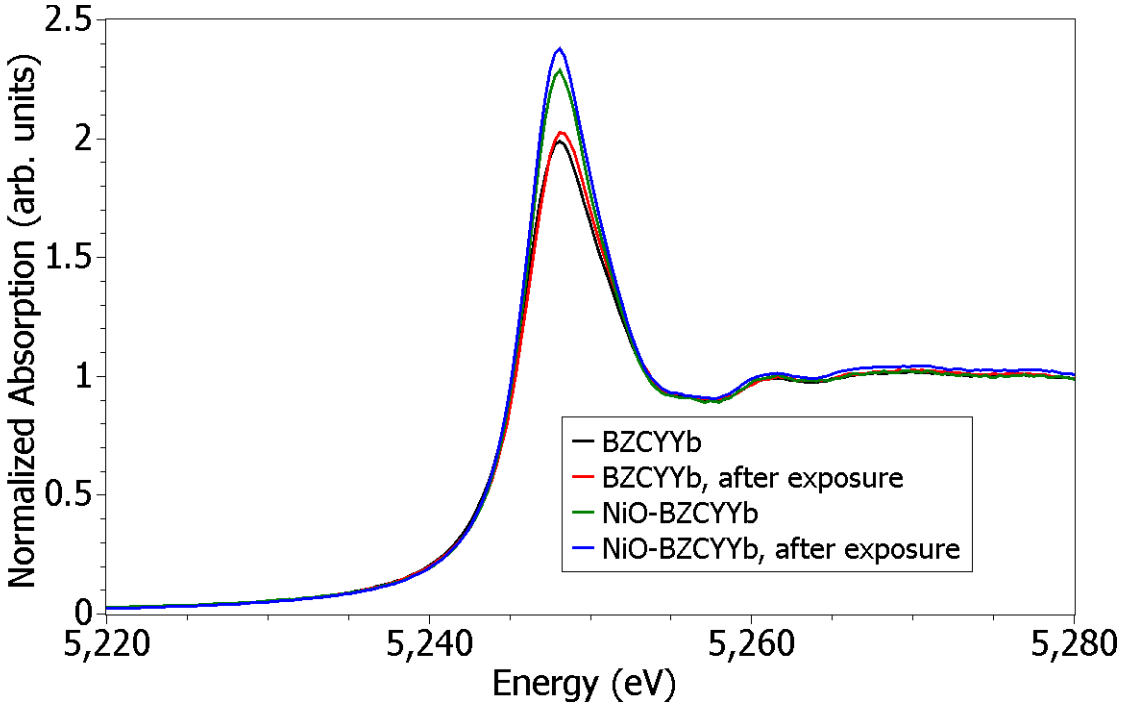

Figure 40: Ba L_3-edge XANES of BZCYYb and NiO-BZCYYb before and after reduction in 100 ppm of H_2S in H_2, measured *ex situ*.

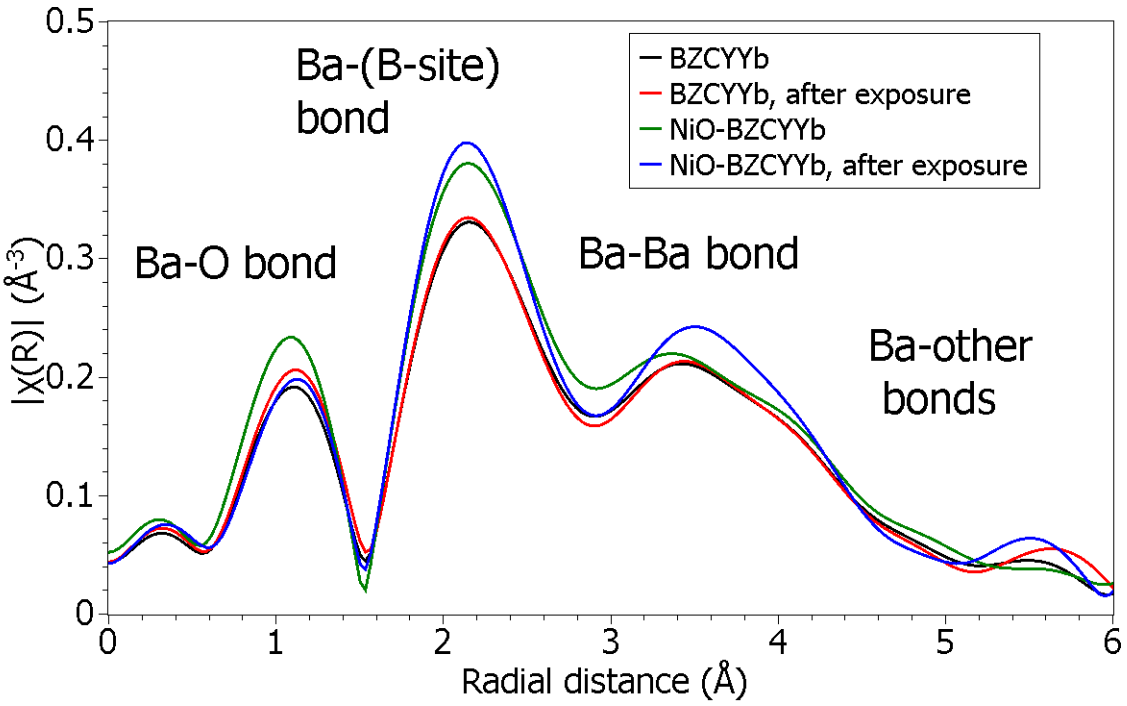

Figure 41: Ba L_3-edge FT EXAFS of BZCYYb and NiO-BZCYYb before and after reduction in 100 ppm of H_2S in H_2, measured *ex situ*.

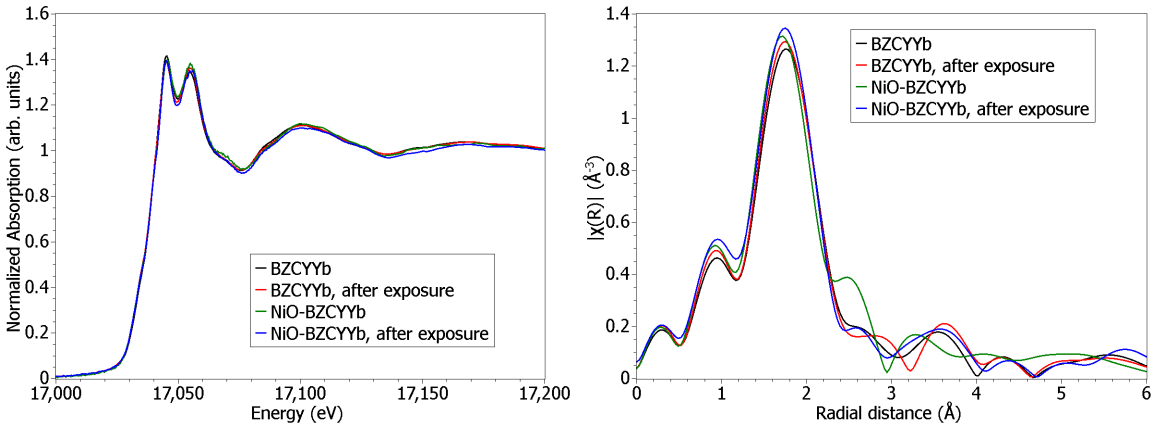

Figure 42: Y L_3-edge XANES (left) and FT EXAFS (right) of BZCYYb and NiO-BZCYYb before and after reduction in 100 ppm of H_2S in H_2, measured *ex situ*.

H_2-exposed BZCYYb. Thus, the Y atoms are unaffected by the exposure to H_2S.

6.2.4 Yb L-edge in BZCYYb

From the Yb L-edge in BZCYYb before and after hydrogen sulfide exposure, shown in Figure 43, the edge energy and near-edge structure are nearly the same. In the sulfur-exposed case, the white line is slightly larger, meaning that there is a slightly higher density of unoccupied states.

Also in Figure 43 is the FT EXAFS, where there is a very short but distinct elongation of 0.03 Å in the distance to the first coordination shell of the Yb atom. The elongation in the distance to the first coordination shell may be the result of a slight distortion in the octahedral coordination. The magnitude of elongation observed is too small to correspond to the larger ionic radius of a sulfur atom. Thus, it is unlikely that there is any sulfur permanently attached to the Yb atom. In general, the Yb was mostly unaffected by the exposure to H_2S.

6.3 In situ *XAS*

Both Ni K-edge and Yb L-edge XAS were collected at the same beamline and showed somewhat interesting phenomena in both the XANES and EXAFS regions.

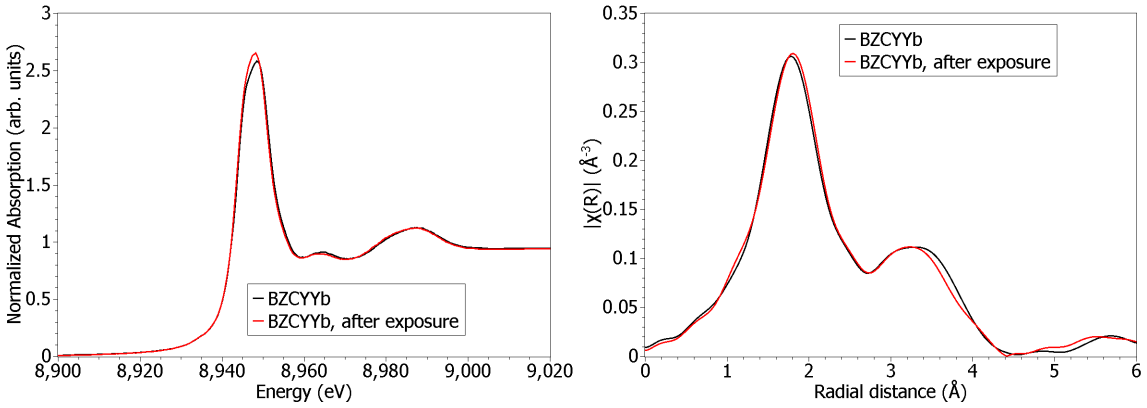

Figure 43: Yb L_3-edge XANES (left) and FT EXAFS (right) of BZCYYb before and after reduction in 100 ppm of H_2S in H_2, measured *ex situ*. The Yb in NiO-BZCYYb could not be measured in fluorescence mode because of an overlap in energy of the Ni fluorescence with the Yb fluorescence.

6.3.1 Ni K-edge XAS

Initially, in Figure 44 the Ni K-edge XANES of the patterned Ni on BZCYYb showed a metallic nature, characterized by how it exhibited the same edge features as the Ni metal reference spectrum. Due to the thin nature of the sputtered Ni patterned electrodes, the post-edge oscillations diverge from the Ni metal reference whose bulk is the FCC crystal structure. Upon heating to 300 °C, 500 °C, and 700 °C, a gradual change in the edge shape is observed until the spectra closely matches the NiO reference spectrum. This occurs despite the sample being heated in the presence of 5 % H_2 in He, which should be a reducing gas. There are two plausible potential sources of oxygen that could be causing this "oxidation": first, the *in situ* cell environment may be leaking in oxygen from the surrounding air and second, the oxygen in the BZCYYb electrolyte substrate may be mobilized at higher temperatures because of a non-equilibrium stoichiometry and oxidizing the Ni. Assuming that the flow rate of the reducing blanket gas is greater than the leaking rate of oxygen in an *in situ* cell with a small dead volume, it seems probable that the second option is the cause of the oxidation. As is characteristic of oxidation, the edge is shifted to higher energies and

the edge peak intensifies, which represents the increased density of unoccupied states that core electrons can be promoted into since the Ni atoms have become cationic relative to the metallic state.

Upon introducing hydrogen sulfide to the sample at 700 °C, a slight oxidative shift is observed, accompanied by an increase in edge peak intensity, as depicted in Figure 45. This phenomenon suggests that the sulfur anion is reacting with the nickel, which is the expected sulfur poisoning mechanism, and may even point to the nickel having preferential reactivity with sulfur anions over oxygen anions.

Upon cooling from 700 °C to 25 °C in the presence of H_2S, the Ni K-edge remains relatively unchanged before experiencing an energy shift to lower energy (Figure 46), indicative of a slight reduction but still retaining the edge peak shape of cationic nickel. Although NiS formation would be expected here, the edge shape does not resemble the NiS reference spectrum. However, the edge energy after cooling down does match the NiO reference. Thus, overall, the presence of H_2S appears to cause Ni atoms to become more cationic when at elevated temperatures.

Analysis of the Fourier transformed (FT) EXAFS supports some of the conclusions made by the XANES analysis. Firstly, when the 25 °C spectrum is compared to the Ni metal reference foil in Figure 47, a close match in the location of the peak at about 2.2 Å confirms the initial metallic local structure. As a reminder, the radial distances in the FT EXAFS are not phase corrected and thus may deviate from true atom-atom radial distances by roughly 0.3 Å to 0.5 Å. After heating, the FT EXAFS exhibits a spectrum profile that bears resemblance to the NiO reference FT EXAFS, such as the appearance of two peaks between 1.0 Å to 2.0 Å and an elongation of the 2.2 Å radial pair. A broadening of the peaks is also expected, as the high temperature increases the Debye-Waller factor. However, switching to the H_2S, the FT EXAFS closely matches the NiO reference, even as far 6.0 Å in the multiple scattering paths regime. This suggests that the NiS formed *in situ* appears to adopt the simple cubic local

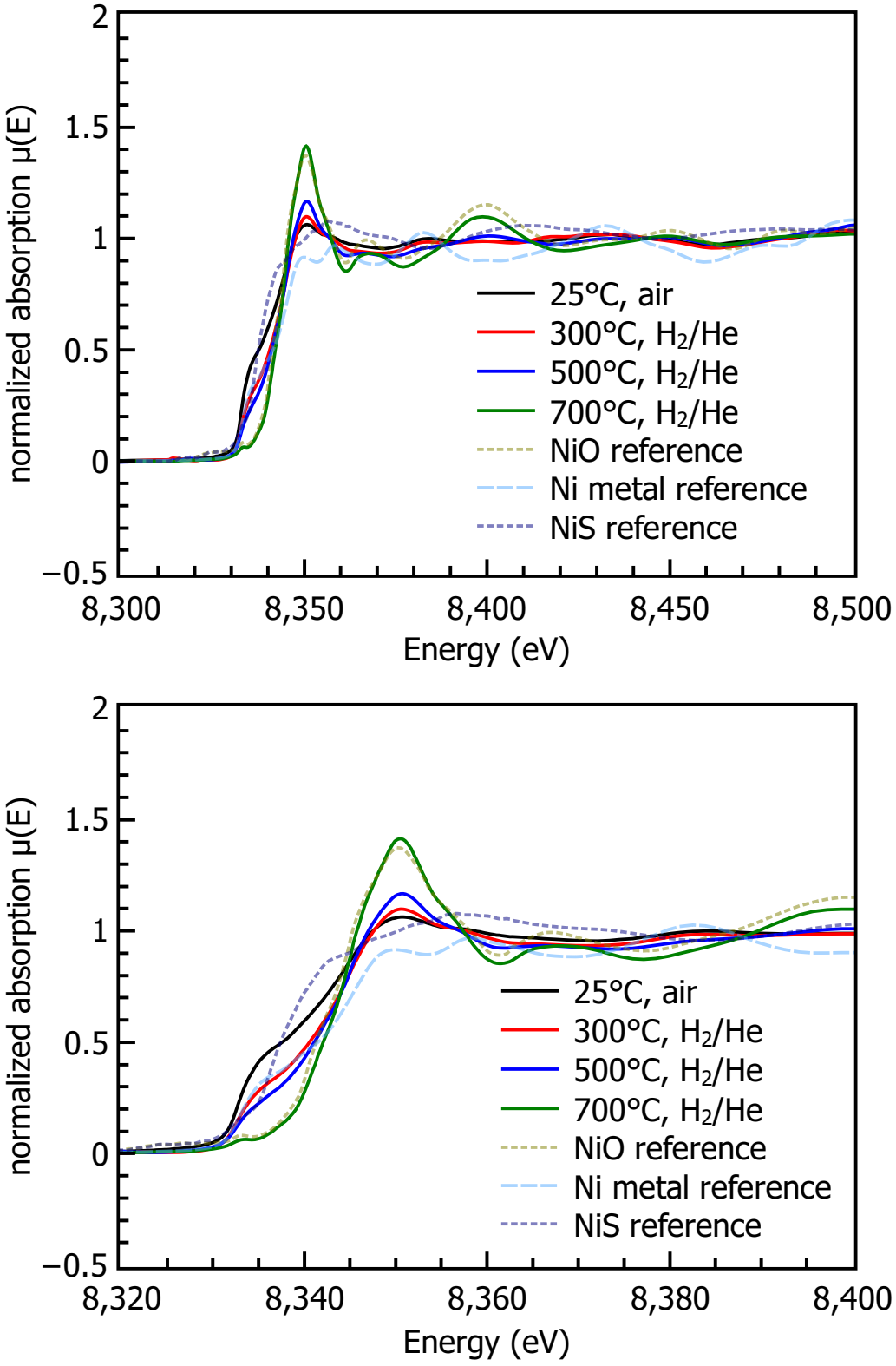

Figure 44: The XANES region of the Ni K-edge XAS (left) and a close-up view (right) to show the edge shifts.

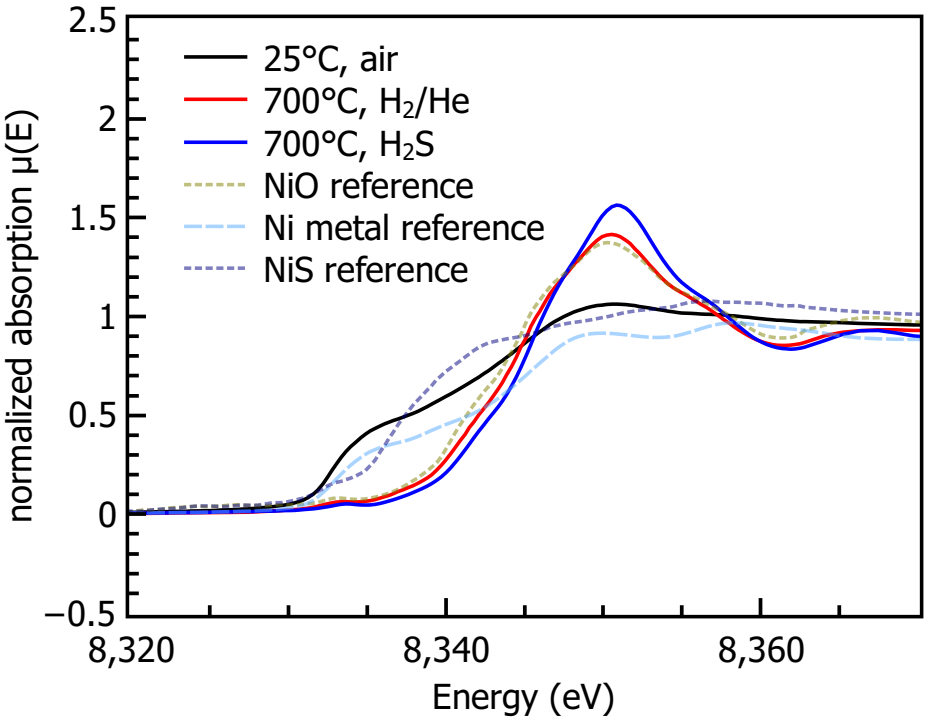

Figure 45: The XANES region of the Ni K-edge XAS after introducing H_2S at high temperature.

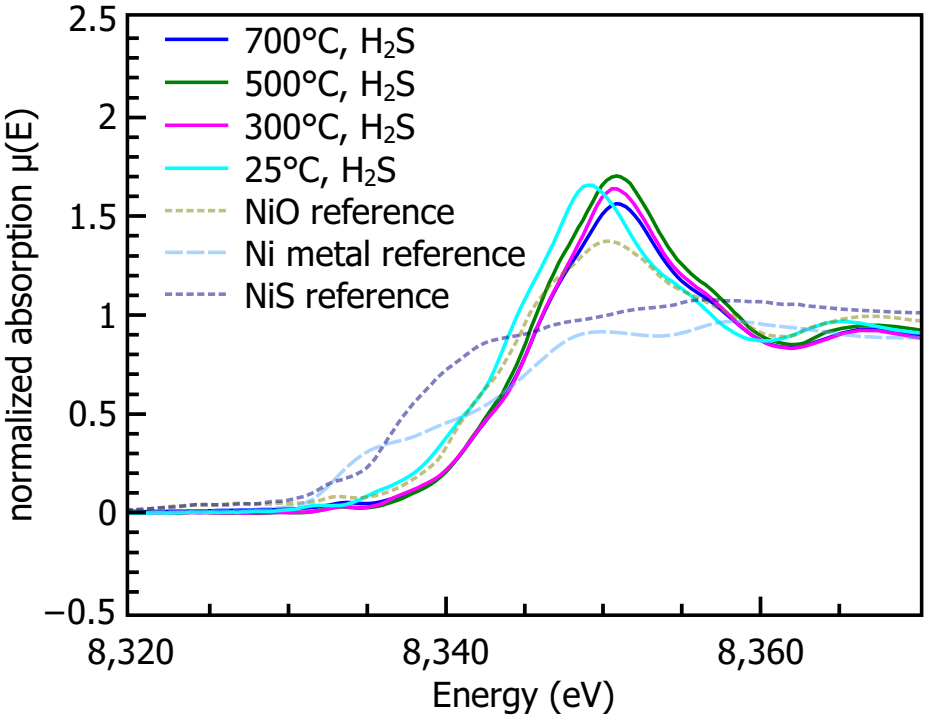

Figure 46: The XANES region of the Ni K-edge XAS after cooling down under H_2S.

structure of the NiO and why it does not match the NiS reference sample, which would nominally have a hexagonal crystal structure. Also in Figure 47 is the FT EXAFS after cooling to room temperature under H_2S. As with the FT EXAFS at 700 °C, it also shows similarity to the NiO reference material, but with two distinctions. First, the relative peak intensities of the 1.0 Å to 2.0 Å are imbalanced. Typically, a splitting of the first peak would suggest distortion of the local structure so that some oxygen anions are closer or farther away from the metal absorber atom instead of all the nearest neighbors being equidistant. Secondly, all of the peaks in the room temperature FT EXAFS show a consistent shift to slightly longer distances. This could suggest the infiltration of sulfur anions into the cationic Ni matrix, which would imply that the previous data represent a NiO matrix.

For the sake of transparency, k-space post-edge fine structure are shown in Figure 48 to point to the origin of the difference in FT EXAFS observed between the metallic state of Ni and the high temperature state before and after sulfidization.

Data from the intermediate temperatures during heating and cooling under 5 % H_2 in He and under H_2S either did not have clear trends or were omitted for clarity in the figures. The Ni K-edge FT EXAFS for intermediate temperatures (Figures 70) can be found in the Appendix. Additional figures showcasing the k-space of the Ni K-edge XAS (Figure 71) are also located in the Appendix.

6.3.2 Yb K-edge XAS

The Yb L_3-edge is roughly 600 eV above the Ni K-edge, which made collection of the data both convenient and relevant to the understanding of BZCYYb. Yb is suspected to play an important role in the catalysis of sulfide ions and neutralizing their degradation of the Ni and/or the triple phase boundaries. From an initial glance, there did not appear to be a significant response in the Yb L_3-edge as was observed for the Ni K-edge. A close examination of the edge energies, as shown in Figure 49,

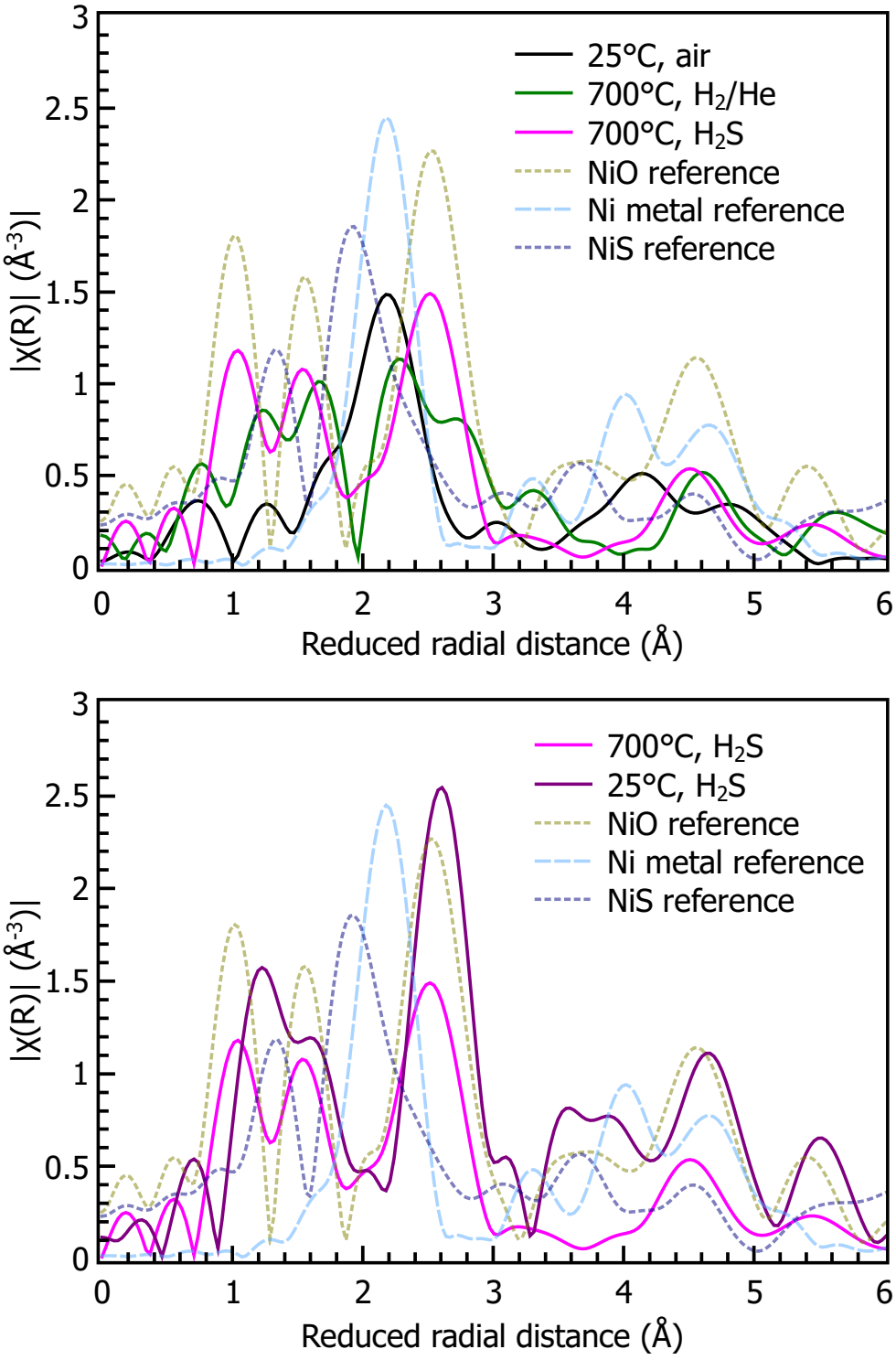

Figure 47: The Fourier transform of the Ni K-edge EXAFS at various temperatures and before and after exposure to H_2S.

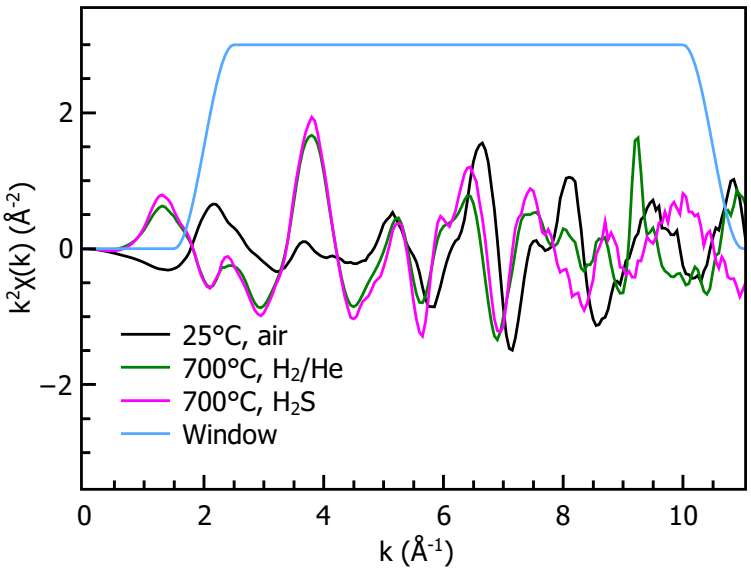

Figure 48: The Ni K-edge EXAFS in k-space before and after exposure to H_2S exposure showing the difference between the metallic state of the as-prepared sample at room temperature and the high temperature state. The window indicates the region for the Fourier transform.

does reveal subtle shifts. Primarily, a reduction edge shift is recorded at 700 °C. If this is inferred to be a loss of local oxygen anions from the high temperature and low oxygen partial pressure affecting the oxygen stoichiometry, it complements the Ni oxidation discussed earlier.

When the H_2S is introduced, there is little change in the edge shape or energy, aside from a small increase in peak intensity. The intensity continues to vary without a consistent trend as the temperature decreases. Eventually, after cooling down to room temperature, the edge energy is observed to take an oxidative shift and nearly return to the initial edge energy. However, from this information, it cannot be determined without doubt whether oxygen or sulfur anions caused the oxidation, unless the presence of oxygen in the *in situ* cell is assumed to be low enough to be a non-factor.

More information about the Yb cation can be extracted from the FT EXAFS. In the as-prepared sample, the Yb cation has a strong local coordination with oxygen, as shown by the prominent, singular peak of the FT EXAFS between 1.0 Å to 2.0 Å.

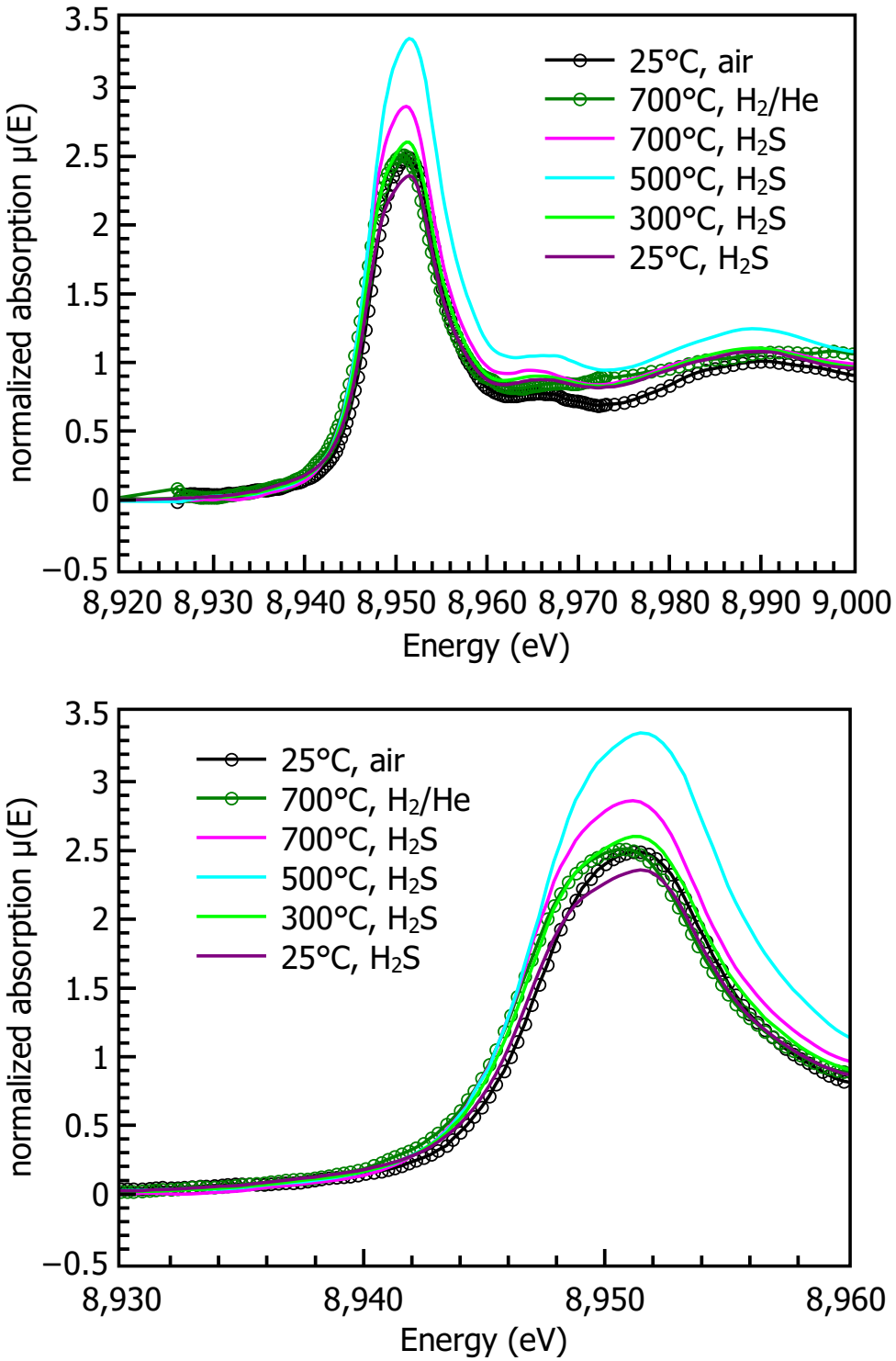

Figure 49: The Yb L_3-edge XANES and a close-up view of the near-edge region to show the edge shifts before and after exposure to H_2S.

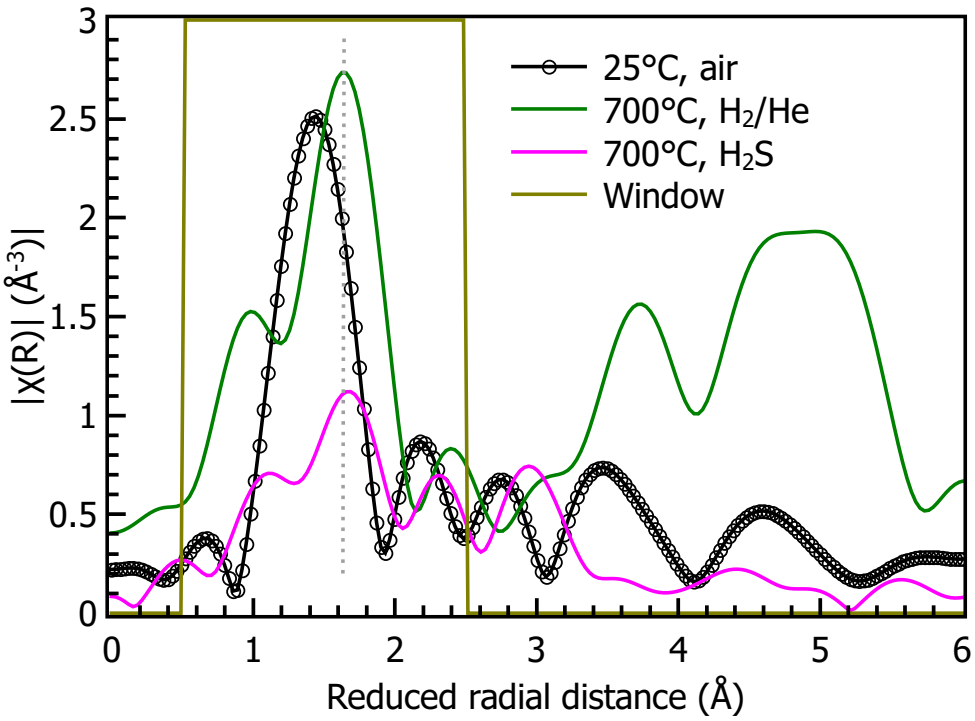

Figure 50: The Fourier transform of the Yb L_3-edge EXAFS at various temperatures and before and after exposure to H_2S. The window indicates the region for the backward Fourier transform.

At 700 °C, the first nearest neighbor shell shows a characteristic peak split likely associated with local oxygen vacancy formation. The loss of an oxygen anion can cause anisotropic deformation in the local coordination, causing a peak split to appear with differing amplitudes depending on their respective degeneracy. The peak split shape is preserved after introducing H_2S gas and as the dotted vertical guide line shows in Figure 50, the positions of both split peaks are shifted to higher R. Again, this could be attributed to the slightly larger radius of the sulfide ion (Pauling ionic radius of 184 pm vs. oxide ion's 140 pm) [80], assuming Yb-S bond formation. It should be noted that the high peak magnitudes observed in the multiple-scattering regime for the 700 °C FT EXAFS is largely due to high frequency noise in the k-space.

Figure 51 continues the data progression with the Yb FT EXAFS at lower temperatures while under H_2S. Although the trends are not exactly clear, the split peak

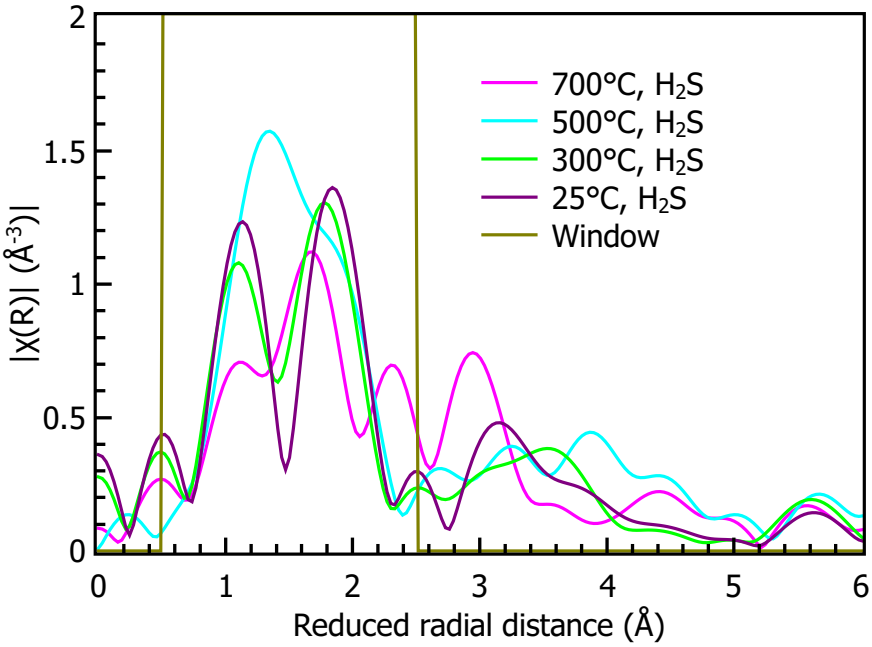

Figure 51: The Fourier transform of the Yb L_3-edge EXAFS at various temperatures after exposure to H_2S, which shows peak evolution. The window indicates the region for the backward Fourier transform.

shape persists and gradually becomes more defined after cooling to room temperature under H_2S. While the FT EXAFS at 500 °C does appear to have a different ratio of peak amplitudes, it should be noted that the total width of the peak is nearly the same as the lower temperature FT EXAFS spectra. Another interesting trend is the split peaks exhibit different correlations between temperature and reduced radial distance. For the peak at 1.2 Å, the R-position remains the same as the temperature decreases. The peak shape sharpens as the lower temperatures reduce the Debye-Waller factor. However, for the second peak, beginning at 1.7 Å, the R-position of the peak increases gradually but consistently to 1.9 Å as the temperature decreases. In a normal sixfold octahedral coordination of a B-site cation in a perovskite, a compression or elongation of ligands along one axis should conversely induce an elongation or compression, respectively, in the orthogonal plane. However, it could be speculated that if the octahedral coordination was mixed between oxygen and sulfur anions, substitution of one over the other could result in the phenomenon observed here, where the R-positions

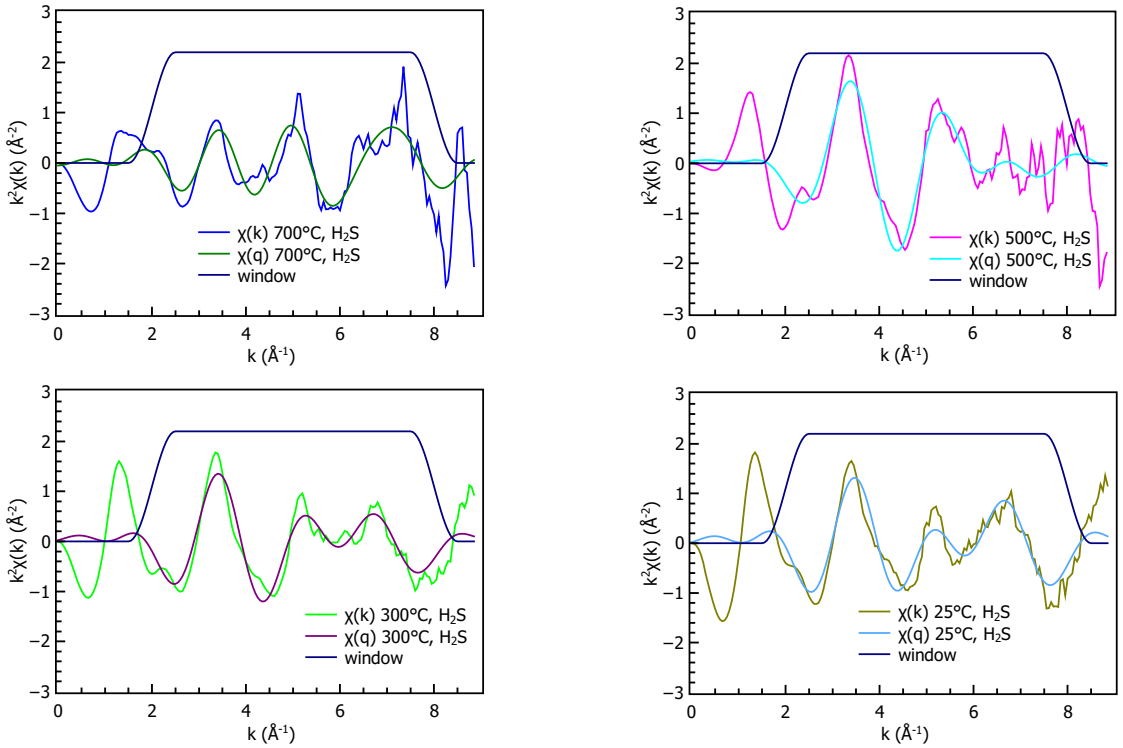

Figure 52: Backward Fourier transforms (labeled $\chi(q)$) from 0.5 Å to 2.5 Å of the $\chi(R)$ function show good agreement with the experimental $\chi(k)$ data. The window indicates the region for the forward Fourier transform of $chi(k)$.

of the split peaks appear to be unlinked.

Because of the lower signal-to-noise ratio of the Yb L_3-edge data collection, the backward Fourier transform of the nearest neighbor split peaks was examined to evaluate the trustworthiness of the data upon which these interpretations were based. By using a window of 0.5 Å to 2.5 Å, it can be seen in Figure 52 that most of the backward Fourier transforms (labeled $\chi(q)$) show good agreement with the experimental k-space data and that most of the signal in the k-space contributes to the peak shape characteristics in the first nearest neighbor shell.

6.4 In situ *XRD of NiO*

With the extremely fast acquisition time of the x-ray diffraction patterns at Beamline X7B, several *in situ* experiments were performed. However, before engaging in lengthy

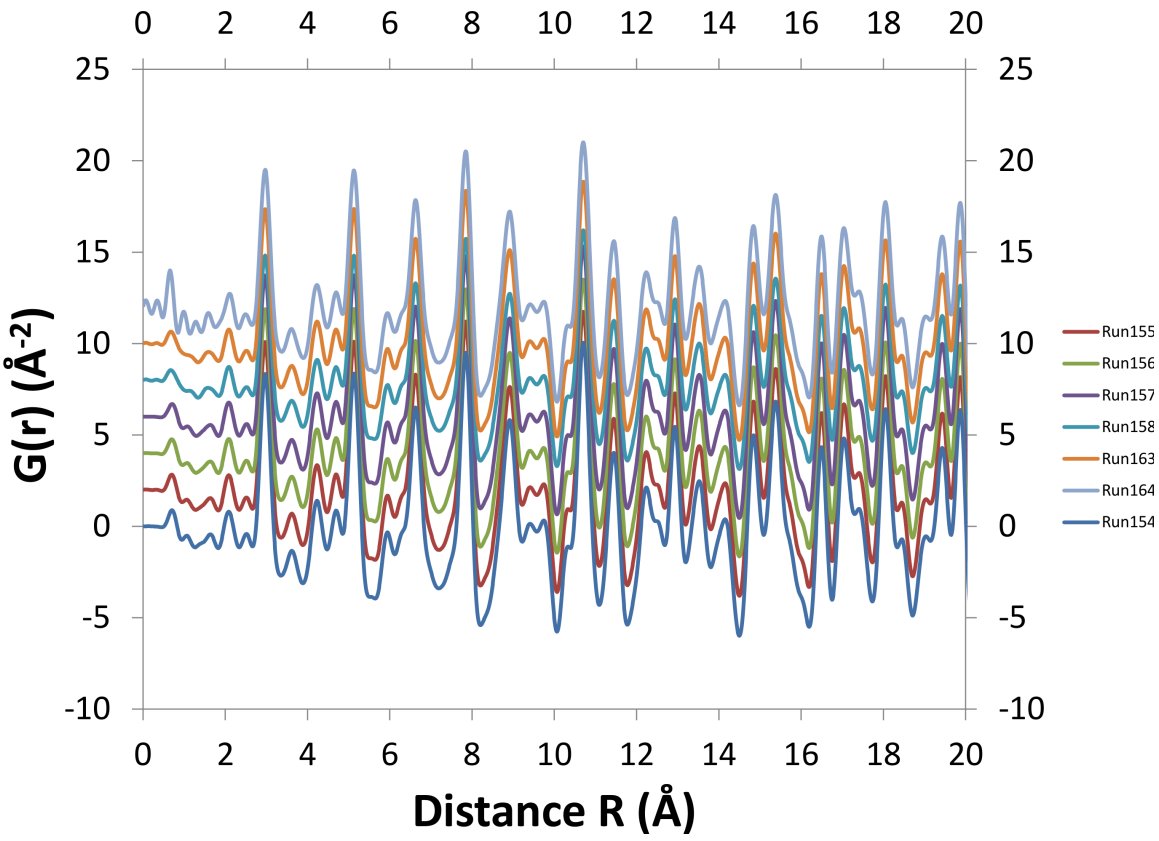

Figure 53: High numbers of exposures did not show any signs of change in the data due to radiation damage, if any, after hours of x-ray beam exposure.

experiments where a small amount of sample would be repeatedly exposed to a high intensity of high energy x-rays (38.86 eV), a preliminary test for x-ray damage was performed. Based on the reduced pair distribution function known as $G(r)$ shown in Figure 53, there does not appear to any significant change to the local structure, which would be the most sensitive to irregularities caused by radiation damage. Each of the seven runs consisted of 450 4 s-exposures, amounting in 30 min of cumulative exposure time for each run. Compare to a normal data acquisition method, which would consist of 5 4 s-exposures or just 20 s of cumulative x-ray exposure. To correctly measure each exposure, the dark current exposure of an equal amount of time must be collected before each x-ray beam exposure.

In Figure 54, a series of *in situ* XRD patterns of NiO are plotted in a stack with small vertical offsets. Beginning from the bottom scan at room temperature, each

scan corresponds to roughly a 10 °C increase in temperature. The pattern colored red indicates when the sample reached 750 °C and the gas connection was modified to introduce H_2S while the purge gas (5 % H_2 in He) was reduced in flowrate to 5 mL min^{-1}. During cooling, each scan likewise corresponds roughly to a 10 °C difference. The initial phase is pure nickel oxide. There is a small broad peak at roughly 20° 2θ which is most likely from the quartz glass sample holder. Upon reaching a temperature of 540 °C during cooling, a new phase was observed to form, which remained until the sample cooled to room temperature. The two new peaks from the new phase, at 51.5° and 92.5°, can be matched to nickel metal, which formed from the reducing gas environment. It is difficult to draw definite conclusions from this result. One possibility is that there may have been insufficient H_2S generated from the FeS reacting with HCl, which explains why Ni metal remains during the cool down phase. However, this seems unlikely given the active bubble formation observed from the reaction. It seems that the NiO was not significantly reduced by the flowing hydrogen. Another possibility is that the H_2S only caused a reaction on only the surface of the Ni and of insufficient thickness to form diffracting crystal planes. Lastly, an experimental error may be that a longer purge time might be needed for the oxygen in the gas system to be completely removed.

The effect of temperature on the diffraction patterns is subtle but consistent. The change in temperature is responsible for the contraction and expansion of the diffraction patterns, which is caused by the thermal expansion of the crystal structure. Since the d-spacing between crystal planes increases as the temperature increases (or vice versa) and the wavelength is fixed, the 2θ angle of a peak must decrease in order to compensate according to Bragg's Law. When many diffraction patterns of different temperatures are plotted, the contraction and expansion appear as a crescent or "boomerang" shape as the 2θ position of the peaks shifts accordingly.

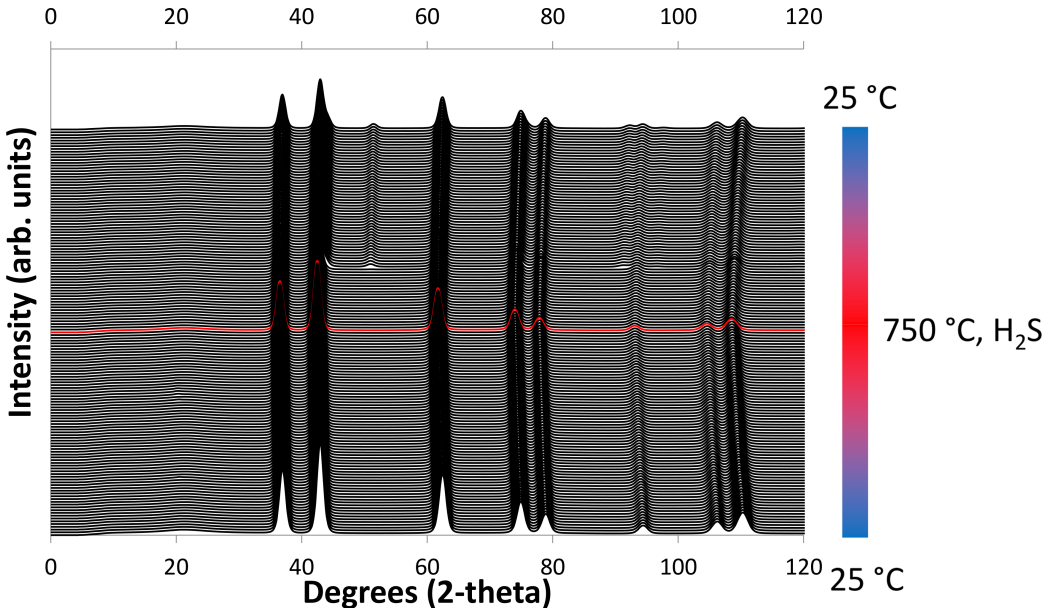

Figure 54: XRD patterns of NiO measured *in situ* at temperatures from room temperature to 750 °C and under 5 % H_2 in He. The pattern marked in red indicates when the temperature reached at 750 °C and H_2S exposure began.

6.5 In situ *PDF of NiO*

The *in situ* reduced PDF data are shown in Figure 55. However, at a first glance, the reduced PDF appears relatively unchanged since most of the interesting phenomena are not easily detectable, partly because the scaling of the data when using many vertical offsets tends to dampen the magnitude of the peaks and troughs. The most significant difference is marked by a green arrow at roughly 2.50 Å.

To more clearly see the difference, the first and last PDF scans of the NiO sample are plotted in direct comparison without offset in Figure 56. The green arrow marks the same peak transition from Figure 55. This feature at 2.50 Å arises at roughly 540 °C and the radial distance matches the distance of a Ni-Ni metal pair from the EXAFS data (2.2 Å) on the Ni metal reference, if the phase shift is accounted for and estimated at 0.3 Å. Thus, the Ni metal formation seen in *in situ* XRD is confirmed with PDF.

An even closer examination of the short-range order is necessary, since the scaling

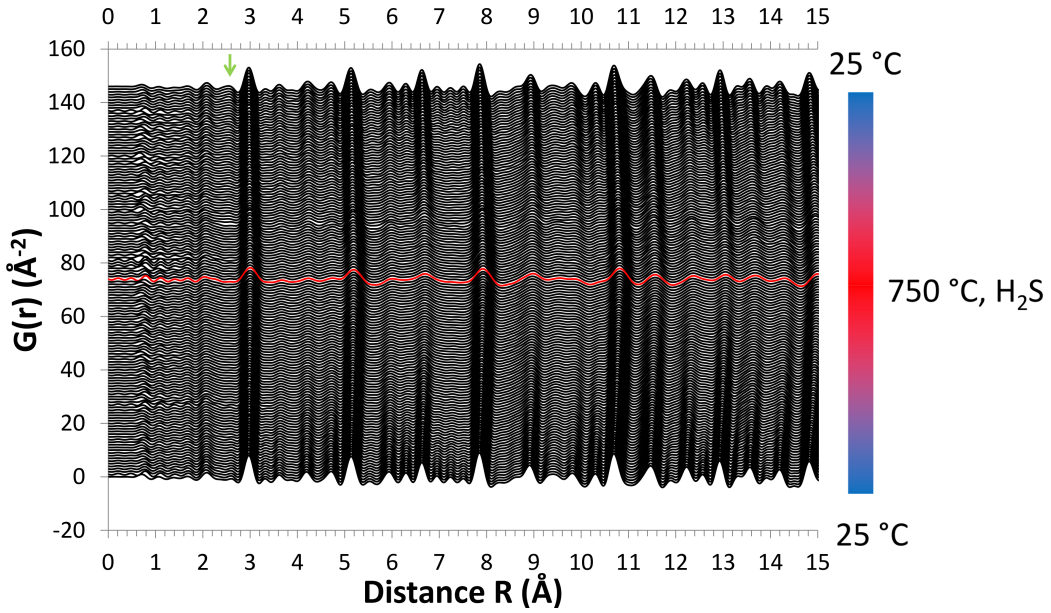

Figure 55: Overview of the reduced PDFs of NiO measured *in situ* at temperatures from room temperature to 750 °C and under 5 % H_2 in He. The pattern marked in red indicates when the temperature reached at 750 °C and H_2S exposure began. Data were derived from the same measurements as the *in situ* XRD in Figure 54. X-axis is adjusted for clarity.

in Figure 55 makes it difficult to capture the nuances. For example, at just below 1.0 Å, there appears to uneven noise in the reduced PDFs, which seems to become more severe after the introduction of H_2S (red scan). Figure 57 shows a few select reduced PDFs in that short-range distance, where each scan represents a 10 °C difference, beginning at 690 °C and cooling to 660 °C under 5 % H_2 in He with H_2S introduced.

In the region of 0.5 Å to 1.0 Å, the progression of the reduced PDFs in order of temperature are traced in orange double line arrows, labeled 1, 2, and 3. In the same order, the peak position shifts from 0.80 Å to 0.68 Å to 0.77 Å to 0.72 Å. Thus, there appears to be an oscillation in the peak position before settling in a middle position at 660 °C. From the context of all the data seen in Figure 55, these oscillations appear to be recurring without a overall trend toward one peak position or another. These oscillations are also too large in magnitude to be solely explained by

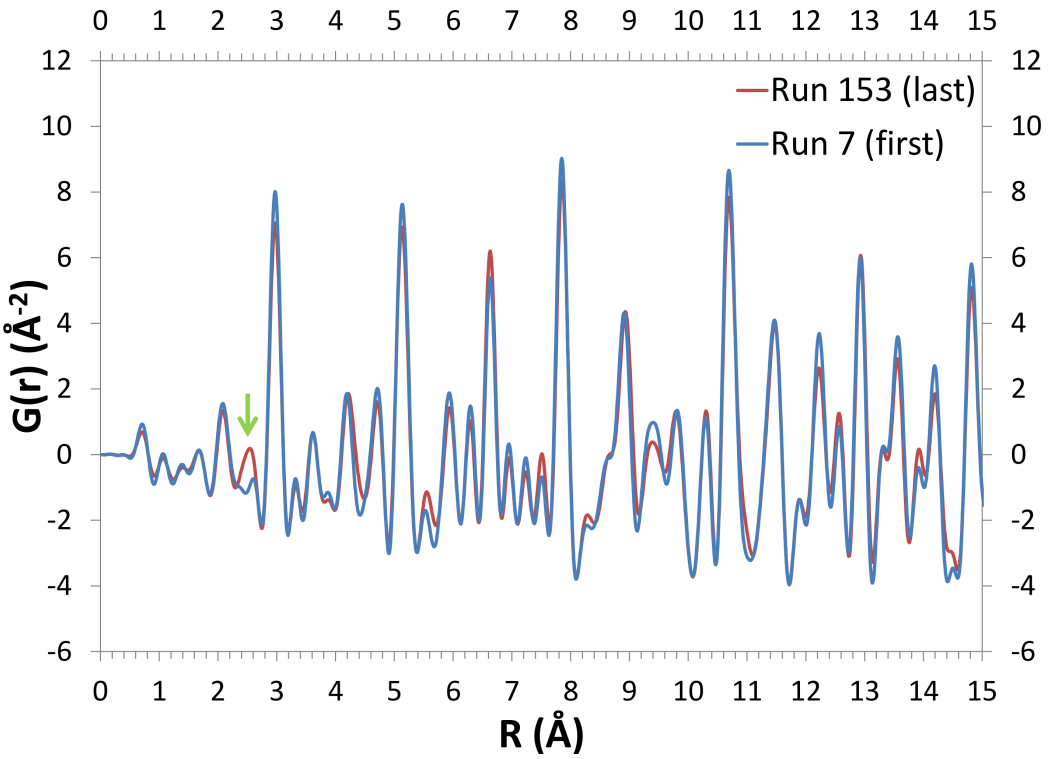

Figure 56: Comparison of the reduced PDFs of NiO measured at the beginning and the end of the experiment with a green arrow indicating the most significant difference in the short-range order. The distance roughly corresponds to the Ni-Ni metal pair distance determined by EXAFS, including the phase shift. X-axis is adjusted for clarity.

thermal expansion. Instead, there seem to be occasional oscillations throughout the experiment, although it could be argued that these oscillations appear more frequently and with greater magnitude after the introduction of H_2S. The four chosen reduced PDFs also appear to share a common point of intersection at 0.73 Å, akin to an isosbestic point. The presence of an isosbestic point suggests that a single, first-order reaction causing the peak shift and that the two species that generate each peak are stoichiometrically fixed along a linear relationship. Along a similar line of observation of the possible isosbestic point, it is interesting to note the shared nodes and anti-nodes, although the peaks in the region below 0.5 Å do not represent physical coordinated pairs except possibly gaseous molecules. To further add to the analysis, corelated peak formation and destruction is observed at 2.59 Å where a peak is located in the NiO reduced PDF. The reduced PDFs at 690 °C and 670 °C tend to resemble NiO at that distance while the reduced PDF at 680 °C has no peak at that distance. As before, the reduced PDF at 660 °C appears as an intermediate mix of the two.

Based on these observations, it is *speculated* that the two peaks represent oxygen and sulfur anions exchanging as coordinated on the same Ni cations. Since the peak position oscillates, the reaction would be oscillating between bonding between oxygen and sulfur anions. Reduced PDFs at 690 °C and 670 °C tend to exhibit longer coordinated pair distances than those found at 660 °C and in NiO at room temperature, which could be attributed to the larger sulfur anion radius. However, if this Ni-S pair is unstable, perhaps if the gas stream is not homogeneous enough, and is cleaned off later by hydrogen gas, it may explain the oscillating behavior. Water vapor in the gas from bubbling the FeS/HCl solution may be causing the Ni to reoxidize, causing the peak at 2.59 Å to form again.

In order to correctly interpret peak shifts in radial distances, the thermal expansion effect must be considered carefully, since it will cause the peaks to shift to higher distances purely as a function of temperature. Based on measurements at different

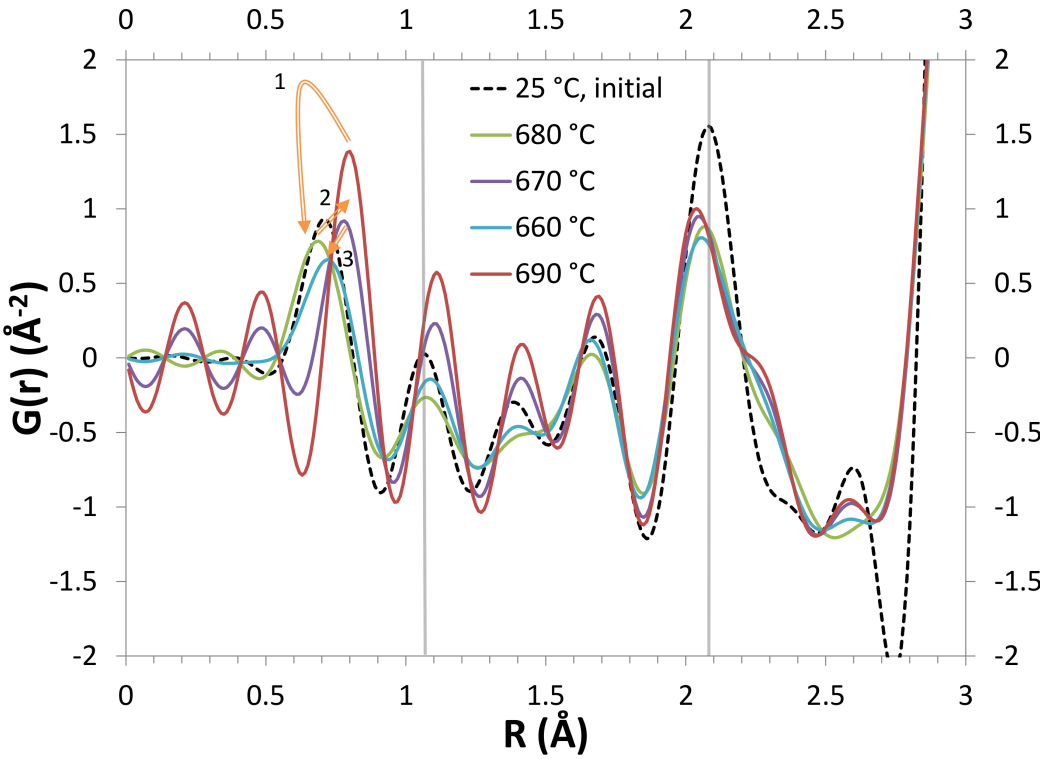

Figure 57: A closer view of the reduced PDF of NiO ranging from 690 °C to 660 °C showing anomalous behavior of the peaks. Progression of runs is shown in order of the numbered orange double-line arrows. Gray guide lines at 1.06 Å and 2.08 Å show deviations from the room temperature reduced PDF (dotted black line). X-axis is adjusted for clarity.

distances, the thermal expansion effect at 690 °C is estimated to be about 1.1 % of the radial distance measured at room temperature. For example, the thermal expansion at the 2.97 Å, 10.68 Å, and 17.01 Å peaks were measured to be 0.03 Å, 0.11 Å, and 0.19 Å, respectively, by comparing the radial distances of that peak in the initial reduced PDF at room temperature to the same peak in the reduced PDF at 690 °C.

The first guide line at 1.06 Å in Figure 57 is drawn to show that thermal expansion effects are insufficient in explaining the peak shift to longer coordinated pair lengths, since all of the peaks in the reduced PDFs at high temperature are shifted consistently to longer distances compared to the initial reduced PDF peak. The most shifted peak is located at 1.10 Å, a difference of 0.04 Å when the thermal expansion at that distance would be expected to shift the peak by 0.01 Å. As a result, it is also speculated that this significant peak shift is further evidence of oxygen subsitution by sulfur is also occurring at this distance. This is plausible because as was observed in the *in situ* Ni K-edge EXAFS, it is likely that the nominally sixfold nearest neighbor coordination of the Ni is distorted, resulting in coordinated pairs of slightly different distances.

The second guide line at 2.08 Å is more anomalous and difficult to explain. In contrast to most peaks and the thermal expansion effect, the peaks at each temperature are shifted to shorter distances. The most plausible explanation seems to rely on attributing the loss in peak magnitude to the growing shoulder at 2.27 Å, which is close to, but not exactly at, the Ni-Ni metal bond observed at 2.50 Å marked by the green arrow in Figure 56.

6.6 In situ *XRD for BZCYYb*

The experiment for NiO was repeated with BZCYYb powder. As before, the first scan begins at the bottom at room temperature and each subsequent scan is roughly 10 °C higher than the previous scan until the diffraction pattern marked in red, which is when the temperature reached 750 °C and the H_2S-generating reaction was initiated.

The main phase of $BaCeO_3$, the parent structure of BZCYYb, is observed as indicated by the blue arrows in Figure 58. The second major initial phase, marked by green stars, was identified as a hexagonal phase, most likely barium carbonate ($BaCO_3$) formed with BZCYYb. The barium carbonate appears to undergo decomposition at high temperature as shown in the diffraction patterns just below the pattern plotted in red. Upon reaching a temperature of 560 °C during cooling under flowing H_2S, indications of barium oxide appeared, marked by the red triangles, and persisted as the sample continued to cool to room temperature. This is expected since it is the remaining decomposition product of the initial $BaCO_3$. Muted signals of another phase, $Ba(OH)_2 \bullet H_2O$ [53], also appeared (marked by purple diamonds), most likely due to BaO reacting with water vapor in the gas, which is humidified because it bubbles through water. There appear to be strong signals of $Ba(OH)_2 \bullet H_2O$ at high temperature after the $BaCO_3$ decomposes but which disappear immediately after the introduction of H_2S. This progression of phase changes suggests that the sulfur tolerance is water-mediated, similar to how barium oxide was shown to promote water-mediated removal of carbon [82].

6.7 In situ *PDF for BZCYYb*

The *in situ* reduced PDF for BZCYYb is much more complicated, owing to all of the dopants having slightly different ion sizes and thus, coordinated pair distances. Figure 59 makes it evident that the reduced PDFs are much more complicated and difficult to interpret, partly because the high intensity of a low R peak dampens the magnitude of the other peaks and partly because of the scaling from the vertical offsets. Although there are certain shifts in peak position along radial distance even to medium ranges, there are no clear and consistent overall trends. Even reducing the data in the figures to the heating and cooling halves of the experiment, shown in Figures 72 and 73 in the Appendix, was insufficient in clarifying any trends.

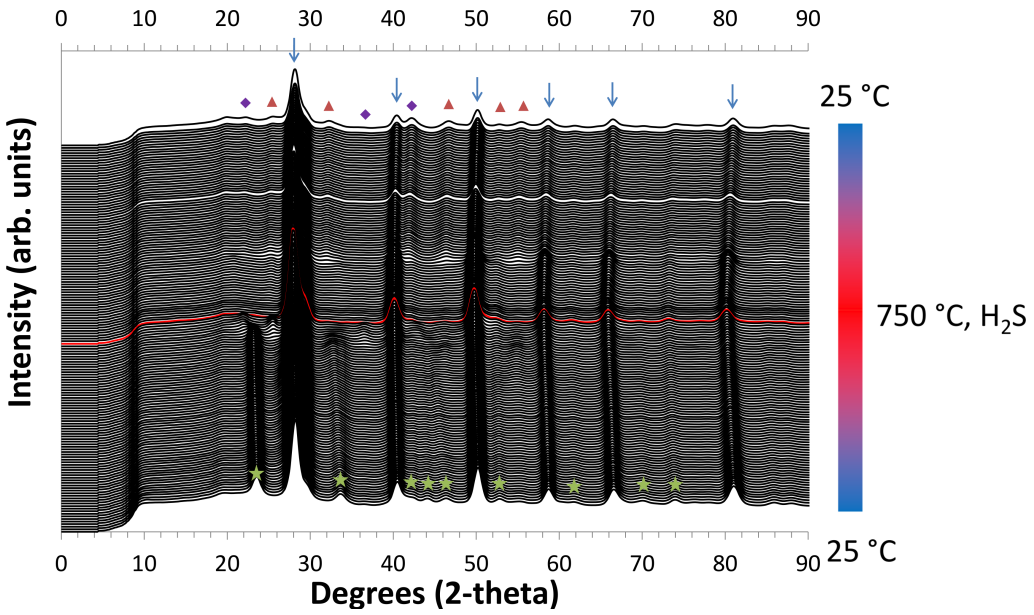

Figure 58: XRD patterns of BZCYYb measured *in situ* at temperatures from room temperature to 750 °C and under 5 % H_2 in He. The pattern marked in red indicates when the temperature reached at 750 °C and H_2S exposure began. The phases identified are $BaCO_3$ (green stars at bottom), BZCYYb (blue arrows), BaO_2 (red triangles), and $Ba(OH)_2 \bullet H_2O$ (purple diamonds).

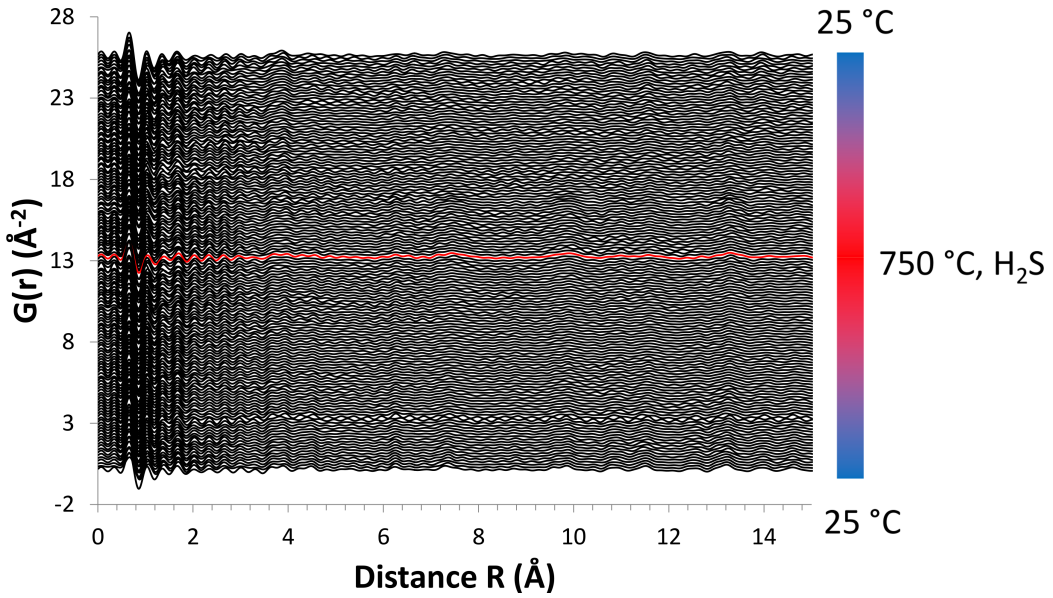

Figure 59: Overview of the reduced PDFs of BZCYYb measured *in situ* at temperatures from room temperature to 750 °C and under 5 % H_2 in He. The pattern marked in red indicates when the temperature reached at 750 °C and H_2S exposure began. Many medium-range features are dampened by the high magnitude short-range features. X-axis is adjusted for clarity.

To best analyze the data, a few reduced PDFs were chosen the most extreme conditions to observe the major differences. Figure 60 contains two reduced PDFs at 25 °C before and after the *in situ* experiment and two reduced PDFs at 750 °C after introducing H_2S for a shorter and longer period of time. The first clear observation is that a peak shift in radial position is observed for the reduced PDF at 750 °C after 20 min of exposure to H_2S which is not apparent in the first H_2S reduced PDF. This is likely a function of the long travel time in the tubes carrying the gas and the percolation of the gas through the small diameter of the quartz capillary tube holding the sample. Peak shifts that exceed the thermal expansion effect, or for which the thermal expansion effect can be neglected because of a common temperature, can be identified at 1.06 Å, 1.39 Å, and 1.69 Å before resulting in negative peak shifts at 2.02 Å and above. The short-range of these coordinated pairs once again suggest substitution of oxygen anions by sulfur anions, particularly as direct bonding pairs. At longer distances between 3.6 Å and 4.6 Å, the longer H_2S exposure imparts more defined structure based on the new peaks forming, which ultimately effects permanent change in the reduced PDF.

By combining all of the previously discussed information from XAS, XRD, and PDF, a hypothetical mechanism of sulfur tolerance from BZCYYb can be proposed, with some caveats. Firstly, it is clear from the *in situ* XRD that $BaCO_3$ is adventitiously present along with the BZCYYb synthesis. The formation of $BaCO_3$ could be a byproduct of an incomplete or non-stoichiometric reaction of BZCYYb. Typically, $BaCO_3$ is stable at high temperature, but the reducing environment appears to weaken that stability, resulting in a mixture of BaO, $Ba(OH)_2 \bullet H_2O$, and CO (Equation 15). Both of the remaining solid Ba phases are either consumed or form amorphous products upon introduction of H_2S at 750 °C. After cooling down, the remaining phases are BZCYYb, BaO, and $Ba(OH)_2 \bullet H_2O$. The $Ba(OH)_2 \bullet H_2O$ can be explained by a reaction of BaO with H_2O (Equation 16), however, based on the PDF

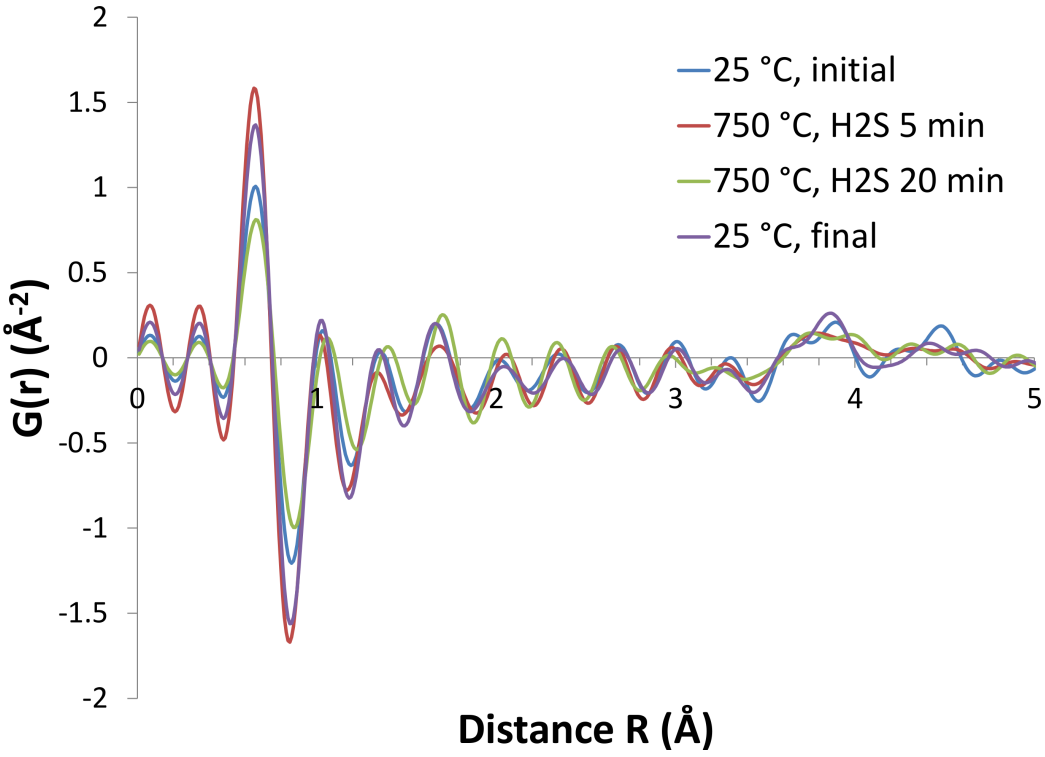

Figure 60: Short-range order comparison of the reduced PDFs of BZCYYb measured at the beginning, middle, and the end of the *in situ* experiment.

evidence of pair lengthening in the short-range structure, the cubic phase identified as BaO is more likely to be BaS, which is also cubic. This distinction between BaS and BaO may explain the faint and subtle discrepancies between the peaks observed between 700 °C and 750 °C that are not explainable by thermal expansion effects on the diffraction pattern. Also, it should taken into account that BaS and BaO will exist in equilibrium based on the ratio of H_2O and H_2S (Equation 17). Alternatively, barium hydroxide hydrate could be in equilibrium with barium bisulfide hydrate (Equation 18). Through these substitution-type reactions, it is hypothesized that H_2S is not oxidized but perhaps is preferentially bound to BaO and $Ba(OH)_2 \bullet H_2O$ over Ni, thereby keeping the Ni atoms nearby free of sulfur. If these catalytic particles are near the triple phase boundaries, their ability to divert the sulfur could be sufficient for the SOFC to continue operation despite the rest of the anode being covered in

sulfides.

$$2BaCO_3 + 2H_2 \rightleftharpoons BaO + Ba(OH)_2 \bullet H_2O + 2CO \tag{15}$$

$$BaO + 2H_2O \rightleftharpoons Ba(OH)_2 \bullet H_2O \tag{16}$$

$$BaO + H_2S \rightleftharpoons BaS + H_2O \tag{17}$$

$$Ba(OH)_2 \bullet H_2O + H_2S \rightleftharpoons Ba(SH)_2 \bullet H_2O + H_2O \tag{18}$$

However, the role of BZCYYb is still not well deciphered from these results and its reaction mechanisms with hydrogen sulfide or how H_2S may be oxidized to SO_2 are difficult to intuit. The BZCYYb itself does not appear to undergo any changes in the bulk crystal structure but Yb does show lengthening of the nearest neighbor bond similar to the PDF results. The XAS results also suggest that Yb has some interaction with the H_2S but substantially more information on the other cations and their response *in situ* to the H_2S seem necessary to narrow down the possible mechanisms of sulfur tolerance.

6.8 Conclusions

This chapter focused on using x-ray characterization techniques of varying complexity, from *ex situ* to *in situ*, to better understand the roles of specific metal cations in NiO and BZCYYb. Clearly, the challenges of characterizing a complex material like BZCYYb have been made apparent. At first, *ex situ* XAS provided some basic information about how Ni, Ba, Y, and Yb behave as a result of exposure to H_2S and served the purpose of a screening tool to better inform future experiments. Adapting the techniques employed for *in situ* x-ray characterization of the cathode materials and utilizing creative methods to generate the H_2S gas *in situ* at the cost of precision, *in situ* experiments on the anode were performed with flaws in the data to overcome and caveats to the interpretation. However, key information about the local structure of Ni and Yb provided new insights into their bonding behavior with sulfide ions as a function of temperature.

From the clarity of the phase transitions in BZCYYb, it is clear how synchrotrons drastically enhance x-ray diffraction as a technique. Based on the diffraction results, it seems that BZCYYb is dependent on water vapor converting barium oxide into an oxide-hydrate, which then is consumed in reacting with the H_2S gas. The FT EXAFS data was further augmented by powerful synchrotron-based XRD and PDF, the latter of which is a unique complement to EXAFS as a high fidelity but element-irreverent probe for local structure. While relatively simpler materials like NiO can be interpreted to some extent at short-range distances, it seems that significant investment into PDF simulation, crystal reconstruction, and refinement may be needed to obtain a full analysis of the data, particularly for complex, doped materials like BZCYYb. With the potential to determine key chemical information like isosbestic points in reaction mechanisms, extremely fast data acquisition times, and unmatched signal-to-noise quality, synchrotron-based PDF remains a characterization technique with a greatly underdeveloped and underutilized potential for important scientific discoveries.

CHAPTER VII

CONCLUSIONS

In closing, this thesis work demonstrates the feasibility and value of *in situ* and *operando* x-ray characterization experiments for deep understanding of the atomic and molecular interactions of solid oxide fuel cell electrodes. While the field of SOFC electrodes is constantly evolving with new stoichiometries, new dopants, and entirely new materials, there remain clear challenges at the cathode, with respect to chemical stability against CO_2 and H_2O, and at the anode, with respect to tolerance of H_2S and other sulfur species. To make more rapid progress in synthesizing improved SOFC electrodes, a rational design process depends on insight on the chemical processes and mechanisms that define an electrode material's performance. X-ray absorption spectroscopy, x-ray photoelectron spectroscopy, and x-ray scattering are three very powerful characterization tools that can provide unique information (whether chemical state, electron occupancy, oxidation state, surface species, local or bulk structure, or more) about the electrode materials, particularly in *in situ* or whenever possible, *operando*, experiments.

As an initial demonstration of *in situ* XAS for SOFCs, LSM-infiltrated LSCF was studied from the perspective of multiple metal cations and from K- and L-edges. This approach provided different, corroborating pieces of evidence of the stabilization of Mn in both oxidation state, crystal field, and local structure as a function of annealing. Next, a challenging *operando* XAS experiment studied degradation of a LSCF thin film cathode caused by the presence of carbon dioxide and water vapor. This experiment, to the author's knowledge, is the first *operando* XAS experiment to study degradation behavior in a SOFC. One of its most unique features is the strategy

of using the large x-ray beam size at the NSLS to obtain a sample fluorescence and reference transmission signal simultaneously. These results were later combined for deeper insight with pump-probe, *in situ* synchrotron XPS to propose transition metal cation segregation as a possible mechanism of degradation in LSCF. Lastly, *in situ* XAS was combined with *in situ* XRD and PDF to track the evolution of phases and local and crystal structure of NiO and BZCYYb as a function of temperature and exposure to H_2S. From the results of the XAS and PDF, it is suspected that sulfur may be replacing oxygen in the local structure of Yb and possibly elsewhere in the crystal structure. However, barium oxide and its interaction with water to form barium hydroxide hydrate also seems to be present and responsive to the introduction of H_2S gas. The utilization of PDF for the study of SOFC materials seems to hold significant, untapped potential. All in all, each chapter demonstrates how *in situ* and *operando* experiments, while ostensibly difficult to perform successfully, can yield key fundamental information and the pursuit of these experiments should be continued and expanded.

7.1 Future Work

With the opening of the National Synchrotron Light Source-II and its foreseeable progression into a synchrotron filled with state-of-the-art beamlines and peerless x-ray capabilities, there are new opportunities to obtain information through *in situ* and *operando* experiments. More intense x-rays with smaller spot sizes are sure to overcome previous limitations in XAS, XPS, XRD, and oher x-ray characterization techniques. For example, the spatial resolution from micron-sized and soon, nano-sized beam spots could be used to map the chemical species and electronic states near and across triple phase boundaries, where the chemical reactions most vital to SOFC operation occur. With greater intensity, newer techniques like x-ray Raman

spectroscopy are enabled to be more feasible and accessible to more scientists. X-ray Raman spectroscopy is more underdeveloped than PDF is for SOFCs, but has the ability to combine the advantages of soft x-ray spectroscopy (sensitivity to low atomic number elements) and hard x-ray spectroscopy (high information depth due to bulk sensitivity) in an unparalleled way. The development of these techniques should be paired with collaborative synthesis and computational work so that the cycle of rational design can be iterated many times, ultimately reaching optimal materials for SOFC deployment and breakthroughs in scientific understanding.

APPENDIX A

ADDITIONAL FIGURES

A.1 Figures for Chapter 4

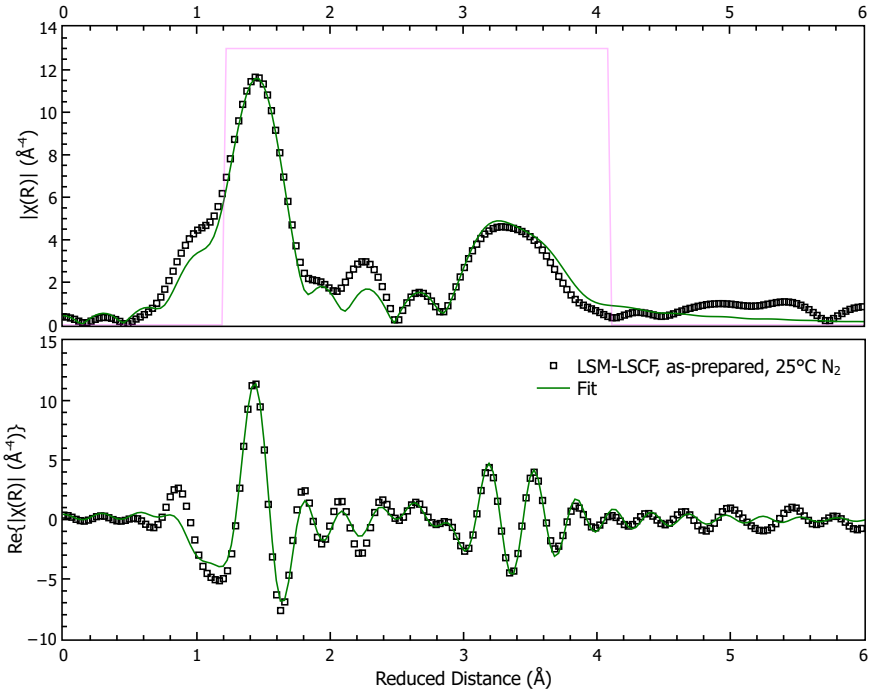

Figure 61: The Mn FT EXAFS of as-prepared LSM-LSCF after treatment in nitrogen shows consistent, intermediate steps of the changes in peak magnitudes at roughly 2.3 Å and 2.7 Å.

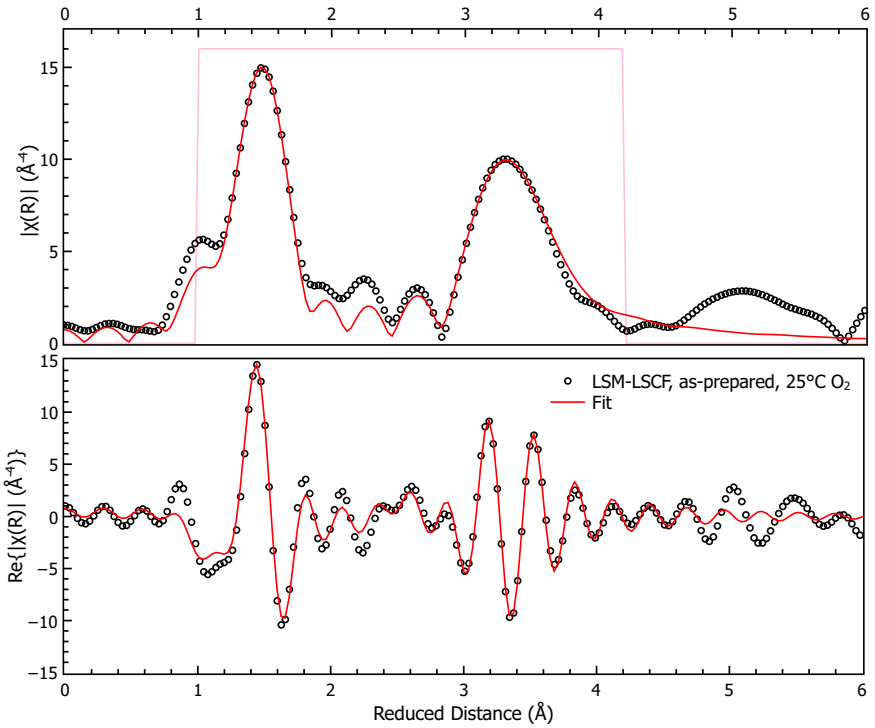

Figure 62: The Mn FT EXAFS of as-prepared LSM-LSCF after treatment in oxygen shows consistent, intermediate steps of the changes in peak magnitudes at roughly 2.3 Å and 2.7 Å.

A.2 Figures for Chapter 5

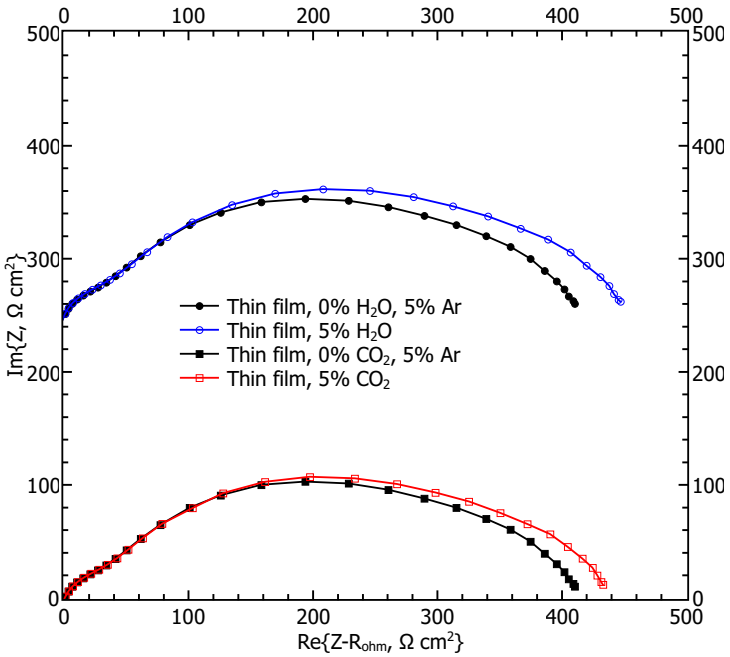

Figure 63: Impedance spectra of a thin-film LSCF cathode deposited on a single crystal YSZ substrate at 600 °C under H_2O and CO_2 and the resulting the increase in polarization resistance.

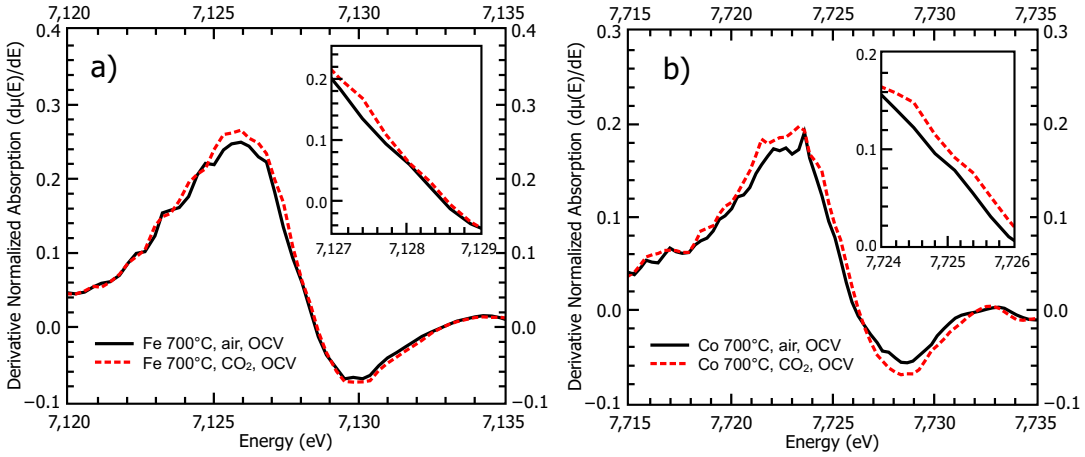

Figure 64: The derivative of the near-edge absorption of (a) Fe and (b) Co at 700 °C while exposed to H_2O and CO_2. Closer views of the edge shift are provided in the insets.

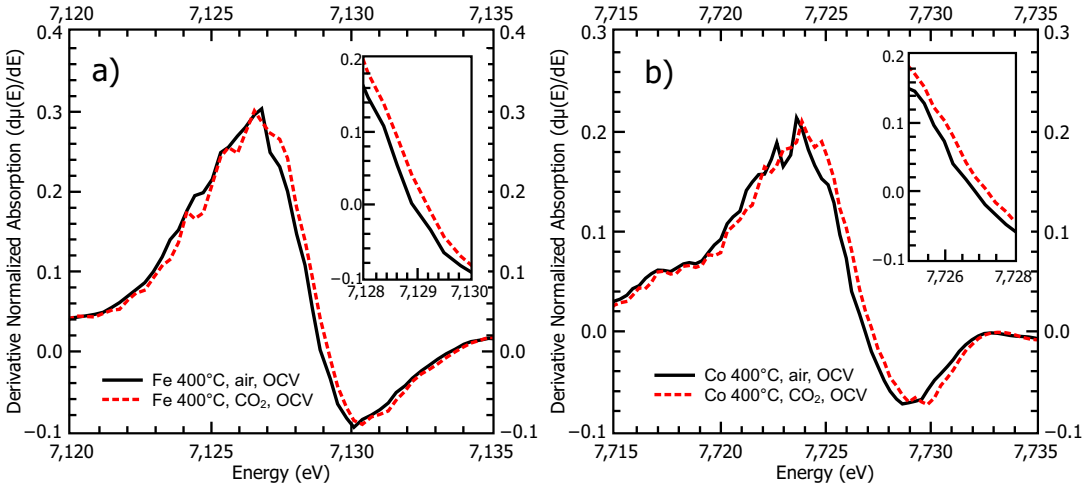

Figure 65: The derivative of the near-edge absorption of (a) Fe and (b) Co at 400 °C while exposed to H_2O and CO_2. Closer views of the edge shift are provided in the insets.

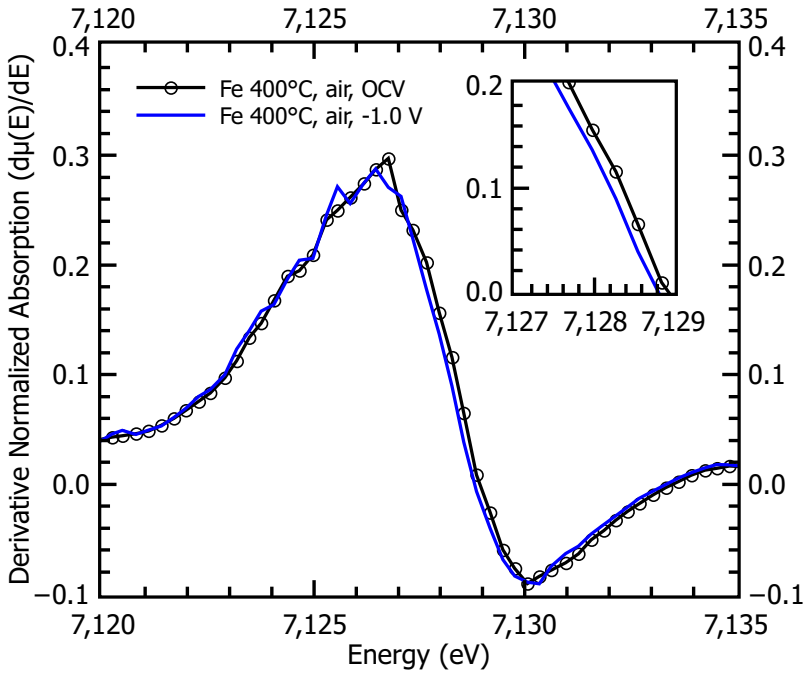

Figure 66: The derivative of the Fe XANES spectrum at 400 °C and a close-up view of the edge shift (inset).

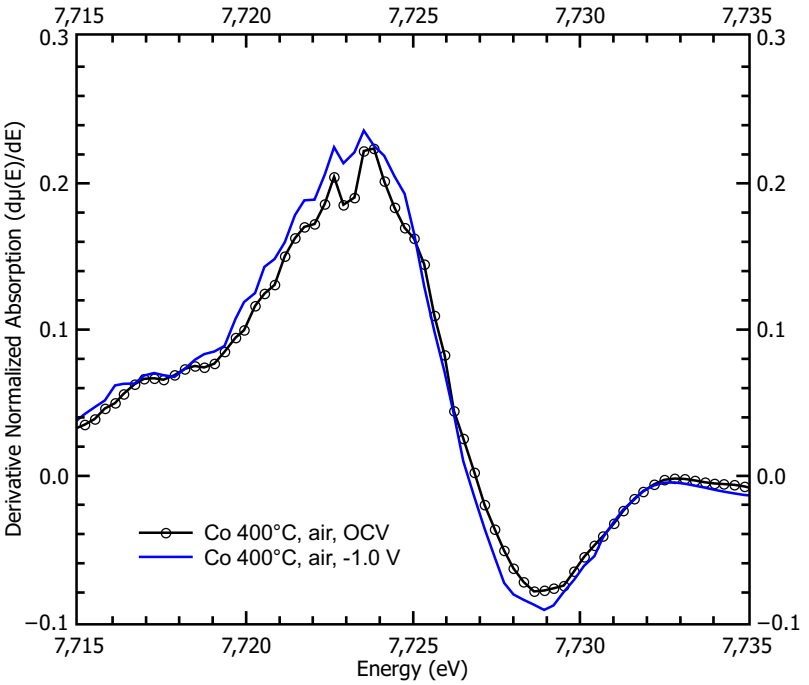

Figure 67: The derivative of the Co XANES spectrum under cathodic bias and at OCV at 400 °C for Co.

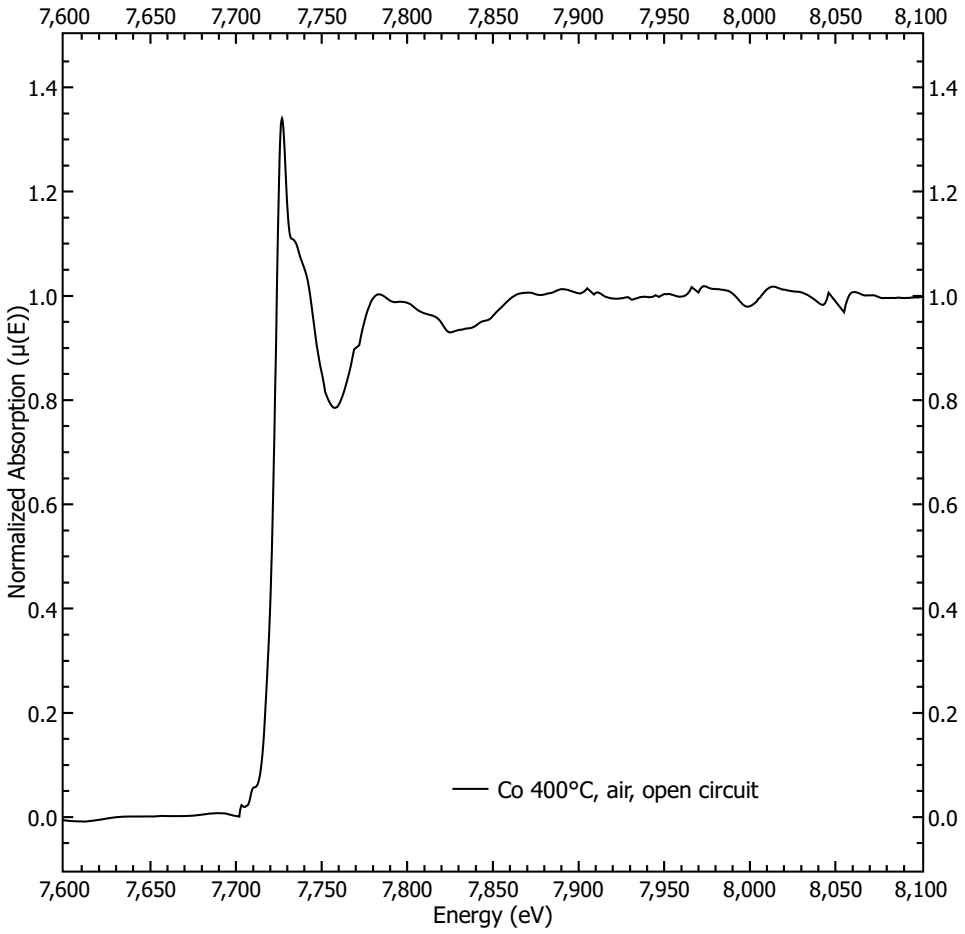

Figure 68: Example of full XAS spectrum of Co K-edge at 400 °C under air at open circuit conditions.

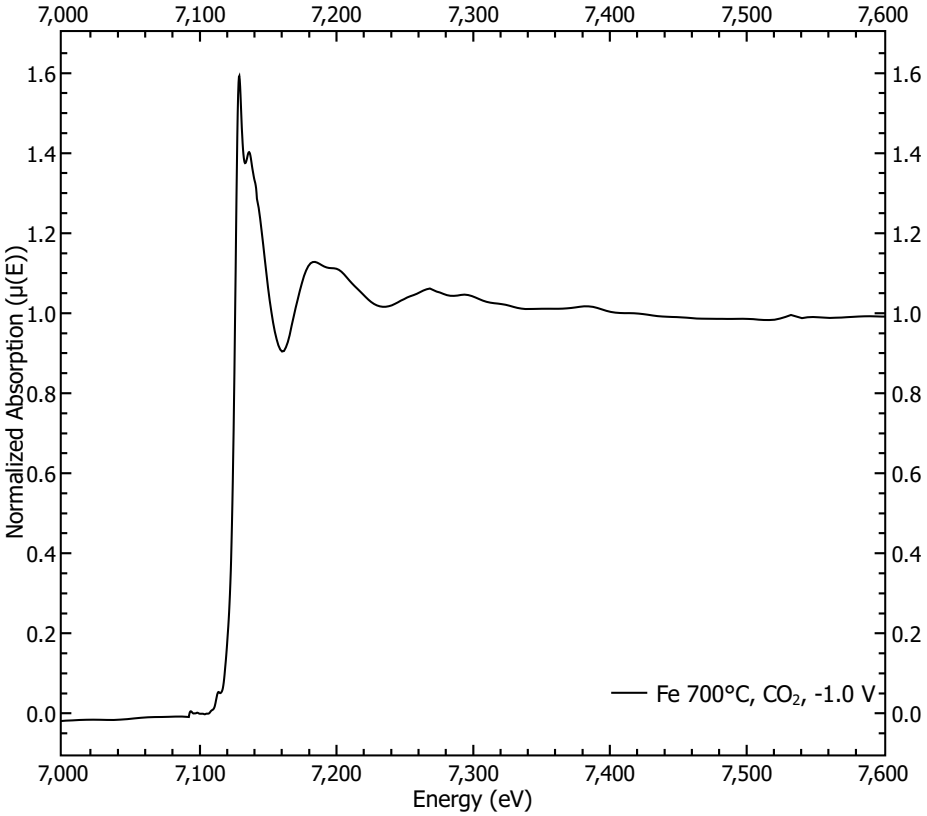

Figure 69: Example of full XAS spectrum of Fe K-edge at 700 °C under −1.0 V bias and CO_2 gas.

A.3 Figures for Chapter 6

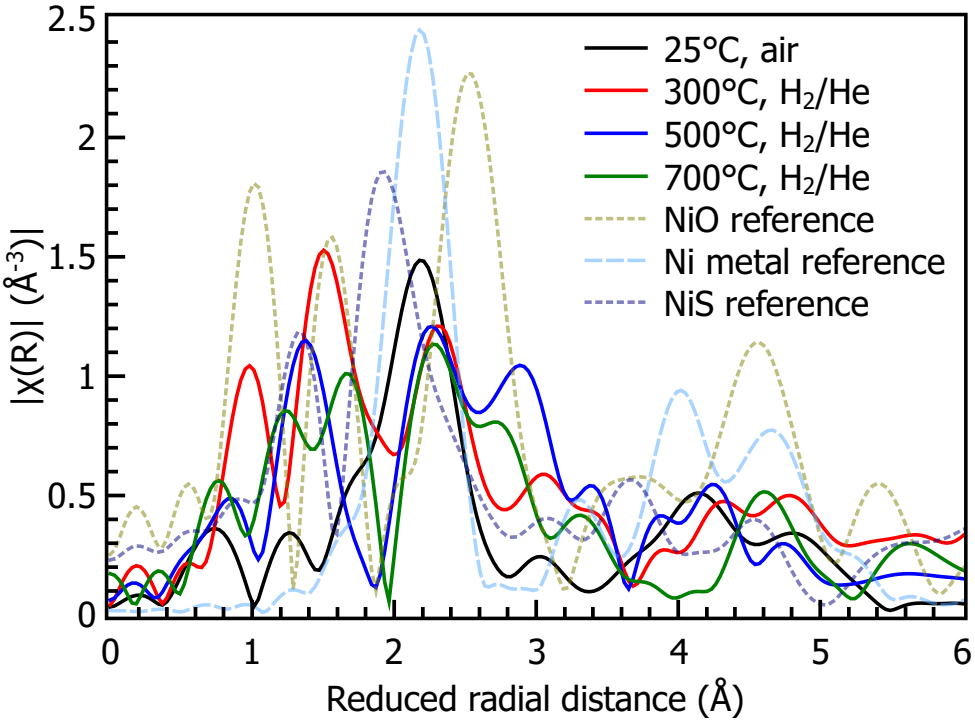

Figure 70: The Fourier transform of the Ni K-edge EXAFS at various temperatures under 5 % H_2 in He before exposure to H_2S.

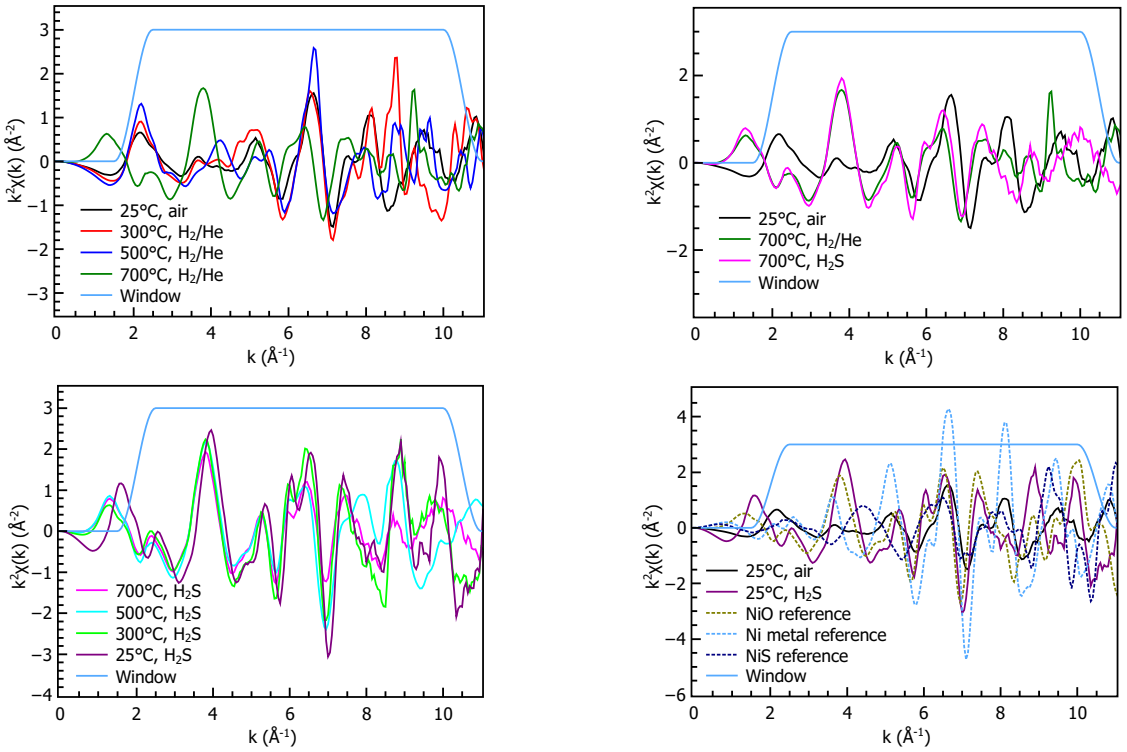

Figure 71: The Ni K-edge EXAFS in k-space at various points of the experiment for comparison. The window indicates the region for the Fourier transform.

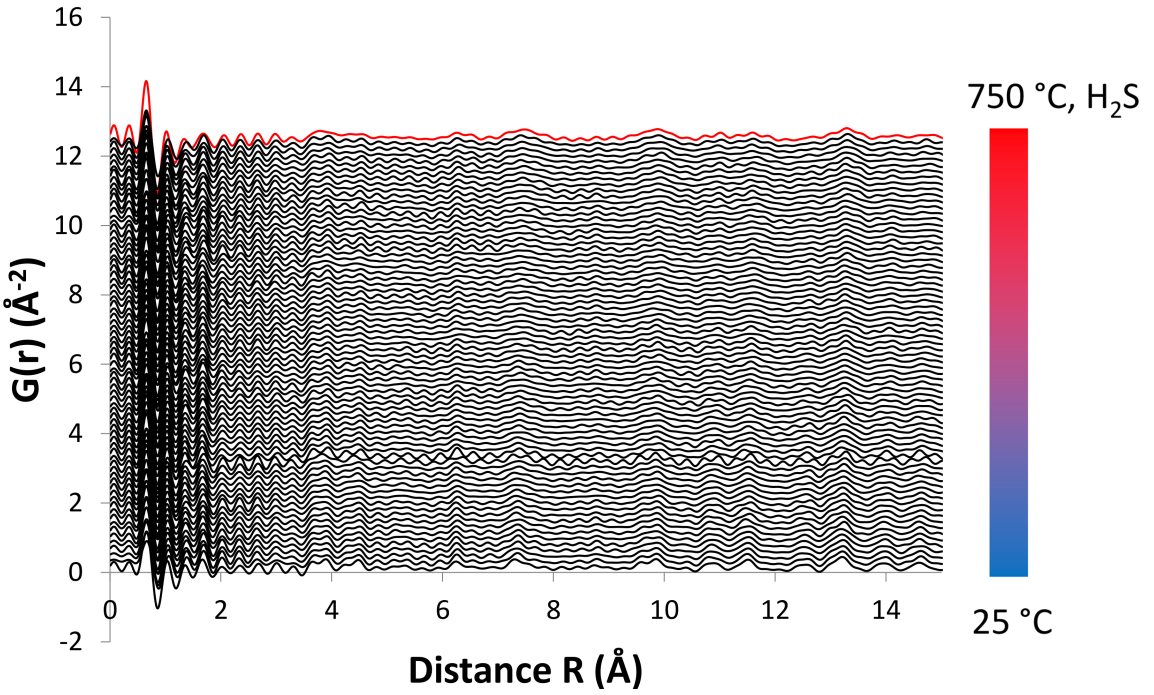

Figure 72: Overview of the reduced PDFs of BZCYYb measured *in situ* at temperatures from room temperature to 750 °C and under 5 % H_2 in He. The pattern marked in red indicates when the temperature reached at 750 °C and H_2S exposure began. Many medium-range features are dampened by the high magnitude short-range features. X-axis is adjusted for clarity.

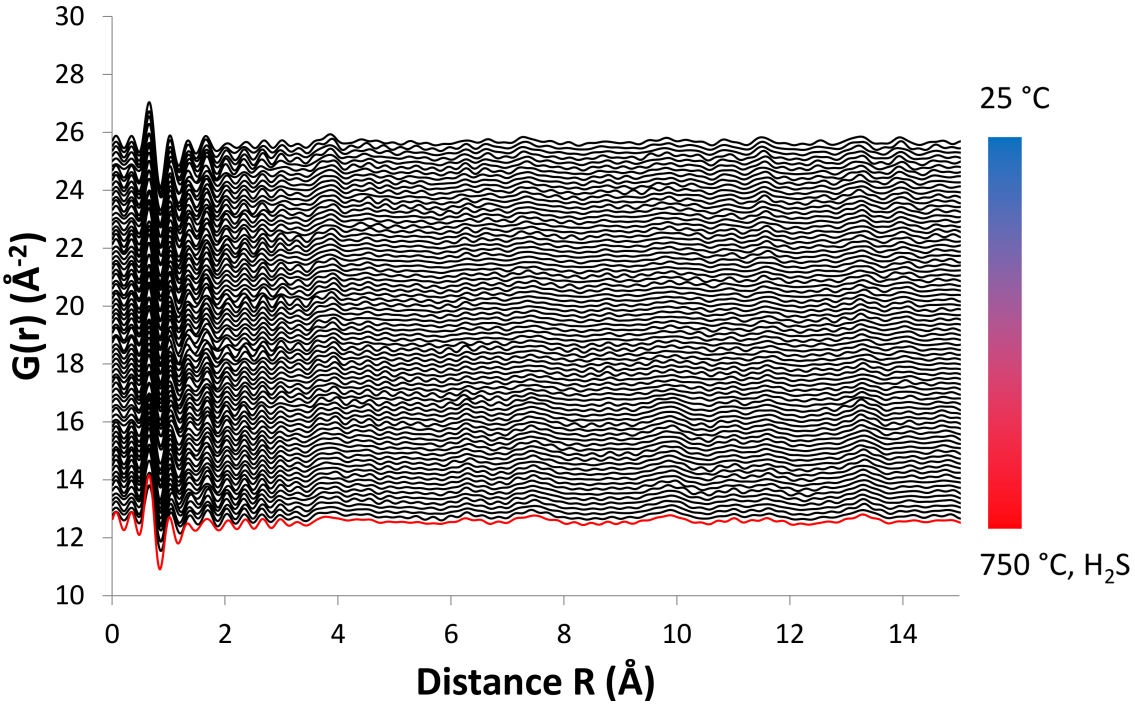

Figure 73: Overview of the reduced PDFs of BZCYYb measured *in situ* at temperatures from 750 °C to room temperature. The pattern marked in red indicates when the temperature reached at 750 °C and H_2S exposure began. Many medium-range features are dampened by the high magnitude short-range features. X-axis is adjusted for clarity.

REFERENCES

[1] Bai, Y., Liu, M., Ding, D., Blinn, K., Qin, W., Liu, J., and Liu, M., "Electrical and electrocatalytic properties of a $La_{0.8}Sr_{0.2}Co_{0.17}Mn_{0.83}O_{3-\delta}$ cathode for intermediate-temperature solid oxide fuel cells," *Journal of Power Sources*, vol. 205, no. 0, pp. 80 – 85, 2012.

[2] Benson, S. J., Waller, D., and Kilner, J. A., "Degradation of $La_{0.6}Sr_{0.4}Fe_{0.8}Co_{0.2}O_{3-\delta}$ in carbon dioxide and water atmospheres," *Journal of The Electrochemical Society*, vol. 146, no. 4, pp. 1305–1309, 1999.

[3] Blinn, K. S. and Liu, M., "$BaZr_{0.9}Yb_{0.1}O_{3-\delta}$-modified bi-electrode supported solid oxide fuel cells with enhanced coking and sulfur tolerance," *Journal of Power Sources*, vol. 243, pp. 24 – 28, 2013.

[4] Braun, A., Bayraktar, D., Erat, S., Harvey, A. S., Beckel, D., Purton, J. A., Holtappels, P., Gauckler, L. J., and Graule, T., "Pre-edges in oxygen (1s) x-ray absorption spectra: A spectral indicator for electron hole depletion and transport blocking in iron perovskites," *Applied Physics Letters*, vol. 94, no. 20, p. 202102, 2009.

[5] Brightman, E., Maher, R., Offer, G. J., Duboviks, V., Heck, C., Cohen, L. F., and Brandon, N. P., "Designing a miniaturised heated stage for in situ optical measurements of solid oxide fuel cell electrode surfaces, and probing the oxidation of solid oxide fuel cell anodes using in situ Raman spectroscopy," *Review of Scientific Instruments*, vol. 83, no. 5, p. 053707, 2012.

[6] Carley, A., Rassias, S., and Roberts, M., "The specificity of surface oxygen in the activation of adsorbed water at metal surfaces," *Surface Science*, vol. 135, no. 1-3, pp. 35 – 51, 1983.

[7] Chang, K.-C., Ingram, B., Kavaipatti, B., Yildiz, B., Hennessy, D., Salvador, P., Leyarovska, N., and You, H., "In situ synchrotron x-ray studies of dense thin-film strontium-doped lanthanum manganite solid oxide fuel cell cathodes," in *Materials Research Society 2008 Fall Meeting Proceedings*, vol. 1126, 2009.

[8] Chang, K.-C., Ingram, B., Salvador, P., Yildiz, B., and You, H., "In situ x-ray studies of (La,Sr)MnO_3, (La,Sr)CoO_3, and $La_{0.6}Sr_{0.4}Co_{0.2}Fe_{0.8}O_{3-\delta}$ thin film SOFC cathodes grown by pulse laser deposition," *MRS Online Proceedings Library*, vol. 1495, 1 2013.

[9] Chen, P., Zhou, X., Shen, H., Andoy, N. M., Choudhary, E., Han, K.-S., Liu, G., and Meng, W., "Single-molecule fluorescence imaging of nanocatalytic processes," *Chem. Soc. Rev.*, vol. 39, pp. 4560–4570, 2010.

[10] Chen, Y., Jung, W., Cai, Z., Kim, J. J., Tuller, H. L., and Yildiz, B., "Impact of Sr segregation on the electronic structure and oxygen reduction activity of $SrTi_{1-x}Fe_xO_3$ surfaces," *Energy Environ. Sci.*, vol. 5, pp. 7979–7988, 2012.

[11] Choi, J.-J., Qin, W., Liu, M., and Liu, M., "Preparation and characterization of $(La_{0.8}Sr_{0.2})_{0.95}MnO_{3-\delta}$ (LSM) thin films and LSM/LSCF interface for solid oxide fuel cells," *Journal of the American Ceramic Society*, vol. 94, no. 10, pp. 3340–3345, 2011.

[12] Choi, Y., Lin, M., and Liu, M., "Rational design of novel cathode materials in solid oxide fuel cells using first-principles simulations," *Journal of Power Sources*, vol. 195, no. 5, pp. 1441 – 1445, 2010.

[13] Coduri, M., Scavini, M., Brunelli, M., and Masala, P., "In situ pair distribution function study on lanthanum doped ceria," *Phys. Chem. Chem. Phys.*, vol. 15, pp. 8495–8505, 2013.

[14] Crumlin, E. J., Mutoro, E., Liu, Z., Grass, M. E., Biegalski, M. D., Lee, Y.-L., Morgan, D., Christen, H. M., Bluhm, H., and Shao-Horn, Y., "Surface strontium enrichment on highly active perovskites for oxygen electrocatalysis in solid oxide fuel cells," *Energy Environ. Sci.*, vol. 5, pp. 6081–6088, 2012.

[15] Dahéron, L., Dedryvère, R., Martinez, H., M?n?trier, M., Denage, C., Delmas, C., and Gonbeau, D., "Electron transfer mechanisms upon lithium deintercalation from $LiCoO_2$ to CoO_2 investigated by XPS," *Chemistry of Materials*, vol. 20, no. 2, pp. 583–590, 2008.

[16] Deabate, S., Gebel, G., Huguet, P., Morin, A., and Pourcelly, G., "3 in situ and operando determination of the water content distribution in proton conducting membranes for fuel cells: a critical review," *Energy Environ. Sci.*, vol. 5, pp. 8824–8847, 2012.

[17] Ding, D., Li, X., Lai, S. Y., Gerdes, K., and Liu, M., "Enhancing SOFC cathode performance by surface modification through infiltration," *Energy Environ. Sci.*, vol. 7, no. 2, pp. 552 – 575, 2014.

[18] Dupin, J.-C., Gonbeau, D., Vinatier, P., and Levasseur, A., "Systematic XPS studies of metal oxides, hydroxides and peroxides," *Phys. Chem. Chem. Phys.*, vol. 2, pp. 1319–1324, 2000.

[19] Fabbri, E., Pergolesi, D., and Traversa, E., "Ionic conductivity in oxide heterostructures: the role of interfaces," *Science and Technology of Advanced Materials*, vol. 11, no. 5, p. 054503, 2010.

[20] Farrow, C. L., Juhas, P., Liu, J. W., Bryndin, D., Boin, E. S., Bloch, J., Proffen, T., and Billinge, S. J. L., "PDFfit2 and PDFgui: computer

programs for studying nanostructure in crystals," *Journal of Physics: Condensed Matter*, vol. 19, no. 33, p. 335219, 2007.

[21] Hammersley, A. P., "FIT2D: An introduction and overview," ESRF Internal Report ESRF97HA02T, European Synchrotron Radiation Facility, 1997.

[22] Hammersley, A. P., Svensson, S. O., Hanfland, M., Fitch, A. N., and Hausermann, D., "Two-dimensional detector software: From real detector to idealised image or two-theta scan," *High Pressure Research*, vol. 14, pp. 235–248, Jan. 1996.

[23] Heising, V. P. S. J. L. B. J. and Kanatzidis, M. G., "Application of atomic pair distribution function analysis to materials with intrinsic disorder. three-dimensional structure of exfoliated-restacked WS_2: Not just a random turbostratic assembly of layers," *Journal of the American Chemical Society*, vol. 122, no. 47, pp. 11571–11576, 2000.

[24] Imamura, M., Matsubayashi, N., and Shimada, H., "Catalytically active oxygen species in $La_{1-x}Sr_xCoO_{3-\delta}$ studied by XPS and XAFS spectroscopy," *The Journal of Physical Chemistry B*, vol. 104, no. 31, pp. 7348–7353, 2000.

[25] Jiang, S. P., "Nanoscale and nano-structured electrodes of solid oxide fuel cells by infiltration: Advances and challenges," *International Journal of Hydrogen Energy*, vol. 37, no. 1, pp. 449 – 470, 2012. ¡ce:title¿11th China Hydrogen Energy Conference¡/ce:title¿.

[26] Jiang, S. P. and Chen, X., "Chromium deposition and poisoning of cathodes of solid oxide fuel cells - a review," *International Journal of Hydrogen Energy*, vol. 39, no. 1, pp. 505 – 531, 2014.

[27] Juhás, P., Davis, T., Farrow, C. L., and Billinge, S. J. L., "*PDFgetX3*: a rapid and highly automatable program for processing powder diffraction data into total scattering pair distribution functions," *Journal of Applied Crystallography*, vol. 46, pp. 560–566, Apr 2013.

[28] Jung, W. and Tuller, H. L., "Investigation of surface Sr segregation in model thin film solid oxide fuel cell perovskite electrodes," *Energy Environ. Sci.*, vol. 5, pp. 5370–5378, 2012.

[29] Kan, C. C. and Wachsman, E. D., "Identifying drivers of catalytic activity through systematic surface modification of cathode materials," *Journal of The Electrochemical Society*, vol. 156, no. 6, pp. B695–B702, 2009.

[30] Kelly, S. D., Hesterberg, D., and Ravel, B., "Analysis of soils and minerals using x-ray absorption spectroscopy," in *Methods of Soil Analysis, Part 5: Mineralogical Methods* (Drees, L. R. and Ulery, A. L., eds.), Methods of Soil Analysis, ch. 14, pp. 387 – 463, Soil Science Society of America, 2008.

[31] Kim, J. Y., Sprenkle, V. L., Canfield, N. L., Meinhardt, K. D., and Chick, L. A., "Effects of chrome contamination on the performance of $La_{0.6}Sr_{0.4}Co_{0.2}Fe_{0.8}O_{3-\delta}$ cathode used in solid oxide fuel cells," *Journal of The Electrochemical Society*, vol. 153, no. 5, pp. A880–A886, 2006.

[32] Kirtley, J. D., Halat, D. M., McIntyre, M. D., Eigenbrodt, B. C., and Walker, R. A., "High-temperature "spectrochronopotentiometry": Correlating electrochemical performance with in situ Raman spectroscopy in solid oxide fuel cells," *Analytical Chemistry*, vol. 84, no. 22, pp. 9745–9753, 2012.

[33] Lai, S. Y., Ding, D., Liu, M., Liu, M., and Alamgir, F. M., "Operando and in-situ x-ray spectroscopies of degradation in $La_{0.6}Sr_{0.4}Co_{0.2}Fe_{0.8}O_{3-\delta}$ thin film cathodes in fuel cells," *ChemSusChem*, vol. 7, pp. 3078–3087, November 2014.

[34] Lane, J., Benson, S., Waller, D., and Kilner, J., "Oxygen transport in $La_{0.6}Sr_{0.4}Co_{0.2}Fe_{0.8}O_{3-\delta}$," *Solid State Ionics*, vol. 121, no. 1-4, pp. 201 – 208, 1999.

[35] Lee, J.-W., Liu, Z., Yang, L., Abernathy, H., Choi, S.-H., Kim, H.-E., and Liu, M., "Preparation of dense and uniform $La_{0.6}Sr_{0.4}Co_{0.2}Fe_{0.8}O_{3-\delta}$ (LSCF) films for fundamental studies of SOFC cathodes," *Journal of Power Sources*, vol. 190, no. 2, pp. 307 – 310, 2009.

[36] Lewis, E. A., Kendrick, I., Jia, Q., Grice, C., Segre, C. U., and Smotkin, E. S., "Operando x-ray absorption and infrared fuel cell spectroscopy," *Electrochimica Acta*, vol. 56, no. 24, pp. 8827 – 8832, 2011.

[37] Li, S., Jin, W., Huang, P., Xu, N., Shi, J., and Lin, Y., "Tubular lanthanum cobaltite perovskite type membrane for oxygen permeation," *Journal of Membrane Science*, vol. 166, no. 1, pp. 51 – 61, 2000.

[38] Li, X., Blinn, K., Fang, Y., Liu, M., Mahmoud, M. A., Cheng, S., Bottomley, L. A., El-Sayed, M., and Liu, M., "Application of surface enhanced raman spectroscopy to the study of SOFC electrode surfaces," *Phys. Chem. Chem. Phys.*, vol. 14, pp. 5919–5923, 2012.

[39] Liu, D.-J. and Almer, J., "Phase and strain distributions associated with reactive contaminants inside of a solid oxide fuel cell," *Applied Physics Letters*, vol. 94, no. 22, p. 224106, 2009.

[40] Liu, M., Liu, Z., Liu, M. F., Nie, L. F., Mebane, D. S., Wilson, D. S., and Surdoval, W., "Solid oxide fuel cells having porous cathodes infiltrated with oxygen-reducing catalysts." Patent, 2010.

[41] Liu, M., Lynch, M. E., Blinn, K., Alamgir, F. M., and Choi, Y., "Rational SOFC material design: new advances and tools," *Materials Today*, vol. 14, pp. 534–546, 2011.

[42] Liu, M., Ding, D., Blinn, K., Li, X., Nie, L., and Liu, M., "Enhanced performance of LSCF cathode through surface modification," *Int. J. Hydrogen Energy*, vol. 37, no. 10, pp. 8613–8620, 2012. International Conference: Photosynthesis Research for Sustainability.

[43] Lynch, M. E., Ding, D., Harris, W. M., Lombardo, J. J., Nelson, G. J., Chiu, W. K., and Liu, M., "Flexible multiphysics simulation of porous electrodes: Conformal to 3D reconstructed microstructures," *Nano Energy*, vol. 2, no. 1, pp. 105 – 115, 2013.

[44] Lynch, M. E. and Liu, M., "Investigation of sheet resistance in thin-film mixed-conducting solid oxide fuel cell cathode test cells," *Journal of Power Sources*, vol. 195, no. 16, pp. 5155–5166, 2010.

[45] Lynch, M. E., Yang, L., Qin, W., Choi, J.-J., Liu, M., Blinn, K., and Liu, M., "Enhancement of $La_{0.6}Sr_{0.4}Co_{0.2}Fe_{0.8}O_{3-\delta}$ durability and surface electrocatalytic activity by $La_{0.85}Sr_{0.15}MnO_{3\pm\delta}$ investigated using a new test electrode platform," *Energy Environ. Sci.*, vol. 4, pp. 2249–2258, 2011.

[46] Mamontov, E. and Egami, T., "Structural defects in a nano-scale powder of CeO_2 studied by pulsed neutron diffraction," *Journal of Physics and Chemistry of Solids*, vol. 61, no. 8, pp. 1345 – 1356, 2000.

[47] Mantzavinos, D., Hartley, A., Metcalfe, I. S., and Sahibzada, M., "Oxygen stoichiometries in $La_{1-x}Sr_xCo_{1-y}Fe_yO_{3-\delta}$ perovskites at reduced oxygen partial pressures," *Solid State Ionics*, vol. 134, no. 1-2, pp. 103 – 109, 2000.

[48] Masadeh, A. S., Božin, E. S., Farrow, C. L., Paglia, G., Juhas, P., Billinge, S. J. L., Karkamkar, A., and Kanatzidis, M. G., "Quantitative size-dependent structure and strain determination of CdSe nanoparticles using atomic pair distribution function analysis," *Phys. Rev. B*, vol. 76, p. 115413, Sep 2007.

[49] McIntyre, N. S. and Cook, M. G., "X-ray photoelectron studies on some oxides and hydroxides of cobalt, nickel, and copper," *Analytical Chemistry*, vol. 47, no. 13, pp. 2208–2213, 1975.

[50] Melo, D. M., Borges, F. M., Ambrosio, R. C., Pimentel, P. M., da Silva Jnior, C. N., and Melo, M. A., "XAFS characterization of $La_{1-x}Sr_xMnO_{3-\delta}$ catalysts prepared by Pechini's method," *Chemical Physics*, vol. 322, no. 3, pp. 477 – 484, 2006.

[51] Mukundan, R., Brosha, E. L., and Garzon, F. H., "Sulfur tolerant anodes for SOFCs," *Electrochemical and Solid-State Letters*, vol. 7, no. 1, pp. A5–A7, 2004.

[52] Murray, E. P., Sever, M., and Barnett, S., "Electrochemical performance of (La,Sr)(Co,Fe)$o_{3-\delta}$(Ce,Gd)O_3 composite cathodes," *Solid State Ionics*, vol. 148, no. 1-2, pp. 27 – 34, 2002.

[53] Nachimuthu, P., Kim, Y. J., Kuchibhatla, S. V. N. T., Yu, Z. Q., Jiang, W., Engelhard, M. H., Shutthanandan, V., Szanyi, J., and Thevuthasan, S., "Growth and characterization of barium oxide nanoclusters on YSZ(111)," *The Journal of Physical Chemistry C*, vol. 113, no. 32, pp. 14324–14328, 2009.

[54] NETL, "Fuel cells." `http://www.netl.doe.gov/research/on-site-research/research-portfolio/coal-research/seca-index`. Accessed on 22 May 2015.

[55] Nie, L. F., Liu, Z., Liu, M., Yang, L., Zhang, Y., and Liu, M., "Enhanced performance of $La_{0.6}Sr_{0.4}Co_{0.2}Fe_{0.8}O_{3-\delta}$ (LSCF) cathodes with graded microstructure fabricated by tape casting," *Journal of Electrochemical Science and Technology*, vol. 1, no. 1, pp. 50–56, 2010.

[56] Offer, G. J., Mermelstein, J., Brightman, E., and Brandon, N. P., "Thermodynamics and kinetics of the interaction of carbon and sulfur with solid oxide fuel cell anodes," *Journal of the American Ceramic Society*, vol. 92, no. 4, pp. 763–780, 2009.

[57] Orikasa, Y., Nakao, T., Oishi, M., Ina, T., Mineshige, A., Amezawa, K., Arai, H., Ogumi, Z., and Uchimoto, Y., "Local structural analysis for oxide ion transport in $La_{0.6}Sr_{0.4}FeO_{3-\delta}$ cathodes," *J. Mater. Chem.*, vol. 21, pp. 14013–14019, 2011.

[58] Petkov, V., Jeong, I.-K., Chung, J. S., Thorpe, M. F., Kycia, S., and Billinge, S. J. L., "High real-space resolution measurement of the local structure of $Ga_{1-x}In_xAs$ using x-ray diffraction," *Phys. Rev. Lett.*, vol. 83, pp. 4089–4092, Nov 1999.

[59] Principi, E., Di Cicco, A., Witkowska, A., and Marassi, R., "Performance of a fuel cell optimized for *in situ* x-ray absorption experiments," *Journal of Synchrotron Radiation*, vol. 14, pp. 276 – 281, May 2007.

[60] Ravel, B. and Newville, M., "*ATHENA*, *ARTEMIS*, *HEPHAESTUS*: data analysis for X-ray absorption spectroscopy using *IFEFFIT*," *Journal of Synchrotron Radiation*, vol. 12, pp. 537–541, Jul 2005.

[61] Redmond, E. L., Setzler, B. P., Juhas, P., Billinge, S. J. L., and Fuller, T. F., "In-situ monitoring of particle growth at PEMFC cathode under accelerated cycling conditions," *Electrochemical and Solid-State Letters*, vol. 15, no. 5, pp. B72–B74, 2012.

[62] Rodríguez-Carvajal, J., Hennion, M., Moussa, F., Moudden, A. H., Pinsard, L., and Revcolevschi, A., "Neutron-diffraction study of the jahn-teller transition in stoichiometric $lamno_3$," *Phys. Rev. B*, vol. 57, pp. R3189–R3192, Feb 1998.

[63] Russell, A. E., Maniguet, S., Mathew, R. J., Yao, J., Roberts, M. A., and Thompsett, D., "In situ x-ray absorption spectroscopy and x-ray diffraction of fuel cell electrocatalysts," *Journal of Power Sources*, vol. 96, no. 1, pp. 226 – 232, 2001. Proceedings of the 22nd International Power Sources Symposium.

[64] Selman, J. R., "Poison-tolerant fuel cells," *Science*, vol. 326, no. 5949, pp. 52–53, 2009.

[65] Sengodan, S., Liu, M., Lim, T.-H., Shin, J., Liu, M., and Kim, G., "Enhancing sulfur tolerance of a ni-ysz anode through bazr0.1ce0.7y0.1yb0.1o3 infiltration," *Journal of The Electrochemical Society*, vol. 161, no. 5, pp. F668–F673, 2014.

[66] Seremak-Peczkis, P., Schneider, K., Zajaczkowski, W., Kapusta, C., Zajac, D., Pasierb, P., Bucko, M., Drozdz-Ciesla, E., and Rekas, M., "XAFS study of $BaCe_{1-x}Ti_xO_3$ and $Ba_{1-y}Ce_{1-x}Y_xO_3$ protonic solid electrolytes," *Radiation Physics and Chemistry*, vol. 78, no. 10, Supplement 1, pp. S86 – S88, 2009. Proceedings of the Nineth International School and Symposium on Synchrotron Radiation in Natural Science (ISSRNS-9) June 15-20, Ameliwka, Poland.

[67] Shao, Z. and Haile, S. M., "A high-performance cathode for the next generation of solid-oxide fuel cells," *Nature*, vol. 431, pp. 170–173, 2004.

[68] Shchukarev, A. and Korolkov, D., "XPS study of group IA carbonates," *Central European Journal of Chemistry*, vol. 2, no. 2, pp. 347–362, 2004.

[69] Shen, X.-F., Ding, Y.-S., Hanson, J. C., Aindow, M., and Suib, S. L., "In situ synthesis of mixed-valent manganese oxide nanocrystals: An in situ synchrotron x-ray diffraction study," *Journal of the American Chemical Society*, vol. 128, no. 14, pp. 4570–4571, 2006. PMID: 16594683.

[70] Simner, S. P., Anderson, M. D., Engelhard, M. H., and Stevenson, J. W., "Degradation mechanisms of La–Sr–Co–Fe–O_3 SOFC cathodes," *Electrochemical and Solid-State Letters*, vol. 9, no. 10, pp. A478–A481, 2006.

[71] Stavitski, E. and de Groot, F. M., "The *CTM4XAS* program for EELS and XAS spectral shape analysis of transition metal L edges," *Micron*, vol. 41, pp. 687–694, 2010.

[72] Stoch, J. and Gablankowska-Kukucz, J., "The effect of carbonate contaminations on the XPS O 1s band structure in metal oxides," *Surface and Interface Analysis*, vol. 17, no. 3, pp. 165–167, 1991.

[73] Takeshi, E. and Billinge, S. J., "Chapter 2 - crystallographic analysis of complex materials," in *Underneath the Bragg PeaksStructural Analysis of Complex Materials* (Egami, T. and Billinge, S. J., eds.), vol. 16 of *Pergamon Materials Series*, pp. 27 – 54, Pergamon, 2012.

[74] Thursfield, A. and Metcalfe, I. S., "Air separation using a catalytically modified mixed conducting ceramic hollow fibre membrane module," *Journal of Membrane Science*, vol. 288, no. 12, pp. 175 – 187, 2007.

[75] van der Heide, P. A. W., "Systematic x-ray photoelectron spectroscopic study of $La_{1-x}Sr_x$-based perovskite-type oxides," *Surface and Interface Analysis*, vol. 33, no. 5, pp. 414–425, 2002.

[76] Vasquez, R., "X-ray photoelectron spectroscopy study of Sr and Ba compounds," *Journal of Electron Spectroscopy and Related Phenomena*, vol. 56, no. 3, pp. 217 – 240, 1991.

[77] Vora, S. D., "Recent developments in the SECA program," *ECS Transactions*, vol. 35, no. 1, pp. 3–9, 2011.

[78] Wang, W., Su, C., Wu, Y., Ran, R., and Shao, Z., "Progress in solid oxide fuel cells with nickel-based anodes operating on methane and related fuels," *Chemical Reviews*, vol. 113, no. 10, pp. 8104–8151, 2013.

[79] Weber, A., Mench, M., Meyers, J., Ross, P., Gostick, J., and Liu, Q., "Redox flow batteries: a review," *Journal of Applied Electrochemistry*, vol. 41, no. 10, pp. 1137–1164, 2011.

[80] Winter, M., "Oxygen: radii of atoms and ions." `http://www.webelements.com/oxygen/atom_sizes.html`, 2015. Accessed 9 Oct 2015.

[81] Xia, C. and Liu, M., "Novel cathodes for low-temperature solid oxide fuel cells," *Advanced Materials*, vol. 14, no. 7, pp. 521–523, 2002.

[82] Yang, L., Choi, Y., Qin, W., Chen, H., Blinn, K., Liu, M., Liu, P., Bai, J., Tyson, T. A., and Liu, M., "Promotion of water-mediated carbon removal by nanostructured barium oxide/nickel interfaces in solid oxide fuel cells," *Nature Communications*, vol. 2, no. 357, pp. 1–9, 2011.

[83] Yang, L., Wang, S., Blinn, K., Liu, M., Liu, Z., Cheng, Z., and Liu, M., "Enhanced sulfur and coking tolerance of a mixed ion conductor for SOFCs: $BaZr_{0.1}Ce_{0.7}Y_{0.2-x}Yb_xO_{3-\delta}$," *Science*, vol. 326, pp. 126 – 129, October 2009.

[84] Yang, Z., Zhang, J., Kintner-Meyer, M. C. W., Lu, X., Choi, D., Lemmon, J. P., and Liu, J., "Electrochemical energy storage for green grid," *Chemical Reviews*, vol. 111, no. 5, pp. 3577–3613, 2011.

[85] Yashima, M., "Invited review: Some recent developments in the atomic-scale characterization of structural and transport properties of ceria-based catalysts and ionic conductors," *Catalysis Today*, vol. 253, pp. 3 – 19, 2015.

[86] Yildiz, B., Chang, K.-C., Myers, D., Carter, J. D., and You, H., "In situ x-ray, electrochemical, and modeling investigation of the oxygen electrode activation," in *7th European Solid Oxide Fuel Cell Forum*, Proceedings of the Lucerne Fuel Cell Forum, 2006.

[87] Zha, S., Cheng, Z., and Liu, M., "Sulfur poisoning and regeneration of Ni-based anodes in solid oxide fuel cells," *Journal of The Electrochemical Society*, vol. 154, no. 2, pp. B201–B206, 2007.

[88] Zhang, L., Jiang, S. P., He, H. Q., Chen, X., Ma, J., and Song, X. C., "A comparative study of H_2S poisoning on electrode behavior of Ni/YSZ and Ni/GDC anodes of solid oxide fuel cells," *International Journal of Hydrogen Energy*, vol. 35, no. 22, pp. 12359 – 12368, 2010. Bio-Ethanol and Other Renewable Sources and Reforming Process for Sustainable Hydrogen Production.

VITA

Samson Y. Lai was born in southeast Michigan. The second child of immigrant mainland Chinese parents, he was born and raised in a largely Chinese household in an somewhat American suburb. After graduating from the University of Michigan in Ann Arbor with a Bachelor's degree in Materials Science and Engineering, he came to the Georgia Institute of Technology to pursue his Ph. D. degree in Materials Science and Engineering and to continue broadening his cultural experiences.